New observations of Arctic sea ice from satellite radar altimetry

Rachel L. Tilling

A thesis submitted to University College London for the degree of Doctor of Philosophy

November 2016

I, Rachel Tilling, confirm that the work presented in this thesis is my own. Where information has been derived from other sources, I confirm that this has been indicated in the work.

Abstract

Satellite observations of Arctic sea ice have observed a decline in extent for all months since 1979. The decline is coincident with abrupt global and Arctic warming over the last 30 years. Over this 30-year period the mean Arctic temperature has increased at almost twice the global average rate – a phenomena known as Arctic amplification. It is crucial to observe and understand changes in Arctic sea ice, as it is a major element of the Earth's climate system. The sea ice cover acts to regulate solar absorption, ocean-atmosphere heat exchange, and freshwater and brine input into the Arctic Ocean and subpolar North Atlantic. The subsequent changes in the regional heat and freshwater budgets impact on patterns of atmospheric and oceanic circulation across the Arctic and at lower latitudes. These in turn impact on global weather patterns. To fully understand the global impacts of changes in the Arctic sea ice cover, long-term and accurate observations of the ice pack as a whole are required. However, it has previously been difficult to quantify trends in sea ice volume because detailed thickness observations have been lacking. The European Space Agency's (ESA's) CryoSat-2 satellite was launched in April 2010 and now provides unparalleled coverage of the Arctic Ocean up to 88°N. CryoSat-2 data have been used in this study to provide the first estimates of sea ice thickness and volume across the entire Northern Hemisphere. Using five years of CryoSat-2 measurements a 14% reduction in sea ice volume was observed between autumn 2010 and 2012, in keeping with the long-term decline in extent. However, 33% and 25% more ice were observed in autumn 2013 and 2014, respectively, relative to the 2010–2012 seasonal mean, which offset earlier losses. The increase was caused by the retention of thick sea ice northwest of Greenland during 2013 which, in turn, was associated with a 5% drop in the number of days on which melting occurred. This coincides with conditions more typical of the late 1990s. In contrast, springtime Arctic sea ice volume has remained stable. The sharp increase in sea ice volume after just one cool summer demonstrates the ability of Arctic sea ice to respond rapidly to a changing environment. Since April 2015, ESA have provided fast delivery CryoSat-2 data, which are based on preliminary orbits. The fast delivery data have been used to produce near real time (NRT) estimates of Arctic sea ice thickness and volume. This study finds that the NRT dataset provides a measurement within 14, 7 and 6 km of each location in the Arctic every 2, 14 and 28 days respectively. NRT sea ice thickness and volume data provide a new resource and opportunity for the developers of short-term sea ice forecast models. These models can provide information such as sea ice location, drift and thickness to operational users. Currently the utility of the NRT data for model and operational use is limited by a lack of availability in summer months. The expansion of sea ice thickness observations in to the melt season will form the basis of future work.

Acknowledgements

First and foremost I wish to acknowledge my supervisors Professor Seymour Laxon and Dr Katharine Giles. Those who loved and worked with them have suffered an irreplaceable loss, and the loss of their expertise has been felt throughout the Polar research community. I'm grateful for the legacy they've left us, and will always strive to do it justice. I also wish to thank them, for seeing a potential in me that I didn't believe I had, and encouraging me to run with it.

Thanks to all who have supervised me along the way: Professor Duncan Wingham, Professor Chris Rapley, Dr Michel Tsamados and Professor Andy Shepherd (for his endless support and expert 'constructive criticism'!)

A special thank you to my friends Tom and Sam. We started our PhDs together and during that time they've made me laugh, made me grumpy, made me shot questionable spirits, made great playlists for long road trips across America (and Cornwall), and generally made me power on through. Thanks as well to CPOMers past and present: Isobel and Alek for being top class office mates, my colleague and friend Andy Ridout without whom none of this would have been possible, and Alan Muir for laughs at the pub and keeping calm when I deleted my IDL license… for the second time.

I'd like to acknowledge those who have supported me from outside of UCL. Thanks to Dr Sinead Farrell for being the best 'cheerleader' going and to Dr Eero Rinne, who entrusted me with the barbecue on the deck of the R/V Aranda, somewhere in the Bay of Bothnia. Most of all, thanks to everyone involved with CryoVEx 2014. I'll treasure the memories of evenings huddled in the mess tent on the Lincoln Sea, with Petter preparing the food and Marc supplying the laughs. Rest easy, Marc. Fieldwork will never quite be the same.

The support from my friends and family has been unwavering. Mum, Dad, Ian, Max, Griff, Nat, Joc, Grace, Gemma, Liz, Chris, and Kevin the whippet – you are all awesome and I love you. Never stop being you!

For Seymour and Katharine

Contents

List of Figures

List of Tables

Commonly used abbreviations and acronyms

Abbreviation	Definition
AWI	Alfred Wegener Institute
BGEP	Beaufort Gyre Exploration Program
CICE	Los Alamos sea ice model
CMIP	Coupled Model Intercomparison Project
CPOM	Centre for Polar Observation and Modelling
CRREL	Cold Regions Research and Engineering Laboratory
DMSP	Defense Meteorological Satellite Program
ERS-1 and -2	European Remote Sensing satellites 1 and 2
ESA	European Space Agency
ESMR	Electrically Scanning Microwave Radiometer
FSIR	Flat Surface Impulse Response
FYI	First Year Ice
GCM	Global Climate Model
ICESat	Ice, Cloud, and land Elevation Satellite
GSFC	Goddard Space Flight Center
IABP	International Arctic Buoy Program
IMB	Ice Mass-balance Buoy
L0	Level 0
L1b	Level 1b
LIM	Louvain-la-Neuve Sea Ice Model
MYI	Multi-year Ice
MCD	Measurement Confidence Data
MSS	Mean Sea Surface
NASA	National Aeronautics and Space Administration
NCAR	National Center for Atmospheric Research
NCEP	National Centers for Environmental Prediction
NMS	Norwegian Meteorological Service
NRT	Near Real Time
NSIDC	National Snow and Ice Data Center
OSI SAF	Ocean and Sea Ice Satellite Application Facility
PP	Pulse Peakiness
ROC	Region of Coverage
SAR	Synthetic Aperture Radar
SARIn	SAR-Interferometric
SIRAL	Synthetic Aperture Interferometric Radar Altimeter (SIRAL)
SLA	Sea Level Anomaly
SMMR	Scanning Multichannel Microwave Radiometer
SSD	Stack Standard Deviation
SSMIS	Special Sensor Microwave Imager/Sounder
SSM/I	Special Sensor Microwave/Imager
SWE	Snow Water Equivalent
THC	Thermohaline Circulation
PIOMAS	Pan-Arctic Ice-Ocean Modelling and Assimilation System
UCL	University College London
ULS	Upward Looking Sonar
WHOI	Woods Hole Oceanographic Institution

1. Sea ice and climate

1.1. Introduction

This chapter acts as an introduction to the Arctic region and its climate. Specifically, the chapter will concentrate on Arctic sea ice and its interactions with the local climate, as well as the wider implications of changes in the Arctic sea ice cover. Modelling efforts and observational records of Arctic sea ice will also be discussed.

1.2. The Arctic climate

1.2.1. Overview of the Arctic climate system

The Arctic is the Polar region surrounding the North Pole. It consists of a large body of water (the Arctic Ocean and peripheral seas) surrounded by land belonging to the United States of America (USA), Canada, Finland, Denmark (in the form of Greenland), Iceland, Norway, Russia, and Sweden. Geographically, the definition of the Arctic region is ambiguous [*Serreze and Barry*, 2005; *Smithson et al.*, 2008] (Figure 1.1). The most common definition of the Arctic is the region that lies above the Arctic Circle – a circumglobal line at approximately 66.56°N. North of the Arctic Circle the Sun does not set on the summer solstice, and does not rise on the winter solstice. Alternatively, the Arctic can be referred to as the area north of the Arctic tree line – the northern limit of tree growth, or as any location in the Northern Hemisphere where the average temperature for the warmest month does not exceed 10°C. For the purpose of this work, the Arctic will refer to the region north of the Arctic Circle.

The Arctic climate experiences a strong seasonal cycle, which is characterised by low amounts or absence of sunlight in winter and long days during summer. The annual mean incoming solar radiation across the Arctic is 100 Wm^{-2} and occurs mostly between the spring and autumn equinoxes. This is compared to mid-latitude regions that receive about 150-200 Wm^{-2} on average [*Przybylak*, 2016]. The Cryosphere – regions where water is in its solid form – is a prominent feature of the Arctic, and is present as ice sheets, glaciers, permafrost, snow, and sea ice.

The Arctic climate system interacts with the global climate through the atmosphere, Arctic Ocean, and peripheral seas. One key connection with lower latitudes is through the Arctic Oscillation (AO). The AO is defined by surface atmospheric pressure patterns, and is a climate pattern characterised by winds circulating counterclockwise

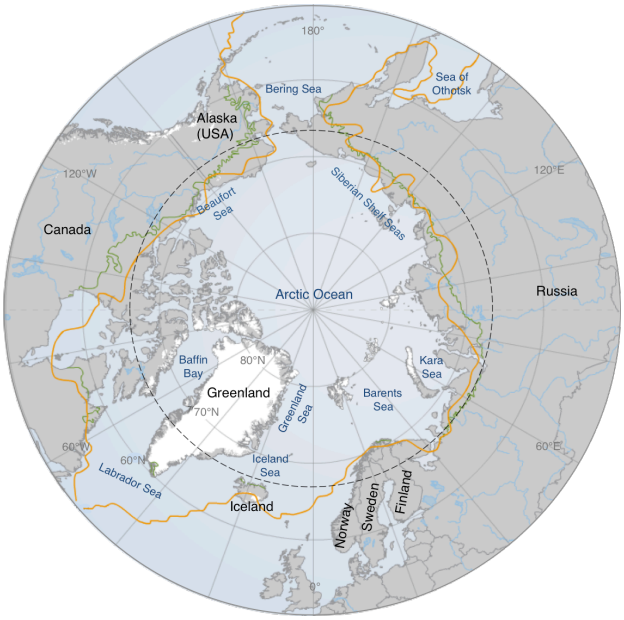

Figure 1.1: Geographical map of the Arctic region. Three Arctic definitions are represented; the Arctic Circle (dashed black line), the Arctic tree line (solid green line), and the 10°C isotherm (solid orange line). Adapted from the Arctic Portal Interactive Map (http://arcticportal.org/maps-heading/maps).

around the Arctic at a latitude of about 45-55°N. When the AO is in its positive phase, surface pressure tends to be lower than normal across the Arctic and higher than normal over the central Atlantic, meaning that strong winds circulate around the North Pole and confine cold air across the Arctic regions. When in its negative phase, surface pressure tends to be higher than normal across the Arctic and lower than normal over the central Atlantic. The winds circulating the North Pole weaken and allow a more southward flow of cold, Arctic air masses, which leads to increased storminess at mid-latitudes [*McBean et al.*, 2004; *Rigor et al.*, 2002]. The phase of the AO was at its most negative in the 1960s. From around 1970 to the early 1990s there was a general trend toward a more positive phase of the AO, which remained mostly positive until the early-2000s, but has oscillated between positive and negative since about 2010 [*NOAA*, 2016]. Closely related to the AO is the North Atlantic Oscillation (NAO). The NAO index is based on the difference in atmospheric sea level pressure (SLP) between two regions in the North Atlantic – an area of low pressure typically located near Iceland, and an area of high pressure over the Azores. During positive phases of the NAO, an increased pressure difference between the Icelandic low and Azores high results in more and stronger winter storms crossing the Atlantic Ocean on a more northerly track. This results in warm and wet winters in Europe and cold, dry winters in northern Canada and Greenland. The eastern USA experiences mild and wet winter

conditions. A negative phase of the NAO is associated with fewer and weaker winter storms crossing on a more west-east pathway. They bring moist air and above-average precipitation into southern and central Europe, and cold air to northern Europe, which experiences below-average precipitation. The eastern USA experiences more cold air outbreaks and snowy weather conditions [*Hurrell*, 1995].

1.2.2. Seasonal evolution of Arctic sea ice

As the water temperature in the Arctic Ocean drops below its freezing point, which for seawater is approximately –1.8°C [*Petrich and Eicken*, 2010], sea ice begins to form. During sea ice formation the hydrogen bonds in the water molecules adjust to hold the negatively charged oxygen atoms apart, which produces a crystal lattice that is less dense than the seawater, and floats on the ocean surface. Sea ice consists of solid ice crystals, along with gaseous air pockets, liquid brine channels, and solid salt and other contaminants [*Wadhams*, 2000].

In the earliest stages of sea ice formation, small crystals form on the ocean surface. These crystals are referred to as frazil ice and have a diameter of 2-3 mm [*Wadhams*, 2000]. As seawater freezes, salt is expelled in a process known as brine rejection. Sea ice therefore has a lower salinity than the surrounding ocean, but is not entirely fresh as some salt can become trapped in small pockets between ice crystals [*Petrich and Eicken*, 2010]. In calm conditions frazil ice crystals combine to form grease ice, then thin, continuous sheets of nilas ice. Following the nilas stage the sea ice grows by congelation growth – a process in which water molecules freeze to the bottom of the ice sheet to form an ice 'floe'. In rough conditions frazil ice crystals combine to form circular, slushy disks referred to as pancake ice. A combination of surface winds, waves and swell force the pancake ice together to consolidate into an ice floe. The state of the sea ice pack is not determined by thermodynamics alone. The ice pack is constantly in motion, driven by wind and ocean currents. This motion can lead to rafting, where sea ice floes slide on top of one another, and also to ridging, where sea ice floes collide and fracture and pile on top of one another (Figure 1.2a). The sails and keels formed by sea ice ridging increase the interaction of the ice with winds and ocean currents [*Martin et al.*, 2016]. The movement of the sea ice pack also causes fractures that result in areas of open water to form between sea ice floes, and these are called leads (Figure 1.2b). These characteristics can help distinguish first year ice (FYI) from multiyear ice (MYI). FYI refers to ice that has not experienced more than one winter growth season. Typically, FYI appears un-deformed and level, and any ridges that do occur are sharp and angular, with little snow cover (Figure 1.2c). MYI refers to sea ice that has survived one or more summer melt seasons. MYI is

characterised by hummocks on the ice surface, and has a greater density of wide ridges and deformation features (Figure 1.2d). MYI ice also contains much less brine and more air pockets than FYI [*Wadhams*, 2000]. The extent of Arctic sea ice varies seasonally, typically reaching its maximum in mid- to late-March and its minimum in mid-September [*Stroeve et al.*, 2014]. It is the growth and melt of FYI in the peripheral seas of the Arctic that most influence seasonal variation in sea ice extent. The thickness of Arctic sea ice varies seasonally and spatially, and ranges from centimetres to metres thick.

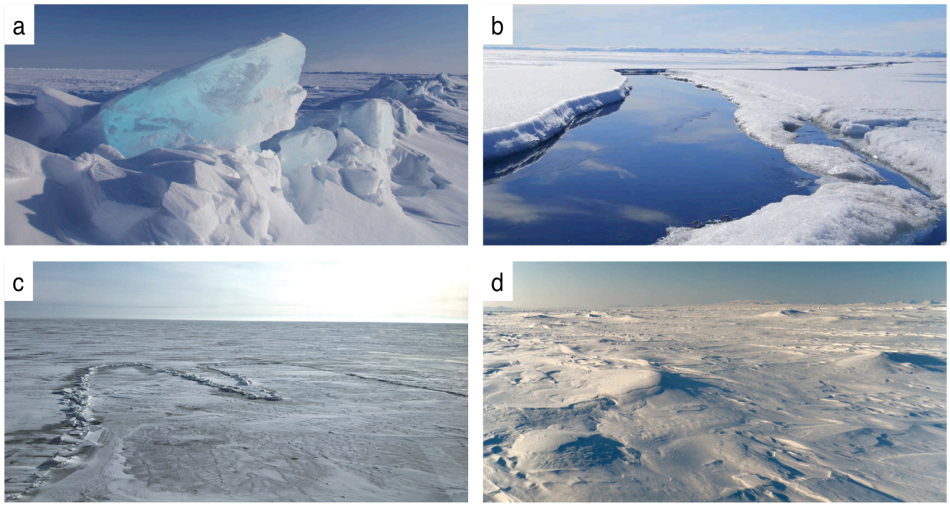

Figure 1.2: Photographs showing different sea ice regimes. (a) A sea ice ridge (photo credit: Seymour Laxon). (b) A sea ice lead (photo credit: shutterstock). (c) First year sea ice. (d) Multiyear sea ice (photo credit: Kyle O'Donoghue).

1.2.3. Changes in the Arctic climate system

Global mean surface temperature (GMST) increased by an average of 0.85°C over the 132-year period between 1880-2012. The rate of this increase was, on average, 0.06°C decade^{-1} from 1880-2012. The rate of increase rose abruptly to 0.16°C decade^{-1} over the period 1979-2012, meaning that the 33-year period is responsible for 0.50°C of the increase in GMST since the 1880s (e.g. Figure 1.3), according to the Intergovernmental Panel on Climate Change (IPCC) [*Hartmann et al.*, 2013]. The datasets used by the IPCC were the National Oceanic and Atmospheric Administration (NOAA) Merged Land–Ocean Surface Temperature (MLOST) dataset [*Vose et al.*, 2012], the UK Met Office HadCRUT4 dataset [*Morice et al.*, 2012], and the National Aeronautics and Space Administration (NASA) Goddard Institute for Space Studies (GISS) surface temperature dataset [*Hansen et al.*, 2010]. The global surface

temperature datasets used by the IPCC show that over the period 1979-2012, the Arctic mean surface temperature increased at almost twice the global average rate (e.g. Figure 1.3) – a phenomena known as Arctic amplification.

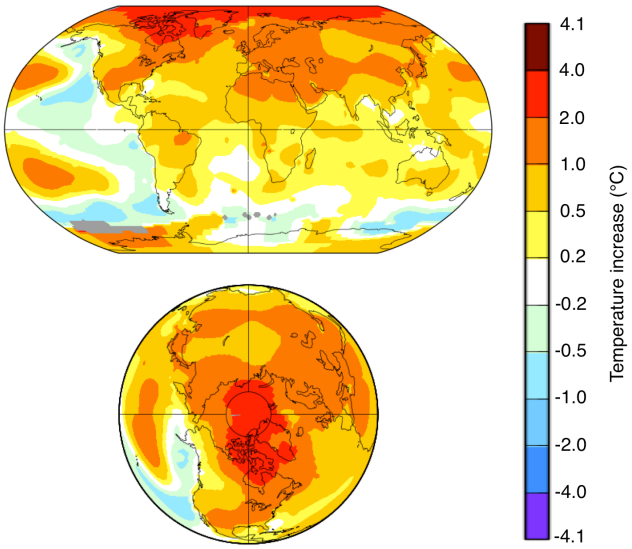

Figure 1.3: Global mean surface temperature (GMST) increase, 1979-2012. Produced using data from the National Aeronautics and Space Administration (NASA) Goddard Institute for Space Studies (GISS) surface temperature dataset [*GISTEMP*, 2015; *Hansen et al.*, 2010].

A number of studies show that the observed increase in Arctic mean surface temperature is not consistent with internal climate variability or natural climate drivers alone [*Chylek et al.*, 2014; *Gillett et al.*, 2008; *Najafi et al.*, 2015; *Wang et al.*, 2007], and the IPCC state that there is sufficiently strong evidence to conclude that anthropogenic influences have contributed to the "very substantial" Arctic warming since the mid-20th century [*Bindoff et al.*, 2013].

For all CO_2 emission scenarios proposed by the IPCC, the global climate models (GCMs) in their fifth assessment report each predicted that the Arctic mean surface temperature will continue to increase more rapidly than the global mean during the 21st century. Each model run incorporates one of four Representative Concentration Pathway (RCP) emission scenarios – RCP2.6, RCP4.5, RCP6.0 or RCP8.5. The RCPs describe four possible radiative forcings (RFs) that are considered possible depending on future greenhouse gas emissions. RCP2.6 stabilises RF at 2.6 Wm^{-2} in 2100 and does not exceed that value, and so on. The increase of Arctic mean surface

temperature for 2081-2100 relative to 1986-2005 is projected to be between 2.2-2.4 times greater than the global mean, for RPC 2.6 and RCP6.0, respectively. This corresponds to an Arctic temperature increase of between 2.2 and 8.3°C [*Collins et al.*, 2013].

1.2.4. Sea ice in a changing Arctic climate

Publications regarding the response of the Arctic sea ice system to a warming climate began to appear in the mid-1970s [*Sanderson*, 1975]. By the mid-1980s a number of teams were working to observe how the sea ice cover was changing using data from submarine upward looking sonar (ULS) [*McLaren*, 1989; *Wadhams*, 1990] and remote sensing aircraft [*Wadhams et al.*, 1991]. Passive microwave satellites were utilised to observe changes in the Arctic sea ice cover as early as 1973 [*Parkinson and Cavalieri*, 1989], although the availability of satellite data was temporally sporadic until 1978 [*Stroeve et al.*, 2012a]. Arctic-wide satellite observations are crucial for understanding how the sea ice system as a whole has responded, and is currently responding, to increasing temperatures.

Satellites have observed a decline in Arctic sea ice extent for all months since 1979, coincident with the abrupt Arctic warming [*Stroeve et al.*, 2014]. The decline is weakest in the Arctic winter months of February-April, around which time Arctic sea ice extent reaches its maximum each year. The date of the sea ice maximum varies considerably and has occurred as early as February 24th in 1996 and as late as April 2nd in 2010. The average rate of decline for February-April extent was 2.7% decade^{-1} from 1979-2016, and the lowest maximum extent of 14.52 million km^2 occurred on March 24th 2016. The decline in Arctic sea ice extent is strongest in September (Figure 1.4), when Arctic sea ice extent reaches its minimum each year. September sea ice extent decreased by 13.4% decade^{-1} from 1979-2015, resulting in a record minimum ice extent of 3.41 million km^2 on September 16th 2012 [*Fetterer et al.*, 2002, updated daily].

1.3. Influence of Arctic sea ice on the global climate system

The Arctic is a major element of the Earth's climate system, and its sea ice cover acts to regulate solar absorption, ocean-atmosphere heat exchange, and freshwater input into the Arctic Ocean and subpolar North Atlantic. This section describes how changes in the Arctic sea ice cover impact on regional heat and freshwater budgets, and on subsequent patterns of atmospheric and oceanic circulation across the Arctic and at lower latitudes.

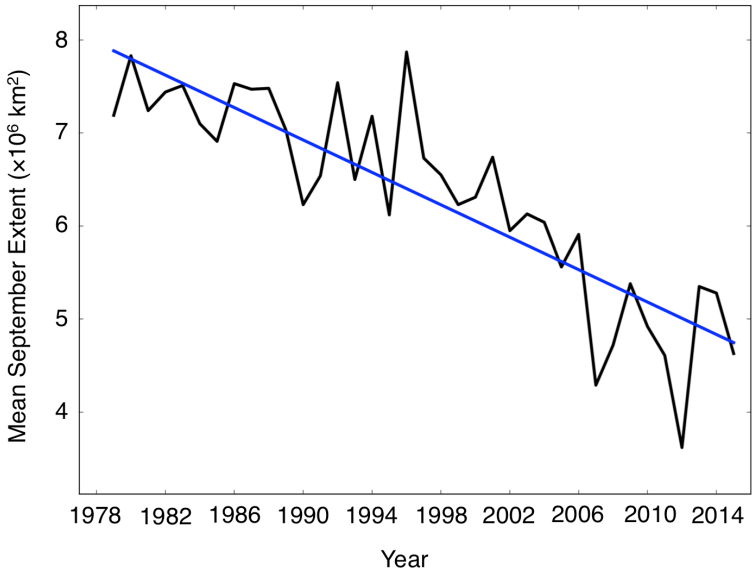

Figure 1.4: Mean September Arctic sea ice extent, 1979-2015. Adapted from the National Snow and Ice Data Center (https://nsidc.org/arcticseaicenews/2015/10/).

1.3.1. The Arctic heat budget

The observed decline in Arctic sea ice extent provides a positive feedback on Arctic surface temperature, through the surface-albedo feedback. The high albedos of sea ice and snow act to reflect incoming shortwave solar radiation – their retreat therefore reduces the surface albedo of the Arctic Ocean and leads to an increase in absorption of solar radiation by the ocean. This results in ocean warming, and an increase in surface air temperature through ocean-atmosphere heat exchange. The absorption of solar radiation by the ocean is most pronounced in the summer months, when the level of radiation is high and the albedo of the sea ice cover (Figure 1.5) reaches its minimum. By mid-July, much of the sea ice snow cover has melted, except over the thickest ice (usually MYI), leaving bare ice with a low albedo. The albedo of sea ice reaches its minimum when the melt pond fraction reaches its maximum, and by mid-August melt ponds begin to refreeze and the sea ice albedo increases [*Curry et al.*, 1995; *Perovich and Polashenski*, 2012; *Perovich et al.*, 2007]. The surface-albedo feedback is only active in a direct sense when solar radiation is present over the Arctic [*Screen and Simmonds*, 2010b]. However, the amount of heat absorbed by the Arctic Ocean during sunlit periods influences ocean-atmosphere heat exchange in darker periods, and if sufficient solar radiation is absorbed in summer then this will limit sea ice growth during the following autumn and winter periods [*Serreze and Francis*, 2006].

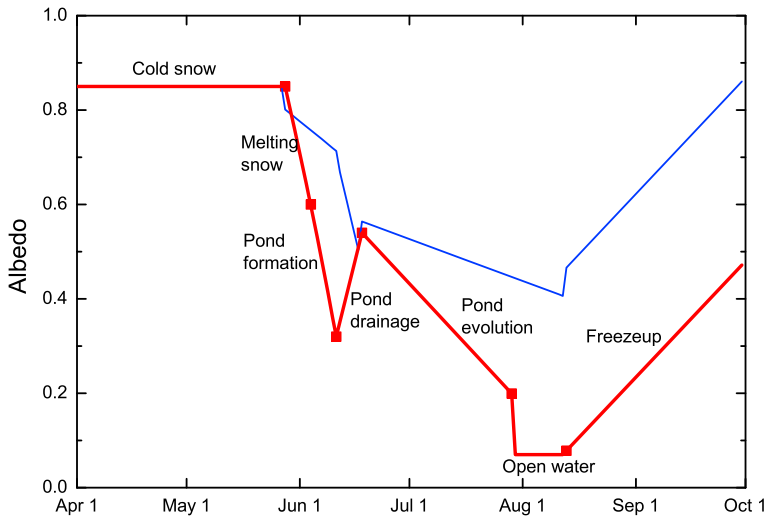

Figure 1.5: Melt season evolution of Arctic sea ice albedo. Estimated from measurements of the optical properties of multiyear ice (blue line) during the 1997-1998 Surface HEat Budget of the Arctic Ocean (SHEBA) experiment, and of seasonal shorefast ice (red line) near Barrow, Alaska over the 2008-2011 melt seasons. From *Perovich and Polashenski* [2012].

The surface-albedo feedback is often cited as the main contributor to the observed Arctic amplification of global warming trends [*Screen and Simmonds*, 2010a; *Serreze and Francis*, 2006; *P C Taylor et al.*, 2013], although a number of factors have likely contributed, and there is still disagreement over which has the most influence overall. For example, *Winton* [2006] analysed the output of 12 climate models from the IPCC fourth assessment report and concluded that the most significant contribution to Arctic warming is an increase in cloud cover – a consequence of rising ocean temperature and atmospheric humidity – which trap shortwave and longwave radiation and subsequently enhance downward radiation to the surface. For most of the year, this acts to warm the surface. However, for a brief period in the middle of summer, the cloud drives a cooling of the surface by reflecting a greater fraction of solar radiation than would be reflected by the sea ice surface in clear conditions [*Intrieri et al.*, 2002]. *Graversen and Wang* [2009] also found that the warming influence of water vapour and clouds are especially important in the Arctic.

Pithan and Mauritsen [2014] analysed the relative contributions to Arctic amplification in models of the surface-albedo feedback and water vapour and cloud radiative feedbacks. They also considered the contributions of the lapse-rate feedback and

changes in atmospheric and oceanic heat transport. Lapse-rate is the rate at which atmospheric temperature decreases with height in the troposphere. Since emission of infrared radiation varies with temperature, longwave radiation escaping to space from the relatively cold upper troposphere is less than that emitted toward the ground from the lower troposphere. As GMST rises the temperature at low latitudes is predicted to increase throughout the troposphere, but more so in the upper troposphere due moist convective processes, leading to a decrease in lapse rate. This induces a negative lapse-rate feedback as the system loses more energy to space. However, in the Polar Regions, there exists a stable atmospheric stratification that effectively confines surface-based warming to the lower atmosphere, increasing the rate of temperature decrease with height and therefore the lapse-rate. This induces a positive lapse-rate feedback as surface warming is amplified [*Goosse*, 2015]. The *Pithan and Mauritsen* study found the positive lapse-rate feedback of the Arctic to be the largest contributor to Arctic amplification. However, *Graversen et al*. [2014] analysed the output from a different suite of models and found that the contribution of the surface-albedo feedback accounted for a larger fraction of Arctic amplification than the lapse-rate feedback.

Arctic warming is also amplified by an increase in ocean-atmosphere heat exchange due to a warming ocean. The heat exchange (via the turbulent fluxes of sensible and latent heat) is strongest in autumn and winter when the amount of solar radiation is reduced or absent, and weakest in summer, when the rise in surface air temperature is limited by a net downward surface heat flux caused by increased solar radiation, sea ice melt, and ocean warming [*R W Lindsay and Zhang*, 2005; *Serreze and Barry*, 2011]. This warming is highly dependent on the state of the Arctic sea ice cover, as its insulating influence impacts on the magnitude of the heat exchange. The heat exchange is therefore affected by the ice thickness as well as extent. It has been estimated that the wintertime ocean-atmosphere heat exchange in the Arctic can vary by nearly two orders of magnitude between open water and thin ice regions, compared to thick MYI regions [*Kurtz et al*., 2011]. In summary, Arctic amplification is driven by a complex balance of forcings and their associated feedbacks, many of which are seasonal. To understand the influence of the Arctic sea ice cover on the regional heat budget, it is necessary to observe changes in the ice thickness, as well as extent.

Changes in the Arctic heat budget are likely to be felt globally. The Arctic is experiencing a significant increase in surface air temperature. This is most notable over regions that are now ice free in summer but historically have not been, as the reduction in sea ice cover increases the latent heat exchange between the ocean and atmosphere. These areas of reduced ice extent and increased atmospheric

temperature are associated with anomalously low SLP [*Alexander et al.*, 2004]. These temperature and pressure changes will alter the vertical stability of the atmosphere by weakening the near-surface stratification of the lower atmosphere [*Schweiger et al.*, 2008; *Singarayer et al.*, 2006], and will also alter latitudinal temperature and pressure gradients [*J A Francis and Vavrus*, 2012]. The global response to these changes depends on the interaction between the anomalous surface fluxes and the large-scale circulation [*Alexander et al.*, 2004], and the way in which the altered latitudinal gradients modify the dynamical atmospheric field that connects the Arctic to the lower latitudes [*Dethloff et al.*, 2006; *J A Francis et al.*, 2009]. For example, autumn SLP fields following low ice-extent summers exhibit higher pressures over much of the Arctic Ocean and North Atlantic, which are compensated by lower pressures in the mid-latitudes. This pressure pattern is similar to the negative phase of the NAO (Section 1.2.1), which results in warm air and increased precipitation in southern and central Europe, cold air and lower precipitation in northern Europe, and cold air and snowy outbreaks in the eastern USA. It has also been suggested that the differential warming of the Arctic and associated circulation changes could lead to Northern Hemisphere atmospheric circulation patterns favouring persistent weather conditions in mid-latitudes. This could impact on the climate in Europe, America and much of the Northern Hemisphere through, for example, an increase in heavy snowfall [*J Liu et al.*, 2012], changes in evaporation and rainfall patterns [*Sewall and Sloan*, 2004; *Singarayer et al.*, 2006], and an increase in extreme weather events such as drought, flooding, prolonged cold spells, and heat waves [*J A Francis and Vavrus*, 2012; *J A Francis and Skific*, 2015]. While there is no definitive agreement regarding the spatial patterns of change that will emerge, a number of modelling studies find that changes in the Arctic heat budget will be felt globally, and that the impacts may be significant.

1.3.2. The Arctic freshwater budget

The Arctic freshwater budget modulates the freshwater supply from the Arctic Ocean to the subpolar North Atlantic, which is a key region in the formation of the global THC. In the North Atlantic, winter atmospheric cooling increases the density of upper-ocean water to the point where it sinks to the bottom and flows southward, forming the lower limb of the THC. The THC influences global climate by transporting heat from the tropics, through the Atlantic Ocean to the mid-latitude Northern Hemisphere, and back to the Arctic (Figure 1.6). During winter, this heat is released to the overlying atmosphere of northern Europe, where winter temperatures are milder than other places at similar latitudes [*Broecker*, 1997].

Changes in Arctic sea ice volume, through the growth and melt of Arctic sea ice, influence the Arctic freshwater budget and vary the amount of salt and freshwater supplied to the subpolar North Atlantic. When salt is rejected during sea ice freeze-up, the water below the ice becomes more dense than its surroundings and sinks, thus contributing to the THC. However, melting of the permanent, MYI Arctic sea ice cover has the potential to input large quantities of freshwater into the North Atlantic. The lower density of freshwater relative to saline water prevents the sinking of water masses, which may in turn weaken the THC [*Broecker*, 1997; *Lohmann and Gerdes*, 1998; *Saenko et al.*, 2004]. The influence of Arctic sea ice melt on the THC is further complicated by the fact that sea ice retreat allows more oceanic heat loss, which acts to strengthen and stabilise the THC [*Levermann et al.*, 2007]. However, despite its stabilising impact, the high-latitude ocean cooling associated with sea ice retreat and thinning cannot compensate for the freshening associated with sea ice melt [*Lohmann and Gerdes*, 1998]. This is because the effects of temperature on density are very much smaller in cool, polar waters than in warmer parts of the globe due to the nonlinearity in the equation of state [*Prange et al.*, 1997; *Winton*, 1997]. Overall, the THC is generally projected to weaken over the next century, although the fifth assessment report of the IPCC states that the rate and magnitude of weakening is uncertain, based on the output of a suite of GCMs [*Kirtman et al.*, 2013]. A weakened THC will lead to subsequent regional cooling in the United Kingdom and northwest Europe and there is also the possibility of coincident weak warming in the southern hemisphere [*Vellinga and Wood*, 2002].

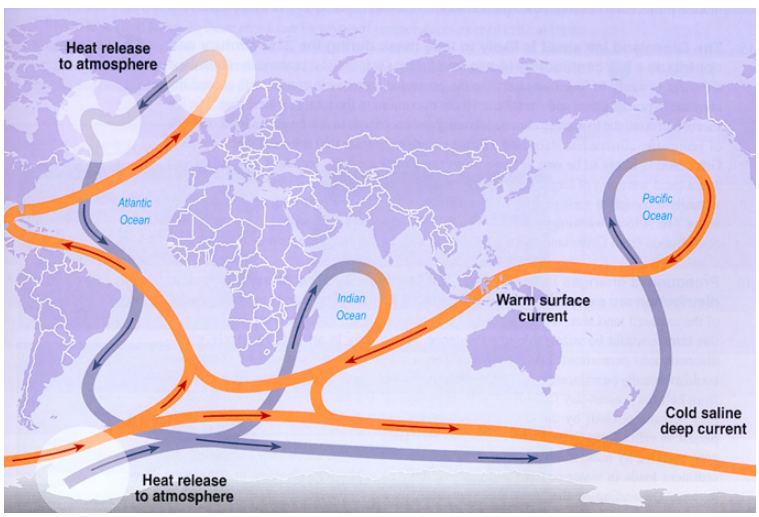

Figure 1.6: The global thermohaline circulation (THC). From *Albritton et al.* [2001].

Arctic freshwater content and freshwater supply to the subpolar North Atlantic could also be affected by changes in the strength of the sea ice cover and its affect on momentum transfer from the atmosphere to ocean. One example of this is in the western Arctic Beaufort Gyre region. The Beaufort Gyre is the major reservoir of freshwater stored in the Arctic Ocean. It has been estimated that the volume of freshwater stored in the gyre is 10-15 times larger than the total annual river runoff to the Arctic Ocean, and at least two times larger than the amount of freshwater stored in the sea ice [*Proshutinsky et al*., 2009]. Between 1995 and 2010, *Giles* [2012] observed a steepening of the dome in sea surface height associated with the gyre, indicating gyre spin-up and an increase in freshwater storage of 8,000 ± 2,000 km^3 in the western Arctic Ocean. The Arctic winds were more effective at spinning up the gyre during the 2000s compared to the 1990s, suggesting that the efficiency of the transfer of momentum from the atmosphere to the ocean had increased. A possible explanation is that the mechanical strength of the sea ice cover decreased due to a decrease in ice thickness, making it easier to move and deform. An increase in ice deformation results in more leads and ridges, increasing the area of vertical surfaces the wind can blow against, which increases the momentum transfer to the sea ice and ocean below. It is possible that future changes in the Arctic wind field and its interaction with the sea ice cover could lead to a spin-down of the Beaufort Gyre, and release of its freshwater content to the Arctic Ocean. To fully understand how changes in the Arctic sea ice cover impact on the Arctic freshwater budget and subsequent global ocean circulation and climate, long-term and accurate observations of sea ice thickness, as well as extent, are required.

1.4. Wider influences of Arctic sea ice

1.4.1. Arctic biology

Changes in the Arctic ecosystem are projected if the current rate of sea ice decline is sustained. *Laidre et al*. [2008] developed a sensitivity index based on nine variables that they felt have the most influence on the response and vulnerability of Arctic marine mammals to climate change. One of these variables was sensitivity to changes in sea ice. They found that two of the most sensitive Arctic marine mammals species are the hooded seal and polar bear, primarily due to their reliance on sea ice cover. Hooded seals live on drifting pack ice when not in deep water, and polar bears depend on sea ice for hunting, breeding, and movement. A 2007 research study by the United States Geological Survey (USGS) projected that around two-thirds of the polar bear population could die out by 2050 if greenhouse gas emissions and sea ice loss

continue at their current rate [*Amstrup et al.*, 2010]. This is primarily due to a reduction in adult female survival and secondarily to a reduction in breeding [*Hunter et al.*, 2010]. The least sensitive species in the USGS study were the ringed seal and bearded seal. Both species have an Arctic-wide distribution and large population, and their flexible habitat requirements allow them to adapt more easily to changes in sea ice cover. The Arctic sea ice cover also influences the amount of primary production in the Arctic Ocean. Primary production is the synthesis of organic compounds from atmospheric or aqueous carbon dioxide and in the ocean it principally occurs through photosynthesis by phytoplankton. Arctic wide primary production increased by an average of 27.5 Tg of carbon year^{-1} from 2003-2007. This increase was primarily due to an increase in the phytoplankton growth season caused by sea ice reduction and a greater availability of light [*Arrigo et al.*, 2008]. Work is still required to determine the dependence of the timing, distribution and magnitude of phytoplankton primary production on sea ice extent and thickness [*Arrigo et al.*, 2012], and how such changes could affect the structure of the Arctic marine ecosystem [*Arrigo et al.*, 2008; *Arrigo et al.*, 2012].

1.4.2. Arctic indigenous communities

Indigenous Arctic communities rely, to varying degrees, on the surrounding sea ice cover for their lifestyle and livelihood. This reliance is based heavily on transportation opportunities and access to food, both of which are changing with the changing Arctic landscape [*White et al.*, 2007]. For example, Yupik hunters indigenous to St. Lawrence Island, Alaska, have observed a shift in the sea ice regime from stable pack ice to thinner, less stable ice, which has diminished their ability to hunt and fish [*Grebmeier et al.*, 2006]. Similarly, members of the community of Nain in northern Labrador, Canada have reported that changes in the quality and strength of the sea ice has impacted on their ability to fish, hunt for caribou and seal, and improve their food supply with healthy wild food. The community also relies on sea ice for transport to school, accessing places of cultural significance, and to visit friends and family, for example. But members of the community feel that their ability to safely navigate the sea ice has been hampered by changes in its quality and strength [*Durkalec et al.*, 2015].

Changes in Arctic sea ice do not just affect the physical health and lifestyle of Arctic communities. Members of the community of Nain also described the mental and emotional benefits of sea ice travel, stating that it is “good for your spirit”, makes your “soul feel better”, makes you feel “rejuvenated”, and provides motivation and a sense of purpose [*Durkalec et al.*, 2015]. *MacDonald et al.* [2015] carried out interviews with youth aged 15-25 from communities of the Nunatsiavut region of Labrador, Canada and identified five key factors that appear to enhance mental health and wellbeing.

These were: being on the land, connecting to Inuit culture, belonging to a strong community, relationships with family and friends, and keeping busy. The changes in Labrador Sea ice cover are compromising these factors by reducing land access and increasing the danger of sea ice-based activities. Mental health is likely to become an emerging problem Arctic-wide [*Willox et al.*, 2015] and many are encouraging an increased effort to respond through research, policy, and improved mental health care [*Doherty and Clayton*, 2011; *Swim et al.*, 2010; *Willox et al.*, 2015].

1.4.3. Operational services in the Arctic region

There is increasing interest in the behaviour of Arctic sea ice among operational services, with a growing need for accurate and timely information of regional sea ice location, thickness and drift. For example, shipping through the Arctic Ocean via the Northern Sea Route could save about 40% of the sailing distance from Asia (Yokohama) to Europe (Rotterdam) compared to the traditional route via the Suez Canal [*M Liu and Kronbak*, 2010], which would quicken the regional export of natural resources, and delivery of cargo to the communities along the Siberian coast [*Meier et al.*, 2014]. Ease of passage is also a concern for those looking to ship along the Northwest Passage and potential future trans-Arctic shipping routes along the Russian coast, and when considering the potential for tourism in regions such as Canadian Arctic waters [*Stewart et al.*, 2007]. Ships navigating through sea ice require an ice class [*IACS*, 2016], meaning that their hull must be strengthened depending on the state of the sea ice that they are traversing. Higher ice classes have higher building costs [*M Liu and Kronbak*, 2010] so accurate and timely sea ice thickness data have the potential to benefit all ship-based operations in the Arctic. The oil and gas sector require hemispheric studies of sea ice concentration, extent, motion and thickness [*Galley et al.*, 2013] to estimate productions costs and to assess the feasibility and safety of replacing ice-based construction with lower cost conventional construction equipment [*Harsem et al.*, 2011]. As a consequence many large oil companies are reducing their plans for Arctic exploration and drilling activities due to the high costs and risks, which will impact on northern areas and communities through local businesses who report losses in hotel revenues, restaurant businesses, and the local marine support [*Meier et al.*, 2014]. Up-to-date measurements of sea ice thickness are crucial when considering building specifications and costs for exploration platforms and ice-classed ships, transit speeds, and navigation difficulties and risks.

1.5. Modelling the Arctic

Climate models are commonly used to investigate the behaviour of Arctic sea ice, to explore relationships between the Arctic and global climate, and to form the basis of future Arctic and global climate projections. Climate models can be regional or global and vary in their complexity and model resolution depending on their purpose [*Randall et al.*, 2007].

1.5.1. Hierarchy of climate models

The most basic models propose a highly simplified version of the dynamics of the climate system, as a number of physical processes are not explicitly included, and are not accounted for by model parameterisations. The resolution of simple climate models tends to be relatively coarse, meaning that input and output parameters are averaged over large regions and often the entire Earth. One basic model type is the Energy Balance Model (EBM). These models do not attempt to resolve the dynamics of the climate system, such as atmospheric circulation systems or ocean currents, and simply focus on the energy transfers and thermodynamics of the climate system. EBMs can be global [*Sato*, 2014; *Sellers*, 1969; *Yan et al.*, 2012], or cover a specific area, such as mountain glaciers [*Hock and Holmgren*, 2005] or cities [*Yan et al.*, 2012].

Intermediate complexity models can be used to assess the relative impact of different processes on a specific area of the climate system. These models are applied to certain scientific questions such as understanding climate feedbacks on millennial time scales when long model integrations are required, or investigating the impact of a changing climate on the Polar Regions. For example, simple one-dimensional models of sea ice have been used in the past to investigate the response of sea ice to a number of climate forcing factors in the Arctic [*Ebert and Curry*, 1993] and the Antarctic [*Petty et al.*, 2013]. Models representing different aspects of the Earth's climate such as sea ice, cloud cover, and the ocean mixed layer, can be coupled together to further investigate changes in a specific system. Whilst these approaches are helpful in understanding the mean behaviour of a system, they do not capture the spatio-temporal complexity of the responses and ignore feedbacks between the atmosphere, ice and ocean [*Tsamados et al.*, 2015].

GCMs, such as ocean and atmosphere GCMs (OGCMs and AGCMs, respectively), aim to account for key processes of the climate system at the highest affordable resolution, on a global scale. However, such models often remain too simplified in representing the physics of certain components of the climate system. Therefore, the

most comprehensive and complex climate models involve coupling GCMs together, for example in a fully couple ocean-atmosphere GCM (AOGCM), or coupling GCMs with models that aim to accurately model one component of the Earth system at high resolution. These specialised models include models of ice sheet dynamics, land-surface processes and sea ice processes [*Goosse*, 2015]. One example is the Los Alamos sea ice model (CICE). CICE is a computationally efficient sea ice model that has several interacting components including a thermodynamic model that computes local growth rates of snow and ice, radiative and turbulent fluxes, snowfall, ice dynamics, and a ridging parameterisation [*Hunke et al.*, 2015]. Another example is the Louvain-la-Neuve sea ice model (LIM) – a numerical model of sea ice designed for climate studies and operational oceanography [*Vancoppenolle et al.*, 2009]. The key parameters that LIM outputs are sea ice thickness, enthalpy, salinity and age distribution.

Many coupled models can relate dynamic and thermodynamic processes of the Arctic region and global climate processes [*Holland et al.*, 2010], and can provide insight into the degree to which the model sea ice trends reflect anthropogenic forcing versus internal climate variability [*Stroeve et al.*, 2012b]. In 1995 the World Climate Research Programme (WCRP) launched the Coupled Model Intercomparison Project (CMIP). The project is ongoing and its objective is to better understand past, present and future changes in the global climate arising from either natural variability or anthropogenic forcing by using a multi-model output from coupled models. The models participating in CMIP are run a number of times from different starting conditions to provide a set of forecasts known as an ensemble. The spread in output from ensemble members is useful when investigating the future and predictability of the climate system from different climate states [*Meehl et al.*, 2014]. A number of the CMIP models have been used in IPCC reports to investigate the sensitivity of various aspects of the global climate, such as global air temperature and ocean circulation, to different $C0_2$ emission scenarios [*Collins et al.*, 2013; *Kirtman et al.*, 2013].

1.5.2. Arctic sea ice in climate models

The CMIP model outputs are useful for assessing the fidelity of model representation of historical sea ice cover, and the reliability of sea ice projections. There is disagreement between CMIP models over the rate at which Arctic sea ice extent has declined over the satellite era [*Holland et al.*, 2010; *Stroeve et al.*, 2007; *Stroeve et al.*, 2012b], as well as the timescale over which the Arctic will become sea ice free (defined as one million square kilometres or less in summer) [*Overland and Wang*, 2013; *Stroeve et al.*, 2012b]. *Stroeve et al.* [2012b] performed an in-depth comparison of 56 ensemble

members from 20 of the coupled models participating in CMIP Phase 5 (CMIP5) [*K E Taylor et al.*, 2012]. Each of the model runs evaluated incorporated RCP4.5 emission scenario, which is one of four RCPs adopted by the IPCC for their fifth assessment report in 2013 (Section 1.2.3). Most of the CMIP5 ensemble members underestimated the rate of September ice extent decline between 1979-2011, although trends varied considerably. Of the 56 ensemble members, 50 had rates of decline that were slower than observed by satellite, six had rates of decline larger than observed, 46 had trends outside of the 2σ uncertainty bound of observations, and nine had trends that were statistically indistinguishable from zero. In relation to ice-free conditions, the CMIP5 multi-model ensemble mean did not reach ice-free conditions in September by the end of this century, although 32% of the individual ensembles did. Six of the models reached ice-free conditions by 2050 and one model – the Canadian Earth System Model 2 (CanESM2) – had an ensemble member that was ice-free by 2016. Based on the CMIP5 multi-model ensemble mean, approximately 60% of the rate of decline in September sea ice extent from 1979–2011 is due to anthropogenic forcing rather than internal climate variability [*Stroeve et al.*, 2012b].

The inter-model differences in CMIP5 sea ice trends may be due to the model complexities and the different ways in which sea ice and climate processes, and their interactions, are treated in the models [*Eisenman et al.*, 2007; *Tao et al.*, 1996]. The behavior of sea ice is dependent on multiple complex factors [*Notz*, 2012] that are not easily observed or incorporated into coupled models. These include mechanical properties such as floe redistribution, ice ridging [*Hunke*, 2010], ice deformation [*Feltham*, 2008; *Tsamados et al.*, 2013], and drag between the ice and atmosphere and the ice and ocean [*Hunke*, 2014; *Tsamados et al.*, 2014]. Other factors include melt pond fraction [*Flocco et al.*, 2010; *Pedersen et al.*, 2009; *Schroeder et al.*, 2014], oceanic heat flux, ice conductivity [*Hunke*, 2010], and brine drainage [*Worster and Jones*, 2015]. The behavior of sea ice is also dependent on climate processes such as ocean circulation [*Kwok*, 2011], winds [*Smedsrud et al.*, 2011], and thermodynamic forcing [*Kwok and Cunningham*, 2015; *Tilling et al.*, 2015]. Model inclusions or improvements of some of these processes could lead to better representation of historical sea ice conditions and future projections.

To analyse Arctic sea ice volume trends in coupled models, *Holland et al.* [2010] selected the 14 models from CMIP Phase 3 (CMIP3) [*Meehl et al.*, 2007] that output sea ice thickness as well as extent. They found that for the period 2000-2100, all the models predicted a decrease in Arctic sea ice volume resulting from an increase in the annual net melt of ice. However, there was significant disagreement over the rate at

which sea ice volume will decrease over the 21st century and the magnitude of ice volume loss. Such inter-model differences highlight the need for Arctic-wide observations of sea ice thickness and volume, as these can be used to assess the fidelity of the various climate models that form the basis of future climate projections.

The models that participated in CMIP3 and CMIP5 are long-term predictive models and do not assimilate sea ice data, but there are a small number of more specialised models that do. In Europe, the Mercator-Ocean model [*Drevillon et al.*, 2008] is a global ocean forecasting system that assimilates sea ice concentration data from Special Sensor Microwave/Imager (SSM/I) instruments on-board the Defense Meteorological Satellite Program (DMSP) suite of satellites. It outputs parameters including ocean temperature, ocean salinity, ice concentration, ice velocity and ice thickness. Mercator-Ocean is the French contribution to the Marine Environment and Security for the European Area (MERSEA) project for operational systems [*Desaubies*, 2006] and the Global Ocean Data Assimilation Experiment (GODAE) project [*GODAE*, 2008]. The Arctic and North Atlantic component of the MERSEA project, and also a contributor to the GODAE project, is the TOPAZ model [*Bertino and Lisaeter*, 2008; *Sakov et al.*, 2012]. TOPAZ is a coupled ocean-sea ice data assimilation system that utilises sea ice concentration data from the Advanced Microwave Scanning Radiometer (AMSR-E) on-board the Earth Observing System (EOS) Aqua satellite. It outputs sea ice parameters including ice concentration, ice drift and ice thickness. Both Mercator-Ocean and TOPAZ are operational as part of the Copernicus Marine Environmental Monitoring Services (CMEMS) [*CMEMS*, 2014].

In addition to TOPAZ, there are also specialised sea ice models that have been developed in the USA that assimilate sea ice data. The Pan-Arctic Ice-Ocean Modelling and Assimilation System (PIOMAS) was developed especially to estimate sea ice volume changes on a continuous basis but not to predict future sea ice conditions. PIOMAS couples a global ocean model to a sea ice model whose grid emphasizes the Arctic Ocean and that assimilates sea ice data by including measurements of near real time (NRT) sea ice concentration and velocity. PIOMAS does not use an atmospheric model and instead assimilates atmospheric information to drive the model from National Centers for Environmental Prediction/National Center for Atmospheric Research (NCEP/NCAR) reanalysis data [*Schweiger et al.*, 2011; *Zhang and Rothrock*, 2003]. PIOMAS has shown good agreement with observations of sea ice volume in the high-Arctic region derived from satellite observations [*Laxon et al.*, 2013]. However, it is not yet a sufficient tool for predicting future changes in Arctic sea volume due to its dependence on historical observations. The U.S. Navy's Arctic

Cap Nowcast/Forecast System (ACNFS) also assimilates sea ice data [*Hebert et al.*, 2015; *Posey et al.*, 2015]. ACNFS is designed to provide short-term (1–7 day) forecasts of Arctic sea ice and ocean conditions, and does so by assimilating NRT sea ice concentration data blended from the Advanced Microwave Scanning Radiometer (AMSR-2) on-board the Global Change Observation Mission - Water (GCOM-W) satellite, and the Interactive Multisensor Snow and Ice Mapping System (IMS). The quantities forecast by ACNFS include sea ice concentration, sea ice thickness, sea ice velocity and sea surface temperature [*Hebert et al.*, 2015]. To assess the ACNFS model output, *Hebert et al.* [2015] compared Arctic sea ice concentration forecast skill to forecast skill using a persistent sea ice state and a historical sea ice climatology. They found that ACNFS forecasts are skillful compared to assuming a persistent ice state and climatological ice state, particularly for forecasts beyond 24 hours and up to 102 hours, respectively. The developers of ACNFS are currently working to further develop its sea ice concentration and thickness forecast skill by assimilating NRT Arctic sea ice thickness data provided by the Centre for Polar Observation and Modelling (CPOM) at University College London (UCL). To evaluate the ACNFS model ice thickness fields, *Allard et al.* [2016] have compared the model ice thickness output to thickness data from Woods Hole Oceanographic Institution (WHOI) ULS buoys, Cold Regions Research and Engineering Laboratory (CRREL) ice mass-balance buoys (IMBs) [*Richter-Menge et al.*, 2006], and NASA's Operation IceBridge [*Kurtz et al.*, 2013], with and without the assimilation of archive sea ice thickness data provided by CPOM UCL. The evaluation has shown that in all cases the model mean thickness is positively biased with respect to observational data, but that the assimilation of CryoSat-2 thickness data reduced the bias by an average of 69%, 41% and 43% when comparing model output to WHO ULS data, CRREL IMB data, and NASA Operation IceBridge data, respectively. The development and interpretation of the CPOM UCL archive and NRT sea ice thickness products, which are provided directly to the U.S. Navy for use with their ACNFS model, constitute the basis of this thesis.

1.6. Observations of Arctic sea ice

1.6.1. Arctic sea ice extent

Knowledge of Arctic sea ice extent in past geologic eras relies on proxy records, such as preserved sediment on the floor of the Arctic Ocean and peripheral seas. Sediment cores can consist of the skeletons of microscopic organisms such as foraminifera and diatoms whose presence or lack thereof can indicate the condition of the sea ice cover above the sediment site. For example, certain planktonic diatoms live in or on sea ice

[*Cronin et al.*, 1995] whereas certain foraminifera thrive in open water conditions [*Cronin et al.*, 2008]. The presence of benthic species that rely on high fluxes of fresh organic matter can be used to indicate the location of the sea ice margin [*Polyak et al.*, 2002]. The chemical composition of the organic matter in sediment cores can also be used to investigate the presence of sea ice cover. Oxygen isotopes fractionate during sea ice formation and the depletion of $\delta^{18}O$ in planktonic foraminifera indicates enhanced brine production and sea ice formation [*de Vernal et al.*, 2008]. More recently the biomarker IP_{25} – an organic geochemical lipid present in sea ice diatoms in the spring – has been used to investigate seasonal sea ice cover [*Belt and Mueller*, 2013; *Belt et al.*, 2007]. The sediment cores that are found in the deep, central Arctic Ocean provide insight into sea ice extent spanning back millions of years, because the seafloor sediment in the region was not disturbed by periods of low sea level or the traverse of large glaciers. However, the slow rate of sediment deposition in the central Arctic means that these cores provide quite a coarse temporal resolution, of up to a millennium. Coastal cores often only date back to the Last Glacial Maximum (LGM) and corresponding low sea-level stand, but are able to capture variability on century and decadal timescales due to faster rates of deposition [*Polyak et al.*, 2010].

Other proxy records include Arctic coastal deposits and terrestrial records from the Arctic region. In coastal regions the presence of land-fast ice can be inferred from the distribution of driftwood logs, which can in turn be inferred from radiocarbon dating. This driftwood is transported long distances by sea ice, and found on ice-free coasts near sea-ice margins [*Blake Jr*, 1975; *Eggertsson*, 1993; *Haggblom*, 1982]. Mammal bone deposits have also been used to investigate past sea ice conditions because the seasonal migrations of certain mammals, such as the walrus [*Dyke et al.*, 1999] and bowhead whale [*Dyke et al.*, 1996; *Savelle et al.*, 2000], are dictated by variations in sea ice cover. The terrestrial proxies that can provide information regarding the past climate of the Arctic, and therefore likely sea ice regimes, include plant remains, ice cores, lake sediment cores, and tree rings [*Kinnard et al.*, 2011].

On more recent time-scales than those examined using proxy records, but prior to the beginning of the satellite era in 1972, [*Parkinson and Cavalieri*, 1989], historical records can be used to provide insight into the extent of Arctic sea ice. Most historical data are from ships at sea. The U.S. NCAR have produced a record of Arctic sea ice concentration spanning from 1870 to 2011 [*Chapman and NCAR*, 2013] by compiling ship-based observations from the pre-satellite years. For the first half of the 20th century the primary data source came from Danish Meteorological Institute (DMI) ship reports and Norwegian Polar Institute (NPI) sea ice charts. The NPI sea ice charts also

span to the beginning of the satellite era and back to the pre-1900 period. A limitation of the NCAR dataset is that it relies on ship-based observations that are often carried out near the ice edge and assume 100% concentration north of this. Satellite observations have shown that this is not the case [*Walsh and Chapman*, 2001]. Other historical sea ice records can come from the observations of indigenous Arctic peoples. An impressive example of this is from Icelandic communities who have recorded the distribution of sea ice and icebergs along the Icelandic coastline since approximately 870AD. From these observations a sea ice index was derived by *Koch* [1945] and has been continuously revised [*Bergthorsson*, 1969; *Ogilvie*, 1984]. *Kelly et al*. [1987] correlated the sea ice index with the aforementioned NCAR ice concentration data for the Icelandic and adjacent seas and concluded that the index is a reasonable measure of the ice cover of a large area of the northern North Atlantic.

Satellite observations of Arctic sea ice extent began in 1972, by using passive microwave sensors to measure the ice concentration. Sea ice concentration measurements from satellite rely on the fact that passive microwave instruments sense emitted microwave radiation, which is affected by surface and atmospheric conditions. The contrast between sea ice and ocean emissivities is high, and increases with decreasing channel frequency. The brightness temperature of sea ice varies spatially due to variations in the surface topography and temperature of the ice, while the brightness temperature of open water remains relatively constant within the sea ice pack [*Cavalieri et al*., 1992; *Comiso et al*., 1997]. From 1972-1978 sea ice concentration estimates were generated using brightness temperature data derived from the Nimbus-5 Electrically Scanning Microwave Radiometer (ESMR) and the Nimbus-7 Scanning Multichannel Microwave Radiometer (SMMR), although the satellite data was not available for all months [*Parkinson and Cavalieri*, 1989]. Continuous satellite observations of Arctic sea ice extent began in October 1978 thanks to the availability of data from a suite of passive microwave satellites [*Stroeve et al*., 2012a]. The National Snow and Ice Data Center (NSIDC) in the USA provides sea ice concentrations generated from brightness temperature data derived from the SMMR carried on-board Nimbus-7 from 1978-1987, the SSM/I instruments on-board the DMSP-F8, -F11 and -F13 satellites from 1987-2007, and the Special Sensor Microwave Imager/Sounder (SSMIS) instrument on-board the DMSP-F17 satellite from 2008-2016. Since April 2016, the SSMIS on-board DMSP-F18 has been used, due to a fault with the vertically polarized 37 GHz channel of the DMSP-F17 SSMIS. Nimbus-7 was able to survey the Arctic up to a latitude of 80.77°N. All DMSP satellites used for measuring sea ice concentration provide data up to 81.20°N.

The two most common algorithms that have been used for deriving sea ice concentration from multichannel data are the Bootstrap algorithm and the NASA Team algorithm, both of which were developed at NASA's Goddard Space Flight Center (GSFC). The two algorithms use different channel combinations, reference brightness temperatures, weather filters, and techniques [*Comiso et al.*, 1997; *Swift and Cavalieri*, 1985]. Data have been produced using the Bootstrap algorithm at GSFC since 2005, and are available from NSIDC at monthly or daily temporal resolution, for 1978-2014 [*Comiso*, 2000, updated 2015]. Data have been produced using the NASA Team algorithm at GSFC since 1996 and are available from NSIDC at monthly or daily temporal resolution with a lag of about a year [*Cavalieri et al.*, 1996, updated yearly]. NSIDC also use the NASA Team algorithm to produce their own NRT estimates of daily and monthly sea ice concentration with a lag of about 48 hours [*Maslanik and Stroeve*, 1999, updated daily]. Both datasets produced using the NASA Team algorithm are continuously updated and are available from October 1978.

Since 1996, the NASA Team algorithm has undergone a number of changes to account for the problems encountered when estimating sea ice concentration using multiple sensors with different frequencies, footprint sizes, and calibrations. One key obstacle to resolving these differences is the lack of temporally overlapping data from the different satellites. A number of techniques are employed to address inter-satellite differences and these include mapping the sensor data onto a common grid, applying a common land mask, addressing instrument drift, and inter-sensor corrections [*Cavalieri et al.*, 1999]. Another consideration is that the inclinations of each satellite mean that they are not able to observe a small area centered on the North Pole. The size of this area varies between the satellites but in all cases has an irregular edge due to the coverage of the instrument swath near the North Pole. The data developers apply a circular mask that symmetrically covers the observed maximum extent of the data to provide the smallest, most consistent missing area possible. The Nimbus-7 SMMR mask was applied from November 1978 to June 1987 and provided data coverage to 84.50°N. the DMSP –F8, -F11 and F-13 SSM/I mask was applied from July 1987 to December 2007 and provided data coverage to 87.20°N. Finally, the DMSP-F17 SSMIS masks has been applied since January 2008 to present and provides data coverage as far north as 89.18°N [*NSIDC*, 2015]. Uncertainties in sea ice concentration are difficult to quantify because the ice cover is always evolving and experiences seasonal and non-seasonal variations in its physical properties and emissivity. The measurement accuracy is better over areas of consolidated ice with thicknesses of >20 cm and high concentration, and decreases with an increasing proportion of thinner ice [*Cavalieri et al.*, 1992; *Comiso and Kwok*, 1996; *Comiso et al.*,

1997]. NSIDC quote a figure of 5% for the uncertainty in their NASA Team NRT Arctic sea ice concentration values in winter, and 15% in summer when meltponds develop on the ice (http://nsidc.org/data/docs/daac/nsidc0051_gsfc_seaice.gd.html).

1.6.2. Arctic sea ice thickness

Early investigations into the thickness of Arctic sea ice relied on measurements of under-ice thickness, known as sea ice draft, from ULS instruments. The USS *Nautilus* submarine was the first vessel to cross the Arctic Basin via the North Pole in August 1958, and made an almost continuous ULS draft profile. In August 1970 the USS *Queenfish* submarine repeated the route, by which time mean sea ice draft had reduced by 0.2 m in the transpolar drift stream and Eurasian Basin, and 0.7 m in the Canadian Basin [*McLaren*, 1989]. *McLaren et al*. [1992] were able to investigate the inter-annual variability in sea ice draft, using data from 50 and 100 km-long segments of submarine ULS measurements from 12 voyages centered over the North Pole conducted between 1958 and 1992. Over this 34-year period the overall mean draft was 3.6 m but demonstrated a large inter-annual variability, ranging from 2.8 m in 1986 to 4.4 m in 1970, sufficiently large to obscure any discernable thinning of the Arctic sea ice cover over that period. There was however a significant decrease in mean sea ice draft between October 1976 and May 1987 over a zone extending more than 400 km to the north of Greenland, as measured by two British submarine cruises [*Wadhams*, 1990]. Throughout the 1990s, summer ice draft data were acquired across the Arctic Ocean as part of the Scientific Ice Expeditions (SCICEX), which used U.S. Navy submarines for scientific research [*Gossett*, 1996; *Rothrock et al*., 2003] (Figure 1.7). Since 2003, the Beaufort Gyre Exploration Program (BGEP), based at WHOI, have made year-round sea ice draft data available from three moored ULS buoys in the Beaufort Sea (http://www.whoi.edu/beaufortgyre). Although past observations provide insight into the changing state of the Arctic sea ice pack, they have been spatially incomplete and temporally sporadic, making it difficult to reliably estimate trends in Arctic-wide sea ice thickness and volume.

When satellite observations of the Arctic began in 1972 the instruments used were not capable of measuring sea ice thickness. Indeed, as recently as 1986 remote sensing experts questioned whether satellite measurements of sea ice thickness would ever be possible. At that time a report was compiled to identify the limitations of remote sensing of the oceans and troposphere and stated that “there is the difficulty or impossibility of remotely sensing several of the ice parameters identified, e.g., ice thickness, albedo, ocean parameters beneath the ice, and location of small icebergs [*Atlas et al*., 1986].” However, the launch of the European Space Agency’s (ESA) European Remote Sensing

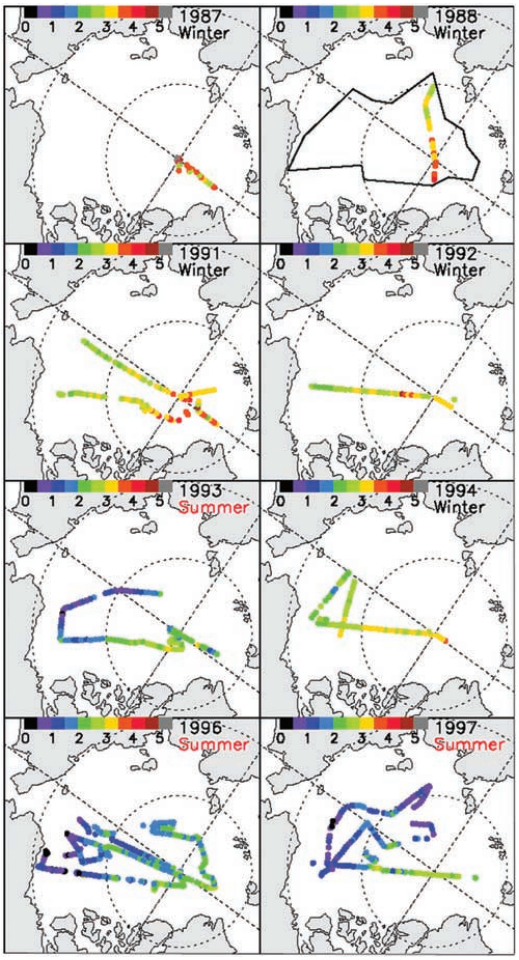

Figure 1.7: The observed ice draft (m) along eight submarine cruise tracks from 1987 to 1997. The sea ice draft data were collected as part of the Scientific Ice Expeditions (SCICEX), which used U.S Navy submarines for scientific research. From *Rothrock et al.* [2003].

(ERS) satellites, ERS-1 (1991-2000) and ERS–2 (1995-2011) marked the start of a new era of Arctic sea ice observation, in which satellite remote sensing could be used to estimate Arctic sea ice thickness using radar altimeter data. The ERS satellites were equipped with a 13.8 GHz radar altimeter instrument and had a region of coverage (ROC) extending to 81.5°N, meaning that they could survey more than half of the permanent sea ice cover of the Arctic in any given month. *Peacock and Laxon* [2004] made significant progress towards satellite measurements of sea ice thickness when they used ERS-1 and -2 radar altimeter data to produce the first measurements of sea surface height in sea ice-covered regions. Following this *Laxon et al.* [2003] used ERS-1 and -2 data to provide the first estimates of sea ice thickness from satellite radar altimetry. The analysis of individual radar echoes can be used to distinguish those originating from consolidated first and multi-year ice floes from those due to

leads, open water and new ice. It is then possible to estimate the elevation of the sea ice surface above the ocean, known as the ice freeboard, and to convert this to ice thickness by assuming that ice floes are in hydrostatic equilibrium and the dominant radar return is from the snow/ice interface. ERS data revealed a high-frequency inter-annual variability in mean winter (defined as October-March) sea ice thickness from 65.0°N to 81.5°N, between 1993-2001. The data also provided insight into the driving forces behind the variability. Changes in sea ice thickness between consecutive winters correlated well with the intervening melt season length [*Smith*, 1998], suggesting that from 1993-2001 the variability of mean ice thickness was dominated by changes in thermodynamic forcing. The thickest ice was observed adjacent to the Canadian Archipelago and in the Fram Strait. Following the ERS missions, the ESA Envisat satellite was launched in 2002, to provide for continuity of the observations started with the ERS satellites. The inclination was the same as the ERS satellites and the mission ended in 2012. Envisat data was used to show that after 2007, which was the year of the record minimum ice extent at the time, the average winter ice thickness was reduced compared to the average of the previous 5 years, particularly in the Western Arctic [*Giles et al.*, 2008a].

From 2003-2010 the NASA Ice, Cloud, and land Elevation Satellite (ICESat) mission overlapped in time with Envisat. ICESat had a ROC extending to 86°N and was equipped with a laser altimeter instrument that could be used to measure the elevation of the sea ice plus snow surface above the ocean, by assuming that the dominant return signal was from the snow surface. Therefore sea ice thickness could be estimated using the same theory as with radar altimetry, with an adjusted scattering horizon. However, the laser operation was hampered by the presence of clouds and as such the temporal coverage of ICESat data over Arctic sea ice is not continuous. Data is consistently available for October, November, and March, and either February or April of each year [*Kwok et al.*, 2007]. *Kwok et al.* [2009] used ICESat data to show a 19% decrease in winter (February/March or March/April) sea ice thickness from 2005-2008, dropping from a mean thickness of 3.2 to 2.6 m. In contrast, the mean winter thickness of the seasonal ice exhibited a negligible trend and remained close to 2 m. ICESat observed the thickest Arctic sea ice in the regions north of the Canadian Archipelago and Greenland. These findings were based on observations that were limited to a fixed central Arctic region that covers an area of ~7.2×10^6 km^2. The region is defined as the area bounded by the gateways into the Pacific (Bering Strait), the Canadian Archipelago and the Greenland (Fram Strait) and Barents seas and as such excludes lower latitude sea ice cover [*Kwok et al.*, 2009]. The region will hereafter be referred to as the ICESat domain (Figure 1.8). A follow on

mission, ICESat-2, is due for launch in late-2017 (http://icesat.gsfc.nasa.gov/icesat2/index.php).

The ESA CryoSat-2 satellite was launched in April 2010 and now provides unparalleled coverage of the Arctic Ocean, with a ROC extending to 88°N. The on-board radar altimeter operates at 13.6 GHz and uses Synthetic Aperture Radar (SAR) technologyto provide improved across- and along-track resolution compared to previous ESA missions [*Wingham et al.*, 2006]. A study by *Laxon et al.* [2013] produced the first estimates of Arctic sea ice thickness from CryoSat-2. They limited their observations to the ICESat domain and showed that the spatial distribution of the ice thickness data in autumn (October/November) and winter (February/March) was similar to that observed by the ICESat satellite [*Kwok et al.*, 2009; *Laxon et al.*, 2003] and the PIOMAS model [*Zhang and Rothrock*, 2003], with the thickest ice adjacent to the Canadian Archipelago and north of Greenland. Since then others have developed their own CryoSat-2 sea ice processing systems, including *Kurtz et al.* [2014] at NASA, *Kwok and Cunningham* [2015] at NASA, and *Ricker et al.* [2014] at the Alfred Wegener Institute (AWI). These data all differ slightly in their areal coverage (Figure 1.8). Both

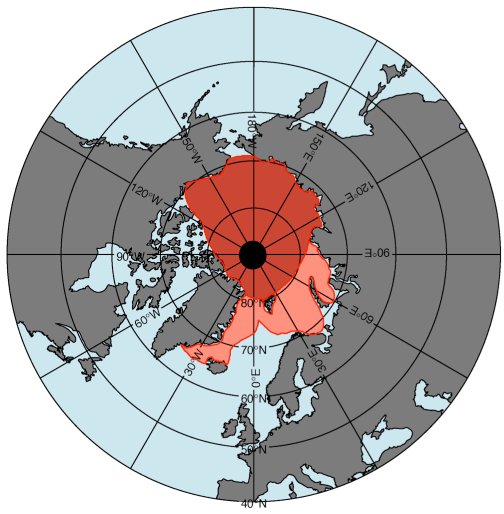

Figure 1.8: Masks used for processing CryoSat-2 data over Arctic sea ice. The dark red mask covers the ICESat domain, used by *Kurtz et al.* [2014] and *Kwok and Cunningham* [2015] at the National Aeronautics and Space Administration (NASA). The region was initially defined for use with the NASA ICESat satellite [*Kwok et al.*, 2009]. The dark red and light red mask combined show the mask applied by *Ricker et al.* [2014] at the Alfred Wegener Institute (AWI). *Tilling et al.* [2015] analysed all sea ice north of 40°N, to produce the first estimates of Arctic-wide sea ice thickness. CryoSat-2 data cannot be used to estimate Arctic sea ice thickness north of 88°N (small black circle) due to its orbital inclination.

NASA teams produce estimates within the ICESat domain whereas the AWI processor covers the area of the Arctic Ocean where values of snow depth from a climatology [*Warren et al.*, 1999] are considered realistic. CryoSat-2 data was also used to produce the first estimates of Arctic-wide sea ice thickness [*Tilling et al.*, 2015]. These estimates not only covered the Arctic, but all Northern Hemisphere sea ice above and including 40°N. The production and analysis of these thickness estimates are ongoing and will be discussed in detail in this thesis.

It is possible that sea ice thickness measurements from CryoSat-2 and other radar altimeter satellites become less reliable below ~0.5 m thickness. This is due to the difficulty in discriminating regions of thin ice from open water [*Laxon et al.*, 2003]. One suggested solution is the use of data from the ESA Soil Moisture and Ocean Salinity (SMOS) satellite, which was launched in November 2009, to obtain estimates of Arctic sea ice thickness over thin ice regions. The Microwave Imaging Radiometer using Aperture Synthesis (MIRAS) on-board SMOS operates in the L-band at a frequency of 1.4 GHz. *Kaleschke et al.* [2012] derive sea ice thickness from MIRAS microwave brightness temperature by using a single layer emissivity model and assuming that the ice emissivity is mainly a function of its temperature, salinity and thickness. The sea ice temperature and salinity are taken from a reanalysis data/thermodynamic model combination and a climatology, respectively. *Kaleschke et al.* [2012] found that thin sea ice thicknesses derived from SMOS agreed with the temporal development of ice growth

from an ice thickness model. They concluded that SMOS can be used to retrieve sea ice thickness up to 0.5 m, at least under cold conditions (surface air temperatures below 10°C) over a high concentration sea ice cover. Despite a number of satellite validation campaigns such as the CryoSat Validation Experiments (CryoVEx) [*Beckers et al.*, 2015] and dedicated sea ice measurement campaigns such as the Sever expedition [*Romanov*, 2004] and numerous research cruises, *in situ* measurements of Arctic sea ice thickness are still limited in their spatial and temporal coverage, especially in the Arctic summer. This is also true of measurements of sea ice density and the depth and density of the snow cover on Arctic sea ice.

1.6.3. Arctic sea ice volume

The first estimates of Arctic sea ice volume were produced by *Kwok et al.* [2009], by combining ICESat thickness estimates with sea ice concentration data from AMSR-E. They found that over the 2005-2008 period the winter (February/March or March/April) volume of MYI decreased by 40%, which corresponds to a net volume loss of 6,300 km^3. Over the same period the FYI cover gained volume owing to an increase in

extent, but the overall volume of sea ice exhibited a loss. Following these observations, *Laxon et al*. [2013] produced the first estimates of CryoSat-2 Arctic sea ice volume, which they limited to the ICESat domain. By combining ICESat and CryoSat-2 results, the study showed that between 2003-2012, autumn (October/November) declined by 4291 km^3 and the winter (February/March or March/April) volume by 1479km^3. The average volume loss over both the autumn and winter periods was approximately 500 km^3 $year^{-1}$, equivalent to a 0.075 m $year^{-1}$ decrease in thickness, which is close to the peak thinning rates observed in the submarine record [*Kwok and Rothrock*, 2009]. The first estimates of ice volume for the entire Northern Hemisphere coincided with those of Northern Hemisphere sea ice thickness produced by *Tilling et al*. [2015] (Section 1.6.2). It is these estimates of sea ice thickness and volume, and the environmental factors that drive their variability that will form the basis of this thesis.

1.7. Antarctic sea ice

1.7.1. Antarctic sea ice extent

In contrast to the widely reported decline in Arctic sea ice extent over the satellite era, Antarctic sea ice extent has, on average, increased since consistent satellite observations began in 1978. Antarctic sea ice typically reaches its minimum extent in February and maximum in September. Antarctic sea ice extent exhibits a large seasonal cycle – over the period 1979-2010 the average minimum extent was 3.1×10^6 km^2 and the average maximum extent was 18.5×10^6 km^2 [*Parkinson and Cavalieri*, 2012]. When the seasonal cycle was removed, the upward trend in Antarctic sea ice volume from 1979-2010 was 13,700 ± 1,500 km^2 $year^{-1}$ when all months were considered. This increase has not been spatially uniform, with the majority of the increase occurring in the Ross Sea, with contributions from the Weddell Sea and the Indian Ocean. The region encompassing the Bellingshausen Sea and Amundsen Sea has instead experienced a significant decrease in sea ice extent.

There is no clear consensus regarding the mechanism through which Antarctic sea ice extent is increasing, although a number of studies have aimed to address it. One possible factor is the drop in ozone levels over Antarctica. The “ozone hole” over the central Antarctic has cooled the stratosphere, causing a strengthening of Antarctic cyclonic winds that drive increased upwelling of cooler subsurface water and create areas of open water, both of which encourage sea ice growth [*Ferreira et al.*, 2015; *Purich et al.*, 2016]. Others have suggested that warmer Antarctic air temperatures have caused increased rain and snowfall and a freshening of the surface waters, leading to increased stratification. The increased stratification means that less heat is

transported upwards from the deeper, warmer ocean and less sea ice melted [*Zhang*, 2007]. Melting land ice could also be responsible, as it leads to more fresh, almost-freezing water reaching the surface waters of the Antarctic and encouraging sea ice growth [*Bintanja et al.*, 2015; *Pauling et al.*, 2016]. These factors are not necessarily independent of one another.

1.7.2. Antarctic sea ice thickness and volume

Past observations of Antarctic sea ice thickness are far sparser in space and time than for the Arctic, making it even more difficult to reliably estimate trends in Antarctic-wide sea ice thickness and volume. Some *in situ* measurements of sea ice thickness are available from drilling profiles (~100–200 drill holes per floe) collected over 273 floes during research cruises from 1988-2007 [*Ozsoy-Cicek et al.*, 2013]. Sea ice draft measurements from 13 drifting ULS instruments are available for 1990–2008, but are restricted to the Weddell Sea [*Behrendt et al.*, 2013]. The most extensive estimates of Antarctic sea ice thickness come from observations collected from 1981-2005 on 81 Antarctic cruises and compiled as part of the Scientific Committee on Antarctic Research (SCAR) Antarctic Sea Ice Processes and Climate (ASPeCt) program. The mean and standard deviation of sea ice thickness from these observations is reported as 0.87 ± 0.91 m [*Worby et al.*, 2008]. However, these observations are arguably subject to significant bias as they were collected from visual estimates only, whilst the ships were in transit. A recent paper by *Williams et al.* [2009] utilised autonomous underwater vehicle (AUV) technology to produce ten floe-scale maps of sea ice draft in spring during the IceBell and Sea Ice Physics and Ecosystem eXperiment 2012 (SIPEX-2) research cruises. These profiles cover an area of over 500,000 m^2 and were collected in the Bellingshausen Sea, Weddell Sea, and in the pack ice off Wilkes Land, East Antarctica. The latter was a region of heavily deformed sea ice and a significant fraction of the ice was thicker than 5 m. One floe in the region contained ice that reached a draft of 16.2 m – the greatest measured in the dataset.

The estimation of Antarctic sea ice thickness and volume from radar altimeter satellites such as ERS-1 and -2, Envisat, and CryoSat-2 is hampered by the complex snow and ice regimes of the region. For example, the snow cover on Antarctic sea ice is thicker than in the Arctic, meaning that the ice is often depressed below the sea surface and negative sea ice freeboards are common. The ice then becomes flooded and seawater "wicks" upward into the snow and refreezes. In addition the snow cover on Antarctic sea ice often survives the summer and begins to accumulate, which further complicates its composition [*Massom et al.*, 2001]. The snow cover exhibits distinct

layers that can include depth hoar, icy layers, and saline slush [*Maksym and Jeffries*, 2000; *Massom and Lubin*, 2006; *Massom et al.*, 1998]. Therefore the assumption applied over Arctic sea ice – that radar pulses penetrate through any snow cover on ice floes and scatter from the snow–ice interface (Section 1.6.2) – does not hold over the Antarctic. Due to these uncertainties radar altimeter data (from ERS-2) have so far only been used to estimate sea ice elevation (the elevation of the radar's reflecting surface above the sea level) in the Antarctic [*Giles et al.*, 2008b]. The ERS sea ice elevation estimates displayed similar spatial patterns to sea ice thickness from the ASPeCt dataset, which shows promise for producing Antarctic sea ice thickness estimates from radar altimetry missions. For the development of radar remote sensing techniques over Antartic sea ice, further studies of the radar penetration into the Antarctic snow cover are required [*Willatt et al.*, 2010].

Satellite laser altimeter instruments are not as complicated over Antarctic sea ice, as it is assumed that the dominant return signal is from the snow surface. *Kurtz and Markus* [2012] used ICESat data to produce basin-wide estimates of Antarctic sea ice thickness and volume from 2003–2008, by assuming that over the scale of an Antarctic sea ice floe the ice freeboard is zero and ICESat freeboard measurements are therefore equivalent to snow depth. Over this time period only small ice thickness changes occurred, of –0.03 m $year^{-1}$ on average for the spring and summer. Volume changes of –266 km^3 $year^{-1}$ and 160 km^3 $year^{-1}$ occurred for the spring (October/November) and summer (February/March), respectively. The study by *Kurtz and Markus* [2012] highlights the contrast in the rates of change in sea ice thickness and volume between hemispheres, as much greater percentage losses have occurred across the Arctic over the same time period.

1.8. Thesis aims

The primary aims of this research have been to advance the development of the CPOM UCL Arctic sea ice processor, and to utilise the output data to investigate the factors that drive interannual variability in sea ice thickness and volume across the Northern Hemisphere. In addition, the processor has been used to output sea ice thickness and volume in NRT. Therefore a final aim of this project was to assess the utility of the NRT data product, by investigating its spatial and temporal distribution. Each chapter is summarised below.

- **Chapter 2** introduces satellite radar altimetry and the CryoSat-2 satellite. The chapter describes the basic principle of satellite radar altimetry and the differences between beam-limited, pulse-limited, and SAR altimetry. The

introduction to the ESA CryoSat-2 mission, which includes information on its mission objectives, the different operating modes of CryoSat-2, and its measurement principle.

- **Chapter 3** provides an end-to-end, comprehensive description of the data processing steps employed at CPOM UCL to estimate Arctic sea ice thickness and volume from CryoSat-2 data. The chapter includes information regarding the additions made during this project, which are the extension of data provision to the whole of the Northern Hemisphere, and the development of an error budget for sea ice thickness and volume estimates.

- **Chapter 4** acts as the main results chapter for this thesis. CryoSat-2 thickness and volume results are presented alongside an evaluation of the results by comparison with a combination of airborne and buoy data, and model estimates. The chapter concludes by highlighting the inter-annual variations in sea ice volume detail.

- **Chapter 5** examines the potential drivers of inter-annual variability in Arctic sea ice volume. The chapter describes a technique to obtain information on climate forcing from reanalysis data, and assesses the impacts of climate forcing on sea ice thickness and volume. The work presented in this chapter was the subject of a Nature Geoscience paper published by *Tilling et al*. [2015] titled “Increased Arctic sea ice volume after anomalously low melting in 2013”.

- **Chapter 6** is dedicated to NRT estimates of Arctic sea ice thickness and volume. It introduces the fast delivery CryoSat-2 data that have been made available by ESA since April 2015, and the method applied to compute sea ice thickness and volume in NRT. As part of the method, the additional considerations required for the uncertainty budget are described. The NRT data are then analysed for one sea ice growth season, which includes a direct comparison with the archive product that is computed using final release CryoSat-2 data, and an analysis of the spatial and temporal coverage of the NRT data. The work presented in this chapter was the subject of a paper published by *Tilling et al*. [2016] in The Cryosphere, titled “Near-real-time Arctic sea ice thickness and volume from CryoSat-2”.

- **Chapter 7** is a summary chapter. It summarises the work presented in this thesis and discusses the future work that could develop from this research project.

2. Introduction to satellite radar altimetry and the CryoSat-2 satellite

2.1. Introduction

Satellite radar altimetry is a technique in which vertical incidence satellite-borne instruments are used to measure the elevation of the Earth's surface using a radar signal. When applied in the Polar Regions it can be used to measure the freeboard of sea ice [*Laxon*, 1994; *Rapley et al.*, 1983], and the elevation of land ice [*Femenias et al.*, 1993a] and the oceans [*Wunsch and Stammer*, 1998]. Applications of the data include the estimation of sea ice thickness and volume [*Laxon et al.*, 2013], ice-sheet mass balance [*Shepherd et al.*, 2012], and ocean circulation [*Giles et al.*, 2012]. This chapter describes the basic principle of satellite radar altimetry, and its different modes of operation – beam-limited, pulse-limited, and SAR. It then introduces the ESA CryoSat-2 mission. CryoSat-2 is a radar altimeter that is based on established altimetry techniques, but with improvements in its operation that enable precise measurements of the Polar Regions.

2.2. The principle of satellite radar altimetry

Satellite radar altimeters transmit pulses of radio waves or microwaves vertically downwards to the Earth's surface [*Chelton et al.*, 2001]. The time delay of the return signal from a surface can be analysed to estimate the elevation of that surface above a reference ellipsoid (a mathematical approximation of the Earth's shape), and hence the Earth's centre of mass. The elevation of the surface is calculated by differencing the satellite's altitude with respect to the chosen ellipsoid, and the satellite-to-surface distance, or the range (Figure 2.1).

The surface elevation calculation is written as:

$$E = A - R \tag{2.1}$$

where E is the elevation of the surface above a reference ellipsoid, A is the altitude of the satellite above the same reference ellipsoid, and R is the satellite range to the surface. The range, R, is the product of the speed of light, c, and the two-way travel time (or delay time) of the radar signal, t, divided by two:

$$R = \frac{ct}{2} \tag{2.2}$$

The precision of the range, and therefore surface elevation estimates is determined by the range resolution of the altimeter. This is given by:

$$\Delta R = \frac{c\tau}{2} = \frac{c}{2B} \tag{2.3}$$

where ΔR is the range resolution, τ is the compressed pulse length, and B is the instrument bandwidth. The instrument bandwidth is the difference between the upper and lower cut-off frequencies of its receiver [*Raney*, 1999]. The accuracy of the measurement is determined by knowledge of c and any timing biases in the instrument. Variations in c occur in the ionized upper atmosphere, where electron density must be estimated, and due to water vapour and dry gas in the troposphere [*Curran*, 1985].

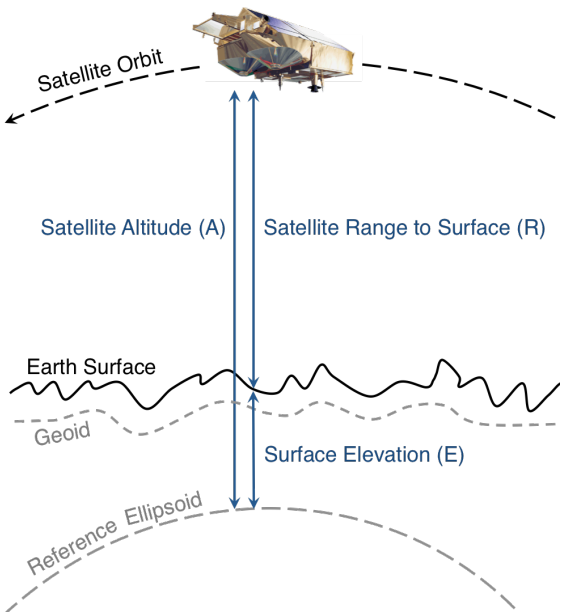

Figure 2.1: The basic principle of satellite radar altimetry. The altimeter measures the range, R, between the satellite and the Earth's surface. The range is subtracted from the satellite altitude, A, to estimate the surface elevation, E, above a reference ellipsoid.

2.3. Radar altimeter operation

In theory there are two basic modes of operation for radar altimeters. These modes are known as beam-limited and pulse-limited. In both cases the effective pulse duration is short, on the order of nanoseconds, to achieve a sufficient range resolution. The mode

of operation dictates the footprint size – defined as the effective area that the radar signal illuminates on the Earth's surface. The principles of beam-limited and pulse-limited operation are described in Sections 2.3.1 and 2.3.2, respectively. Instrument resolution can be improved with respect to standard radar techniques using SAR technology [*Curlander and McDonough*, 1991], which is introduced in Section 2.3.3. CryoSat-2 is the first terrestrial satellite to operate in SAR altimeter mode.

2.3.1. Beam-limited altimetry

The basic concept of a radar altimeter can be understood by beam-limited altimetry. In this mode, the return pulse characteristics and beam-limited footprint are dictated by the antenna beam width, or the half-power beam width (HPBW). The HPBW is the angular separation between adjacent points on the main beam where the magnitude of the radiation pattern is 50% below the maximum of the main lobe (3 dB below in decibels). The beam-limited footprint is made sufficiently small that the differential path length at the edge of the beam (ΔR) is less than the product of the speed of light, c, and the effective pulse length, τ (Figure 2.2).

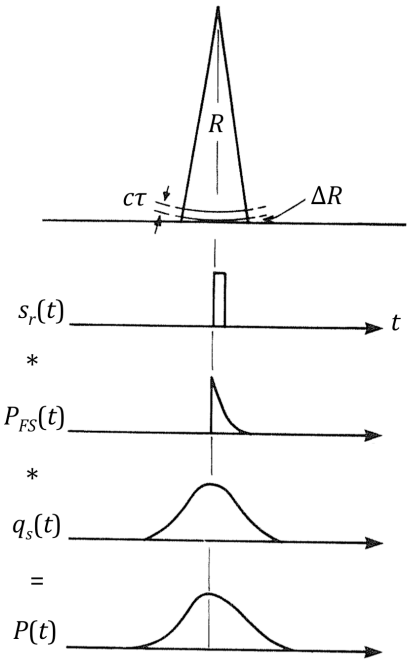

Figure 2.2: Beam-limited echo power, $\boldsymbol{P(t)}$, as a function of delay time over a flat, homogenously rough, horizontal surface. $\boldsymbol{P(t)}$ is the convolution of the transmitted pulse shape, $\boldsymbol{s_r(t)}$, flat surface impulse response, $\boldsymbol{P_{FS}(t)}$, and the height probability density function of specular reflecting facets, $\boldsymbol{q_s(t)}$. Adapted from *Rapley et al.* [1983].

Over a flat, homogenously rough, horizontal surface viewed normally, the echo power as a function of delay time, $P(t)$, can be represented as a convolution between the transmitted pulse shape, $s_r(t)$, flat surface impulse response (FSIR), $P_{FS}(t)$, and the height probability density function (PDF) of specular reflecting facets, $q_s(t)$:

$$P(t) = s_r(t) * P_{FS}(t) * q_s(t) \tag{2.4}$$

The FSIR describes the average echo power as a function of delay time from an illuminated flat surface, weighted by the antenna gain pattern (the angular dependence of the strength of the signal from the antenna) and the angular dependence of the backscatter [*Brown*, 1977; *Rapley et al.*, 1987]. For beam-limited altimetry, the effect of the narrow beam and sharp cut-off of surface illumination on the FSIR result in a return power profile that is a convolution of $s_r(t)$ and $q_s(t)$ only. The return waveform shape corresponds to the PDF of the specular scatterers (Figure 2.2), and the range to the surface can be estimated from the centre of the waveform.

The application of beam-limited altimetry to satellite-based platforms is inhibited by antenna size requirements. The HPBW, ϑ, is related to the wavelength of the transmitted signal, λ, and the dimension of the antenna, d, by:

$$\vartheta = k\frac{\lambda}{d} \tag{2.5}$$

where k is a factor that depends on the shape of the antenna, and is ~1.22 for a parabolic antenna [*Ulaby et al.*, 1986]. Equation (2.5) shows that narrow beams require large antennae, which is impractical and expensive for satellite applications. The operation of satellite radar altimeters in beam-limited mode has also been ruled out in the past on the basis of the demanding requirements placed on precise antenna pointing of narrow beams [*Rapley et al.*, 1983].

2.3.2. Pulse-limited altimetry

Due to the impracticality of beam-limited altimetry for satellite applications, satellite radar altimeters adopt a pulse-limited mode of operation, which uses as smaller antenna with a broader beam width, and has a more relaxed requirement on antenna

pointing. In pulse-limited altimetry the return pulse and pulse-limited footprint are dictated by the effective length of the pulse. In this mode the pulse energy propagates from the antenna as part of an expanding spherical shell. The surface area illuminated by a given radar pulse is a disk shape that expands linearly with time until the trailing edge of the pulse leaves the lowest reflecting points at nadir. The illuminated area then grows as an annulus with constant area (Figure 2.3) [*Rapley et al.*, 1987]. Pulse-limited radar altimeters use pulse compression to achieve the equivalent of a short, intense pulse. A relatively long pulse, on the order of microseconds, is transmitted and the return pulse is processed in a way equivalent to measuring the return time to the surface of a much shorter pulse, on the order of nanoseconds. This enables the radar to achieve adequate range resolution with lower peak power requirement [*Fetterer et al.*, 1992].

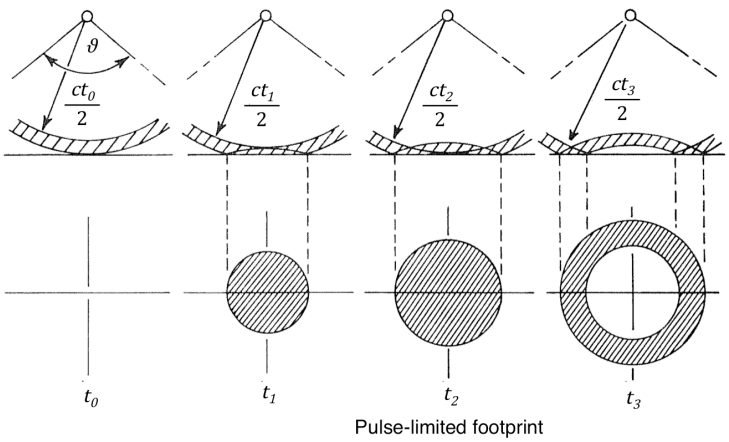

Figure 2.3: Development of the illuminated surface area for a pulse-limited altimeter. Adapted from *Rapley et al.* [1983].

The pulse-limited footprint is defined as the surface area illuminated as the trailing edge of the pulse leaves the lowest reflecting points at nadir. It corresponds to the part of the waveform over which maximum power is reached [*Fetterer et al.*, 1992]. Mathematically, it is defined as:

$$r = \sqrt{Rc\tau} = \sqrt{R\frac{c}{B}} \tag{2.6}$$

where r is the radius of the pulse-limited footprint, R is the satellite range to the surface, c is the speed of light, τ is the compressed pulse length, and B is the instrument bandwidth [*Chelton et al.*, 2001]. As the illuminated area continues to grow as an annulus, the pulse-limited footprint is smaller than the full antenna illumination pattern, or antenna-limited footprint. In pulse-limited altimetry the beam width is broad enough that differential path length at the edge of the full antenna-limited footprint (ΔR) is much greater than the product of *c* and τ (Figure 2.4).

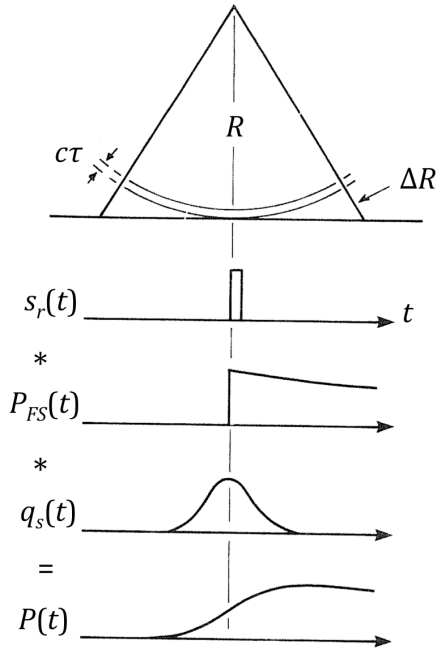

Figure 2.4: Pulse-limited echo power, $P(t)$, as a function of delay time over a flat, homogenously rough, horizontal surface. $P(t)$ is the convolution of the transmitted pulse shape, $\boldsymbol{s_r(t)}$, flat surface impulse response, $\boldsymbol{P_{FS}(t)}$, and the height probability density function of specular reflecting facets, $\boldsymbol{q_s(t)}$. Adapted from *Rapley et al.* [1983].

Over a flat, homogenously rough, horizontal surface viewed normally, the echo power as a function of delay time is described by Equation (2.4). The leading edge of the return power waveform displays a rise in power with time as the radar pulse illuminates an increasing area on the surface, and the rise in power is proportional to the illuminated area [*Fu and Cazenave*, 2000]. The power of the return waveform then gradually decreases, as the radar pulse expands over the surface to form the annulus and a smaller surface area is illuminated. The return waveform shape corresponds to the integral of the heights of the specular scatterers (Figure 2.4), and the range to the surface can be estimated from the half power point of the waveform leading edge. Over a flat, specular surface viewed normally, the echo power rises and falls again very

rapidly, creating an echo that looks like a spike. This is because the backscatter of the surface is large, and highly directional, meaning that most of the power is reflected away from the receive antenna (at an angle equal to the angle of incidence). The effective illuminated area that contributes to the integral of the heights of the specular scatterers is reduced compared to the rough surface case. This influences the FSIR such that the return waveform is a copy of the transmit pulse [*Laxon and Rapley*, 1987; *Rapley et al.*, 1985].

2.3.3. Synthetic aperture radar (SAR) altimetry

As described in Section 2.3.1, the large antennae required for high horizontal resolution radar observations are impractical for satellite applications. Instead, building on imaging radar techniques, a new innovation in altimetry is employed by CryoSat-2, in which the forward motion of the satellite is used to synthesise a larger aperture antenna [*Curlander and McDonough*, 1991; *McCandles Jr and Jackson*, 2004]. As it moves, the satellite transmits phase-coherent pulses that are received from many different points along its orbit. The satellite movement causes a Doppler shift of the received signal in the along-track direction, which is a function of the satellite's along-track position and velocity. SAR systems save the phase histories of the responses at each position then weight, phase shift, and coherently sum them to focus on one target area at a time and suppress all others. By focusing successive radar pulses on the same area of ground during motion, the returns from different angles at different times can be synthesised into a narrow equivalent main lobe to improve along-track resolution. Multiple pulses are summed for each resolution cell, resulting in an improved signal to noise ratio compared to regular radar altimeters.

During flight, the SAR system records the return signals from the target area from multiple pulses. The target area is within the radar footprint at various satellite positions. During this time the radar altimeter collects waveforms, phase information and Doppler measurements, which are processed to synthesise an aperture with length equivalent to the along-track distance travelled by the satellite antenna while the target location is illuminated.

2.4. The CryoSat-2 satellite mission

2.4.1. The CryoSat-2 satellite mission objectives

The primary aim of ESA's CryoSat-2 mission was to accurately determine the inter-annual fluctuations and longer-term trends in Earth's continental and marine ice fields

[*Drinkwater et al.*, 2004; *Wingham et al.*, 2006]. CryoSat-2 data have now been used to estimate the thickness and volume of Arctic sea ice [*Kwok and Cunningham*, 2015; *Laxon et al.*, 2013; *Tilling et al.*, 2015], and monitor elevation changes in Arctic [*Helm et al.*, 2014] and Antarctic [*McMillan et al.*, 2014] ice sheets.

CryoSat-2 has been able to meet its mission objectives due to its unique coverage of the Polar Regions compared with other satellite missions. The orbit inclination of CryoSat-2 is 92° meaning it can observe to just 2° short of the poles. In *Wingham et al.* [2006] the inclination is described as a 'compromise' between achieving a high density of orbit crossovers over Arctic land ice, whilst achieving almost complete coverage of the Arctic Ocean and the Antarctic continent. To further achieve this compromise the satellite has a 369-day repeat period (to provide the high orbit crossover density over high latitude land), which is built up by successive shifts of a 30-day sub-cycle (to provide uniform coverage of the Arctic sea ice and Antarctic continent every 30 days). Over the period that both CryoSat-2 and ESA's Envisat satellite were in orbit (October 2010-March 2012), CryoSat-2 mapped an average of 63% of the Arctic sea ice north of 60°N, compared to 21% for Envisat (Figure 2.5a). This is equivalent to a measurement being delivered, on average, within 6 km of each location in the Arctic every month for CryoSat, compared to every 31 km for Envisat (Figure 2.5b).

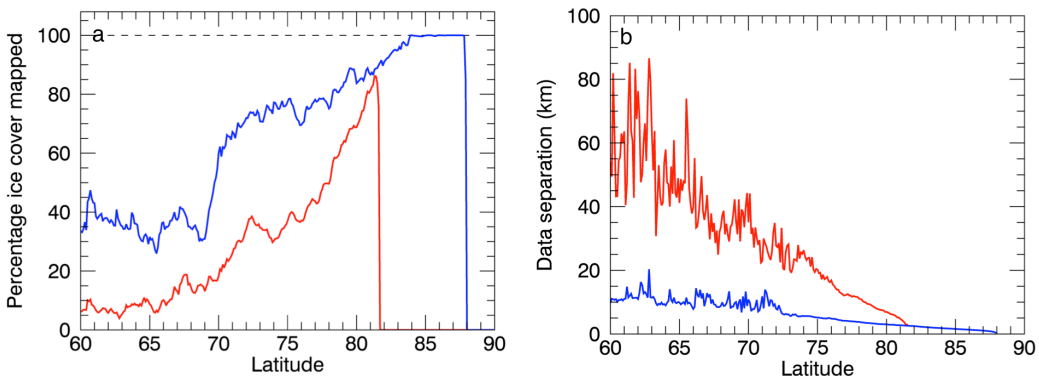

Figure 2.5: CryoSat-2 and Envisat data coverage, north of 60°N. (a) Percentage of sea ice cover mapped in 0.1° latitude bands, averaged over each month from October 2010-March 2012, for CryoSat-2 (blue) and Envisat (red). (b) Mean separation between measurement points in 0.1° latitude bands, averaged over each month from October 2010-March 2012, for CryoSat-2 (blue) and Envisat (red).

2.4.2. The CryoSat-2 SIRAL instrument

Cryosat-2's primary payload is the Synthetic Aperture Interferometric Radar Altimeter (SIRAL). SIRAL is an altimeter/interferometer system operating in the Ku-band (13.575 GHz). The SIRAL antenna system comprises two nadir looking antenna mounted 1 m apart in the across-track direction [*Wingham et al.*, 2006]. SIRAL operates in three modes (Figure 2.6) – low resolution mode (LRM), SAR mode, and SAR interferometric (SARIn) mode – depending on the type of surface that is being observed [*ESA/MSSL*, 2013]. CryoSat-2 operates in LRM over areas of the continental ice sheets, and the majority of the Earth's ice-free oceans and land. SAR mode is implemented over sea ice areas, which are relatively flat, as well as some ocean basins and coastal zones. SARIn mode is mainly implemented over ice sheet margins, small ice caps and mountain glaciers, which often have large slope variations. It is also used over some geostrophic ocean currents and major hydrological river basins. Prior to October 2014, SARIn mode was also used over a small area of sea ice north of Ellesmere Island, Nunavut (Figure 2.6).

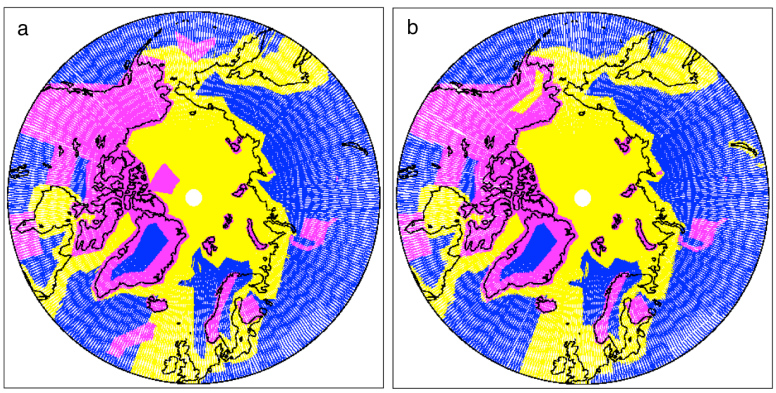

Figure 2.6: CryoSat-2 operation modes across the Arctic. CryoSat-2 operates in low resolution mode (LRM; blue tracks) over the continental ice sheets and the majority of the Earth's ice-free oceans and land, synthetic aperture radar (SAR) mode (yellow tracks) over sea ice and some ocean basins and coastal zones, and SAR interferometric (SARIn) mode (pink tracks) over ice sheet margins, small ice caps and mountain glaciers, and some geostrophic ocean currents and major hydrological river basins. (a) The mode mask for orbit tracks in April 2011, when the SARIn mode was in operation over a small area of sea ice north of Ellesmere Island. (b) The mode mask for orbit tracks in April 2015, once the SARIn mode was no longer in operation over sea ice. This is the mode mask that has been implemented since October 2014.

In LRM a single antenna is used to transmit and receive the signal and SIRAL acts as a conventional nadir-pointing, pulse-limited altimeter. The LRM footprint is

approximately 1.6 km, based on an altitude of 720 km. At the typical CryoSat-2 orbital speed of 7 km s^{-1}, the interval between pulses in LRM is about 500 μs (2000 Hz), which ensures that returning echoes are uncorrelated. This means that the data collection rate for LRM is lower than SAR and SARIn mode [*ESA/MSSL*, 2013; *Wingham et al.*, 2006], which are discussed in the following two Sections.

2.4.3. SAR mode

When operating in SAR mode, the SIRAL instrument on-board CryoSat-2 uses just one antenna to transmit and receive. As opposed to emitting a single pulse, the instrument emits a burst of phase-coherent pulses, which enables it to further reduce its along-track footprint and target multiple locations simultaneously. Each successive burst lasts 3.6 ms and consists of 64 individual pulses [*C R Francis*, 2007]. The returns are Doppler processed as with conventional SAR altimetry (Section 2.3.3) to form narrow beams along-track (Figure 2.7). The beams from each burst are made to overlap with the beams from other bursts in exact coincidence by adjusting the look angle of the central beam (the angle at which the beam "looks" at the surface as measured from the vertical at the antenna), and in turn all other beams. Over multiple bursts a given beam location is sensed multiple times. The reduction in CryoSat-2's along-track footprint due

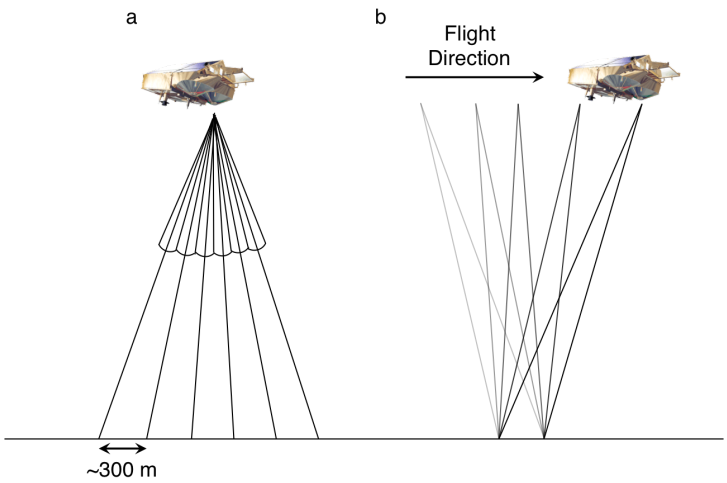

Figure 2.7: CryoSat-2 beam formation process. (a) The satellite emits a burst of phase-coherent pulses. For simplicity, only six pulses are illustrated, rather than the full 64. Beams are formed in the forward and backward looking directions, with an along-track width of ~300 m. (b) Beams from multiple bursts overlap at the same location. These beams are gathered in a 'stack', and the waveforms are summed in a process known as 'multi-looking' to provide CryoSat-2 Level 1b (L1b) 20 Hz waveforms. Adapted from *Wingham et al.* [2006].

to beam formation enables it to resolve a higher density of sea ice features, such as sea ice leads, compared with standard pulse-limited radar altimeters such as ESA's Envisat (Figure 2.8). Orbit patterns of high lead density appear in Figure 2.8b (CryoSat-2), but are absent in Figure 2.8a (Envisat). This is due to a higher number of near-repeat tracks occurring for the CryoSat-2 orbit compared with the Envisat orbit for a given month (in this case April 2011), meaning that a greater number of leads are detected along these tracks.

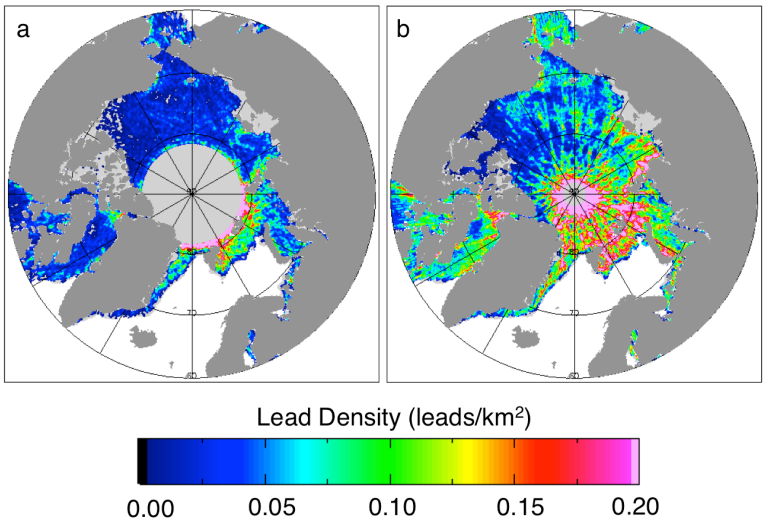

Figure 2.8: Detected sea ice lead density for April 2011. Lead density is derived from radar altimeter data from the European Space Agency's (ESA) (a) Envisat and (b) CryoSat-2 satellites.

The along-track width of each beam, Δx, is dependent on the along-track velocity of the satellite, v_s, the satellite operating frequency, f, the satellite altitude, A, and the burst length, τ_B, through:

$$\Delta x = \frac{cA}{2v_s f \tau_B} \tag{2.7}$$

For a typical CryoSat-2 velocity of 7 km s^{-1} and altitude of 720 km [*ESA/MSSL*, 2013; *Wingham et al.*, 2006], this gives a Δx of ~300 m. The across-track footprint in SAR mode is simply the antenna-limited footprint, which can reach 15 km depending on satellite altitude [*C R Francis*, 2007]. The delay time for each beam has a dependence on look angle. Therefore the delay time is adjusted to account for the different ranges

to the surface – a process known as slant range correction. After beam formation and slant range correction, all waveform returns from beams at the same location are gathered together in a 'stack'. The power of each return waveform in the stack has a dependence on incidence angle (the angle between the incident beam and the normal to the intercepted surface) (Figure 2.9), which results partly from variations in surface backscattering. Over a flat, homogenously rough surface, the maximum power occurs when the beam is nadir-pointing (Figure 2.9a). Over a flat, specular surface, the spread of power with incidence angle narrows (Figure 2.9b). The standard deviation of backscattering variation for all waveforms that make-up the stack is known as the stack standard deviation (SSD), which is an important parameter for the distinction of different surface types. The waveforms from each stack are averaged into one composite waveform – a 20 Hz waveform – in a process know as 'multi-looking' [*ESA/MSSL*, 2013] (Figure 2.7). The 20 Hz waveforms are provided with the CryoSat-2 Level 1b (L1b) data product, along with SIRAL instrument information relating to each waveform. The burst-mode SAR processing adopted by SIRAL is described in detail in *Raney* [1998] and *Wingham et al*. [2006]

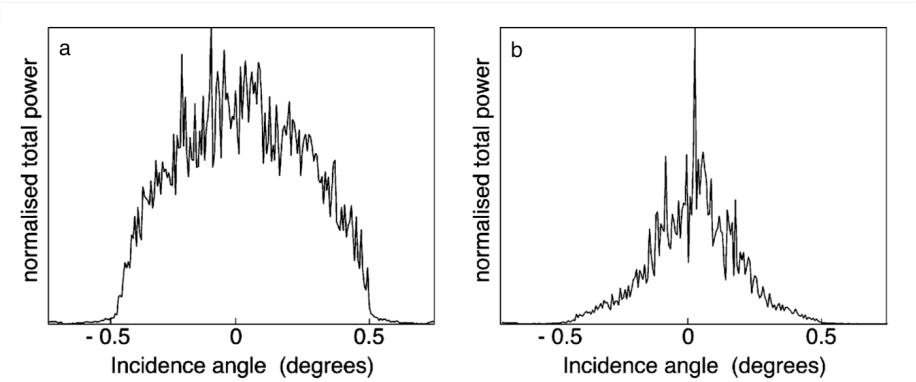

Figure 2.9: Variation of time-integrated (total) echo power in CryoSat-2 Synthetic Aperture Radar (SAR) mode. (a) Over a flat, homogenously rough surface. (b) Over a flat, specular surface. The fluctuations are the result of radar speckle. From *Wingham et al*. [2006].

2.4.4. SARIn mode

In SARIn mode, the along-track processing remains the same as SAR mode. However, the second receive antenna is activated to obtain additional across-track information [*Jensen*, 1999]. Following pulse emission, both antennae receive the return signal almost simultaneously. If the signal originates from anywhere on the ice surface other

than satellite nadir, then there will be a difference in the path lengths of the signal received at each antenna. It is therefore possible to derive the angle between the baseline (joining the antennas) and the echo direction (origin) by interferometry. SARIn mode is used to estimate the across-track surface slope to account for slope-induced errors when estimating range.

3. A method to estimate Arctic sea ice thickness and volume from CryoSat-2 Data

3.1. Introduction

This chapter provides an end-to-end, comprehensive description of the data processing steps employed to estimate Northern Hemisphere sea ice thickness and volume using CryoSat-2 radar altimeter data. This is a sea ice processing chain that has been under constant development at CPOM UCL since the early 1990s [*Laxon*, 1994]. Past studies and technical documents have documented aspects of its evolution [*Giles et al.*, 2008a; *Laxon et al.*, 2003; *Laxon et al.*, 2013; *Peacock and Laxon*, 2004; *Ridout*, 2012] and provided an analysis of the sources of error and uncertainty in the retrieval of sea ice thickness from satellite altimetry [*Giles et al.*, 2007]. At the end of this chapter an uncertainty budget is developed for Northern Hemisphere sea ice thickness and volume.

3.2. CryoSat-2 data

CryoSat-2 L1b SAR and SARIn mode data are used to estimate Arctic sea ice thickness and volume. The L1b data contain measurement information for each 20 Hz waveform along the ground track of the satellite. Each ground track constitutes around 3,000 waveforms, on average. The generation of L1b CryoSat-2 data and the 20 Hz waveforms are described in Section 2.4.3. For SAR and SARIn modes, the L1b data include the average multi-looked echo power, satellite altitude, window delay, measurement time, geolocation, geophysical corrections, a measurement confidence data (MCD) flag (to indicate a number of potential problems that may arise with each waveform), surface type (open ocean, closed sea, continental ice, or land), SSD (Section 2.4.3 and Figure 2.9), and numerous other SIRAL instrument measurements [*ESA/MSSL*, 2013]. In the L1b data ESA have applied the precise satellite orbit and instrument corrections to the window delay and satellite altitude computations respectively, and they are also provided in the product. The geophysical corrections provided in the product have not been applied to the window delay or satellite altitude. In SARIn mode the multi-looked echo is complex, and therefore the L1b product also contains phase differences and coherence terms for each bin of the echo, computed by comparing the echoes received by both antennas. In SAR mode the CryoSat-2 range window explored is about 30 m, which corresponds to 128 range bins in the waveform data. In SARIn mode the range window is increased to about 120 m in order to capture the slope variation in ice sheet margins, which corresponds to 512 range

bins. ESA also produce a Level 2 (L2) data product, which provides waveform information derived from the L1b data. L2 data includes estimates of elevation for all surface types, as well as other surface parameters such as the radar backscattering coefficient.

The L1b product is derived from the SIRAL instrument Level 0 (L0) data, where L0 is the raw data product, which is then synthetic aperture processed on ground (see Section 2.4.3. for information on CryoSat-2 SAR processing). Before February 21st 2015, ESA applied an on ground processing chain known as 'Baseline-B' to the raw data, and an updated processor, 'Baseline-C', has been applied since April 1st 2015. Between February 22nd and March 31st 2015, a hybrid 'Baseline-BC' processing chain was used. All L1b data have now been re-processed by ESA using the Baseline-C processing chain. However, the data processing steps described in this chapter, and the results presented in Chapter 4, apply to Baseline-B data only as these were the data available when the work was carried out.

3.3. Ancillary data

3.3.1. Sea ice concentration

Daily and monthly Arctic sea ice concentration data, generated at the NASA GSFC, are available through NSIDC [*Cavalieri et al.*, 1996, updated yearly]. The data are generated from brightness temperature data derived from satellite passive microwave sensors using the NASA Team algorithm (Section 1.6.1). Gridded averages of the percentage of ocean area covered by sea ice are provided on a Polar stereographic projection with a grid size of 25 km square.

3.3.2. Sea ice type

Sea ice type data are provided by the Norwegian Meteorological Service (NMS) Ocean and Sea Ice Satellite Application Facility (OSI SAF) [*Andersen et al.*, 2012]. The NMS OSI SAF data defines sea ice type as FYI, MYI, ambiguous, ice free, or unclassified. The sea ice type is determined by combining large sets of brightness temperature data from the SSM/I and SSMIS instruments carried on-board DMSP satellites (Section 1.6.1) with backscatter data from the Advanced Scatterometer (ASCAT) on-board the Metop-A satellite. For SSM/I and SSMIS data, the gradient ratio (the normalised difference in brightness temperature between the 37 and 19 GHz vertically polarised channels) can be used to distinguish between ice types. At vertical polarization the brightness temperature of FYI is similar to that of MYI at radiation frequencies of ~5

GHz. The brightness temperature of MYI then drops as frequency increases, due to increased internal scattering (Figure 3.1) [*Eppler et al.*, 1992; *Svendsen et al.*, 1983]. MYI is rougher than FYI (section 1.2.2), meaning that backscatter is larger over MYI. MYI also has an additional backscatter signature compared to FYI as a result of volume scattering, particularly during winter [*Onstott*, 1992].

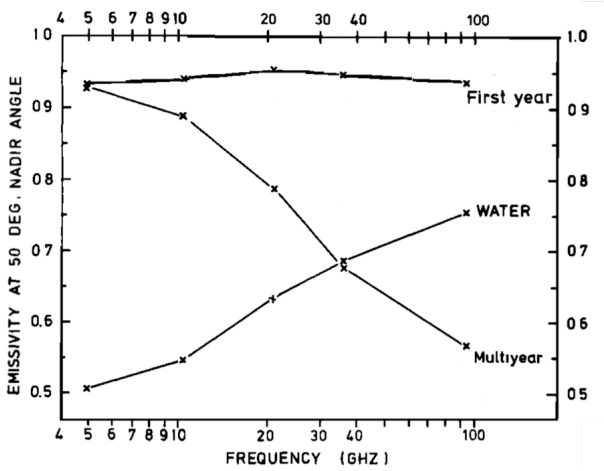

Figure 3.1: Frequency dependence of microwave emissivity over first-year ice (FYI), multiyear ice (MYI), and calm open water at vertical polarisation. Data are from surface measurements taken north of Svalbard by the Norwegian Remote Sensing Experiment (NORSEX) group, from 17 September 1979 to 12 October 1979. Adapted from *Svendsen et al.* [1983].

3.3.3. Sever Expedition sea ice data

The Sever expedition data [*Romanov*, 2004] consist of monthly mean values of sea ice freeboard, sea ice thickness and snow depth. These data were collected during spring on sea ice runways from 689 aircraft landings, between 1982 and 1988. From the Sever data the sea ice density associated with each set of measurements is calculated by setting the densities of seawater and snow to be 1025 kg m^{-3} and 324 kg m^{-3}, respectively [*Alexandrov et al.*, 2010], and following the method of Alexandrov *et al.* [2010]. Densities falling outside the range 860 to 970 kg m^{-3} are considered unrealistic and are discarded. Monthly averages where fewer than four measurements are available are also discarded.

3.3.4. Snow loading climatology

Snow loading data are obtained from a climatology [*Warren et al.*, 1999]. The climatology was compiled from *in situ* measurements of snow depth and snow density collected over MYI in the central Arctic between 1954 and 1991, with a two-dimensional quadratic function fitted to all measurements to represent the spatial variability of snow depth (Figure 3.2a-d) and density (Figure 3.2e-h). However, these quadratic functions are not constrained by *in situ* measurements outside of the central Arctic (Figure 3.2a) and the climatological snow depth has been found to agree poorly with recent snow depth observations over peripheral sea ice from satellite and airborne campaigns [*Kern et al.*, 2015]. Therefore for each month the mean climatology values of snow depth and density within the ICESat domain (Figure 1.8), where the climatology is constrained by *in situ* measurements, are used for the processing outlined in this chapter. There are also known differences between the climatology and

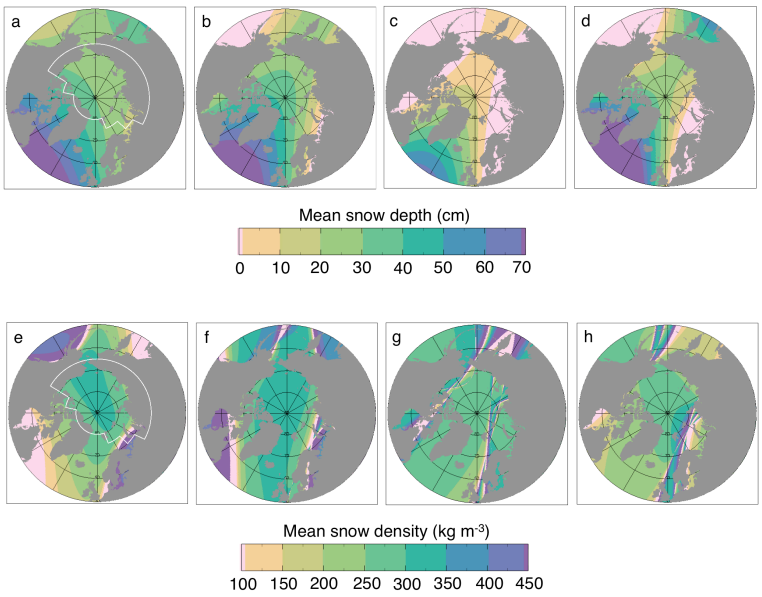

Figure 3.2: Quarterly-averaged snow depth and snow density from the Warren climatology [*Warren et al.*, 1999]. (a-d) Mean snow depth for January-March, April-June, July-September, and October-December, respectively. (e-h) Mean snow density for January-March, April-June, July-September, and October-December, respectively. Values are from the Warren climatology [*Warren et al.*, 1999]. The white polygon in (a) and (e) represents the area within which the two-dimensional quadratic function fitted to all measurements is constrained by *in situ* measurements.

the current snow depth on younger Arctic sea ice [*Kern et al.*, 2015; *Kurtz and Farrell*, 2011; *Webster et al.*, 2014]. Therefore snow depth is halved over FYI [*Kurtz and Farrell*, 2011], to account for the reduced snow accumulation compared with MYI.

3.4. Sea ice thickness and volume processing method

Section 3.4 describes the methods used to build a Northern Hemisphere sea ice thickness and volume processing system for CryoSat-2 radar altimeter data. The processor reads input L1b files and analyses and outputs one file at a time. A flowchart outlining the processing steps is shown in Figure 3.3. It is intended that the theory and methods described may act as a guide to developing a sea ice processing system for any polar orbiting satellite radar altimeter.

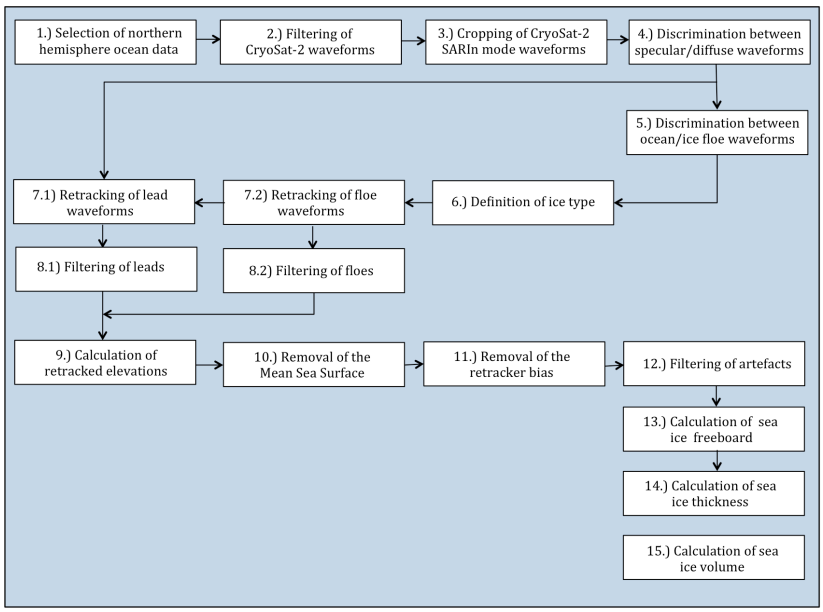

Figure 3.3: A flowchart showing the processing steps required to estimate Arctic sea ice thickness and volume from CryoSat-2 Level-1b data.

3.4.1. Pre-processing of CryoSat-2 data

The latitude range within which Northern Hemisphere sea ice is found is set as 40°N-90°N. Any data-points outside of this range are removed from the processing. Next, the surface type flag is used to remove all non-ocean waveforms, and the MCD flag (introduced in Section 3.2) is used to remove all waveforms that are fatally degraded. Waveforms may be fatally degraded due to a computation error with the window delay

or automatic gain control (AGC), or if the value for either of these parameters falls outside of a specified range. The window delay refers to the two-way delay time between pulse emission and the reference point at the centre of the range window, which for CryoSat-2 is centrally located; at bin 63 for LRM and SAR mode and bin 255 for SARIn mode, where bins are counted from bin zero. CryoSat-2 implements AGC to adjust the receiver sensitivity for the best reception of signals with varying return powers. AGC uses information about the previous return signal level to adjust the receiver gain in anticipation of the next. The aim is to keep the signal level as constant as possible. [*ESA/MSSL*, 2013]. Waveforms can also be fatally degraded due to inaccurate or missing information regarding the time that the radar pulse was reflected from the surface.

To allow for identical processing of both SAR and SARIn mode data acquired over Arctic sea ice, SARIn mode waveforms are cropped to include only the central 128 bins (bins 100-277, where bins are counted from bin zero) so that they are the same length as SAR mode waveforms. This assumes that the return waveforms from both modes are positioned at approximately the same location within the range window. The additional phase and coherence information available in the SARIn mode product is not required for sea ice processing. The individual SAR and SARIn mode files are then merged into single files for each Arctic ground track of the satellite, using the time stamps of the first and last waveforms in each individual file. Each timestamp is expressed as 3 integers; the day, seconds of the day, and microseconds. The orbital period of CryoSat-2 is extremely stable [*Wingham et al.*, 2006], allowing the time of the ascending equator crossing before each Arctic pass and the descending equator crossing after each Arctic pass to be accurately computed.

3.4.2. Discrimination between sea ice and ocean waveforms

To discriminate between measurements of the ocean surface and the ice surface it is necessary to identify which echoes are specular and which are diffuse [*Drinkwater*, 1991; *Peacock and Laxon*, 2004]. Specular echoes occur when the radar burst is reflected from a smooth, mirror-like surface such as a lead or very thin ice. These regions are smooth because they tend to be sheltered from wind and experience low fetch (the distance that a given wind has blown over the water) [*Wadhams*, 2000]. In these cases the power in the range window rises and falls again very rapidly, creating an echo that looks like a spike (Figure 3.4a). Diffuse echoes occur when the radar burst is reflected from a rougher surface such as an ice floe or the open ocean. In these cases the power in the range window rises rapidly but gently decays, creating an echo that looks like a step (Figure 3.4b) (Section 2.3.2).

Specular and diffuse echoes are identified by the values of their SSD and pulse peakiness. The SSD parameter uses the multi-looking capability of CryoSat-2 to provide a measure of the variation in surface backscatter with incidence angle. It was described in Section 2.3.4 and shown in Figure 2.9. The pulse peakiness is defined as:

$$PP = \frac{P_{max}}{P_{mean}} \tag{3.1}$$

where PP is the pulse peakiness, P_{max} is the maximum return power of the echo, and P_{mean} is the mean return power. Pulse peakiness is only calculated for bins where the return echo power is above the noise floor, where the noise floor is defined as the mean power in bins 10-19, and zero is the first bin. The higher the pulse peakiness, the more the echo looks like a spike. Specular echoes are defined as those with a pulse peakiness greater than 18 and a SSD less than 4, and diffuse echoes as those with a pulse peakiness less than 9 and a SSD greater than 4. Echoes with a pulse peakiness or SSD between these values are considered complex and removed from the processing. During the sea ice melt season it becomes difficult to discriminate between measurements from leads and the ice surface due to melt ponds forming on sea ice. Melt ponds cause specular echoes from ice floes, and eventually specular echoes dominate the return waveforms. Therefore the sea ice processor is not run in the months of May-September.

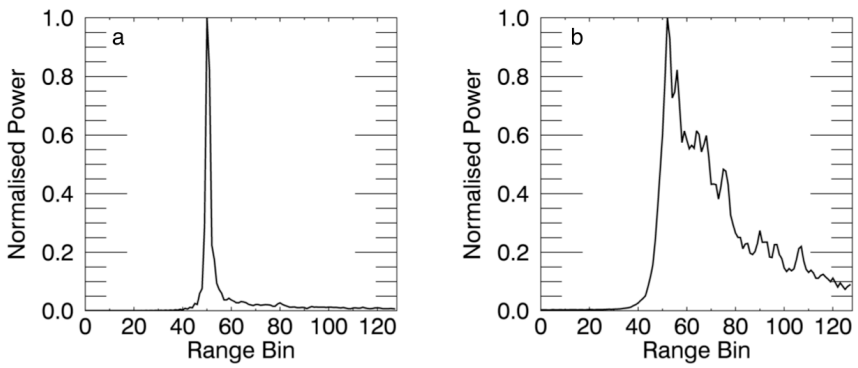

Figure 3.4: Example CryoSat-2 waveforms. (a) A specular return echo, (b) A diffuse return echo.

The next step is to differentiate between radar echoes from sea ice floes and echoes from the ocean, as both get classified as diffuse according to the above definitions. Ice floe regions are defined as those with a sea ice concentration (Section 3.3.1) greater than 75%, and ocean regions as those with a concentration of 0%. Echoes from

regions with an ice concentration between these values are not trusted to come from either ice floes or open ocean, and are removed from the processing. The floe concentration threshold was derived empirically – the aim is for it to be high enough to avoid incorrectly classifying open water as an ice floe region. This could occur due to the relatively low resolution of the sea ice concentration data.

3.4.3. Definition of sea ice type

Daily sea ice type data (Section 3.3.2) is used to flag sea ice measurements as FYI, MYI, ambiguous, ice free, or unclassified. Records are removed where the ice type is ice-free, unclassified, or ambiguous. The ambiguous classification often relates to a thin band of ice between FYI and MYI regions. This band is highly mobile during the course of a month, so its removal does not cause gaps in monthly maps of sea ice thickness, and should not significantly affect monthly volume estimates. Maps of sea ice type, for the same day each year (Figure 3.5), show inter-annual variation in the location of the FYI and MYI edges. But in all years the MYI cover is concentrated around the coast north of Greenland and the Canadian Archipelago, and often extends into the central Arctic.

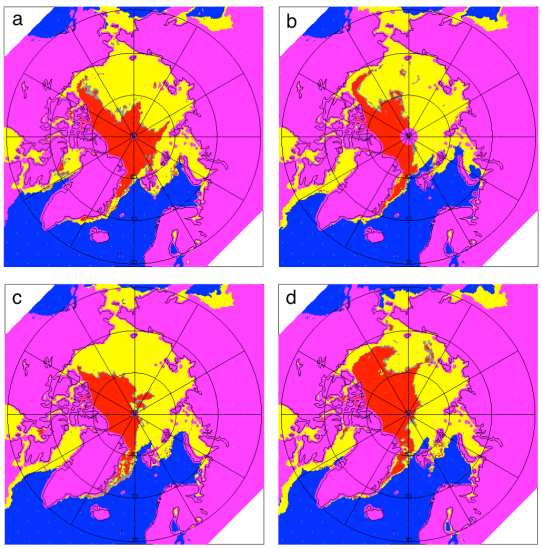

Figure 3.5: Interannual variation in Northern Hemisphere sea ice type. The maps show sea ice type for January 31st (a) 2011, (b) 2012, (c) 2013, and (d) 2014. Yellow shading represents first year ice (FYI), red represents multi year ice (MYI), blue represents areas where sea ice is not present, grey represents an ambiguous ice type, and pink represents areas where the sea ice type has not been set in the data, which correspond to areas of land cover.

3.4.4. Waveform retracking

For each echo, a specific point is selected on the waveform leading edge to mark the location of the ocean or ice surface. This point often deviates from the reference point to which the window delay is measured, which for CryoSat-2 L1b data is the central range bin, bin 64. The purpose of this process, known as retracking, is to find the location within the range window where the returned power comes from the surface at nadir. The assumption that the retracking point represents the nadir return can be violated when applied to SARIn data [*Armitage and Davidson*, 2014], but the specular echo retracker (Section 3.4.4.1) and diffuse echo filtering (Section 3.4.4.2) act to remove any SARIn waveforms for which the assumption fails. This value is returned as a bin number from the retracking routine and used later in the calculation of the surface elevation (see Section 3.4.5). A different retracking routine is applied depending on whether the surface return is specular (corresponding to a lead), or diffuse (corresponding to open ocean or a sea ice floe).

3.4.4.1. Specular echo retracking

The specular echoes from leads are retracked using a retracking method first presented in *Giles et al*. [2007]. This method uses two functions to describe the shape of a specular echo. The first part of the echo is represented by a Gaussian function (where $f = f_1$ in Equation (3.2)). The second part of the echo is represented by an exponentially decaying function (where $f = f_2$ in Equation (3.2)). These two functions are linked by a third linking function (where $f = f_L$). The full retracking function is:

$$P_r(t; a, t_0, k, \sigma) = ae^{-f(t)^2} \tag{3.2}$$

where

$$f(t) = f_1(t) = \frac{t - t_0}{\sigma} \qquad -\infty < t < t_0$$

$$f(t) = f_1(t) = a_3(t - t_0)^3 + a_2(t - t_0)^2 + \frac{1}{\sigma}(t - t_0) \qquad t_0 < t < (t_b + t_0) \tag{3.3}$$

$$f(t) = f_2(t) = (k(t - t_0)^{\frac{1}{2}}) \qquad (t_b + t_0) < t < \infty$$

$$t_b = k\sigma^2 \tag{3.4}$$

$$a_2 = \frac{5k\sigma - 4\sqrt{kt_b}}{2\sigma t_b \sqrt{kt_b}} \tag{3.5}$$

$$a_3 = \frac{2\sqrt{kt_b} - 3k\sigma}{2\sigma t_b^2 \sqrt{kt_b}} \tag{3.6}$$

where $P_r(t)$ is the power at time t, a is the maximum amplitude of the echo, t_0 is the time that $P_r(t) = a$, t_b is the time period for which $f = f_L$, k governs the rate of decay of the exponentially decaying function, and σ is the standard deviation of the Gaussian function. a_2 and a_3 are chosen such that the function, P_r, and its first derivative, are smooth and continuous.

The retracking function is fit to each CryoSat-2 waveform using the Levenberg-Marquardt non-linear least-squares method [*Marquardt*, 1963]. The fitting algorithm (http://users.ics.forth.gr/~lourakis/levmar/index.html) varies the fitting parameters a, σ, t_0 and k to minimise the sum of the squares of the differences between the waveform samples and the fitted function, and reports it at the end of each iteration. The fit is run for a maximum of 3000 iterations and the retracking point is selected for the iteration where the sum-squared difference is at its minimum. The retracking point is the location of the maximum amplitude of the fitted function, t_0. The retracker returns the bin number, b_0, corresponding to the retracking point, t_0. If an acceptable fit is not achieved after 3000 iterations then the echo is removed from processing. In these cases the echoes differ in some way from the standard specular echo shape. For example, the lead dominating the return signal may be located away from the nadir of the satellite [*Armitage and Davidson*, 2014].

3.4.4.2. Diffuse echo retracking

Open ocean and sea ice floe waveforms are noisier than those originating from leads, especially in the case of SARIn data. Therefore diffuse echoes are smoothed using a three-point moving average before retracking. The surface height of the sea ice surface can be derived from the waveform leading edge, by determining the point along the edge that corresponds to the average surface. This will coincide with the two-way

travel time for the midpoint of the pulse to reflect from the mean surface at nadir [*Rapley et al.*, 1983]. Therefore diffuse echoes are retracked using a threshold retracker. The tracking point is positioned where the leading edge rise of the echo first reaches 70% of the amplitude of its first peak. As the echo bin count will cross the 70% threshold somewhere between two bins, the exact tracking bin number, b_0, is located by linear interpolation. The threshold is applied to the first peak rather than the peak of maximum amplitude, as the maximum may be caused by off-nadir ranging to leads. To be defined as the first peak, a peak must have an amplitude of 20% of the maximum, or higher.

The echo is retracked to the 70% power threshold, rather than the 50% threshold of conventional, pulse-limited altimetry [*Femenias et al.*, 1993b; *Rapley et al.*, 1983] due to the synthetic aperture operation of CryoSat-2 over sea ice regions. The surface illumination pattern for a regular pulse-limited altimeter is described in Section 2.3.2 and shown in Figure 2.3. A typical pulse-limited echo is shown in Figure 2.4. In pulse-limited altimetry the location of the mean surface height within the antenna footprint is taken to be the position where the leading edge rise of the echo first reaches 50% of the amplitude of maximum power, for surfaces with a Gaussian height distribution (returned power is proportional to illuminated area) such as sea ice [*Femenias et al.*, 1993b; *Kurtz et al.*, 2014]. However, during CryoSat-2 processing, the radar bursts are separated into strips arranged across-track, which are sensed multiple times from multiple angles (Section 2.4.3 and Figure 2.7). Due to the synthetic, strip-like illumination pattern of each beam and the process of slant-range correction (Section 2.4.3), the point on each return waveform that corresponds to the surface does not lie at the half-power point of the leading edge [*Wingham et al.*, 2006], but closer to 70% of the maximum.

Diffuse echoes are flagged as invalid in cases where the leading edge rise is complex, as these echoes typically produce anomalously low surface elevations. To detect echoes with a complex leading edge rise the leading edge width of each echo is calculated. The width of the leading edge is defined as:

$$W_{le} = (b_{70} - b_{30}) \tag{3.7}$$

where W_{le} is the width of the leading edge rise in number of bins, b_{70} is the altimeter echo range bin number corresponding to the 70% threshold of the first peak, and b_{30} is the altimeter echo range bin number corresponding to the 30% threshold of the first peak. Waveforms with leading edge widths larger than three bins are removed from processing (Figure 3.6). Causes of such echoes over sea ice floes could include off-

nadir reflection to leads [*Armitage and Davidson*, 2014], or reflection from a very rough surface (surface roughness ~1.5 m and above), such as a heavily deformed or ridged ice.

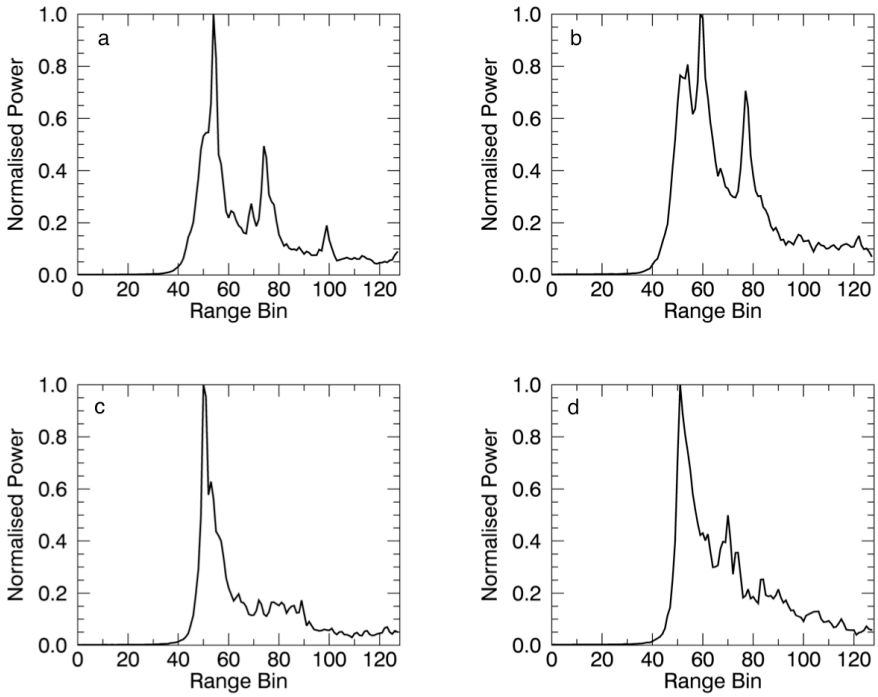

Figure 3.6: CryoSat-2 radar altimeter echoes from an Arctic sea ice floe region. (a) and (b) Leading edge rise greater than three bins. These echoes will be removed from processing. (c) and (d) Leading edge rise smaller than three bins. These echoes will be included in processing. The exact values of the leading edge widths are (a) 5.96, (b) 3.34, (c) 1.37 and (d) 1.61.

3.4.5. Calculation of sea ice and ocean elevations

The next step is to compute the ocean surface elevations in the leads between sea ice floes, and the surface elevations of the sea ice floes. It is assumed that the radar pulses penetrate through any snow cover on ice floes and scatter from the snow-ice interface, which has been shown in laboratory experiments where the snow cover on sea ice is cold and dry [*Beaven et al.*, 1995], as is the case during Arctic winter. Despite some evidence that the scattering horizon migrates as temperature rises [*Willatt et al.*, 2010], there is no bias observed in the CryoSat-2 thickness retrievals when compared to year-round ice draft data from ULS buoys. The comparison is presented in *Tilling et al.* [2015] and will be described in detail in Section 4.3. It is therefore concluded that the migration of the scattering horizon has a minimal impact on sea ice thickness retrievals from CryoSat-2 over the sea ice growth seasons for

which they are calculated. The elevation of the lead or floe surface is computed as:

$$E = A - R_0 \tag{3.8}$$

which is equivalent to Equation (2.1) and shown schematically in Figure 2.1. For CryoSat-2 sea ice processing, E is the elevation of the lead or floe surface above the WGS84 reference ellipsoid, A is the altitude of the satellite centre of gravity (COG) above the same ellipsoid, and R_0 is the range of the satellite to the lead or floe surface. The satellite COG is located at the centre of the single, spherical fuel tank [*Wingham et al.*, 2006] and will not move during the satellite lifetime. R_0 is computed using:

$$R_0 = R_n + C_G + C_R \tag{3.9}$$

where

$$R_n = \frac{ct_n}{2} \tag{3.10}$$

and

$$C_R = (b_0 - b_n)\Delta_b \tag{3.11}$$

where R_n is the range of the satellite to the surface represented by the nominal tracking bin, C_G represents the geophysical corrections that are applied, C_R is the retracking correction, t_n is the two-way travel time of the radar signal to the surface represented by the nominal tracking bin, b_0 is the bin number returned by the lead or floe retracker (Section 3.4.4), b_n is the bin number of the nominal tracking bin, and Δ_b is the bin width (0.2342 m). For SAR and cropped SARIn data, b_n is centrally-located, at bin 63 of the range window, where bins are counted from zero. C_G accounts for the effects of tides and atmospheric pressure on the surface elevations, and the effect of radar range delay due to propagation through the atmosphere. The geophysical corrections applied are taken from the CryoSat-2 L1b data product, and are: dry tropospheric, wet tropospheric, inverse barometric, modelled ionospheric, ocean tide, long period equilibrium tide, ocean loading tide, solid earth tide, and geocentric polar tide. Finally, C_R accounts for the fact lead and floe surfaces are located at bin b_0, the bin number returned by the specular or diffuse echo retracker, rather than the nominal tracking bin of CryoSat-2.

3.4.6. Removal of the mean sea surface

At this point, the dominant signal in the sea ice and ocean elevations will be due to the Earth's geoid and the mean circulation of the ocean currents, which together make up the mean sea surface (MSS). This is a fixed signal that is removed from all elevation estimates before continuing. The MSS model that is removed is the UCL 2013 (UCL13) MSS [*Ridout*, 2014]. This was built using two complete 369 day repeat cycles of CryoSat-2 from September 24th 2011 to September 30th 2013 and improves on earlier MSS models in the region north of 81.5°N, where previously no satellite radar altimetry data was available. Two years of data was considered sufficient to capture the mean state of the ocean circulation and account for tracks that may be missing in just one year of data. The UCL13 MSS is now used by ESA to produce L2 Baseline-C CryoSat-2 data (Section 3.2), and is included in the L2 product. Once the MSS has been removed, the remaining sea level anomaly (SLA) signal will be due to time variant changes in the ocean surface elevation (the ocean dynamic topography). It is important to note however that long wavelength errors in tides and atmospheric corrections will remain.

After removal of the MSS, the occasional satellite ground track is observed where sea ice and ocean elevations are shifted by a few metres with respect to the MSS, for all measurement points along the track (Figure 3.7). This is physically unlikely, as the Arctic ocean dynamic topography varies on a scale of a few hundred kilometres with a maximum amplitude of around 0.5 m [*Kwok and Morison*, 2011]. The shift can have a variety of causes, such as errors in the orbit determination or missing geophysical corrections. Shifted tracks are detected by computing the mean SLA for each track, from the individual lead elevation measurements along it. Before calculating the mean SLA for each track, individual leads with a SLA more than 20 m or less than -20 m are removed as they are regarded as noise spikes. Tracks are then removed where the mean SLA is lower than -0.5 m or greater than 0.5 m. Often the shift persists for several orbits. For example, Figure 3.7 shows a cluster of tracks enclosed by a black dashed rectangle that are all shifted by a few metres with respect to the MSS. The mean SLA of this cluster is -2.3 m. of the geophysical corrections normally applied (Section 3.4.5), the dry tropospheric, wet tropospheric and inverse barometric geophysical corrections were missing in the input data for each track in this cluster, which likely caused the anomalously low mean SLA.

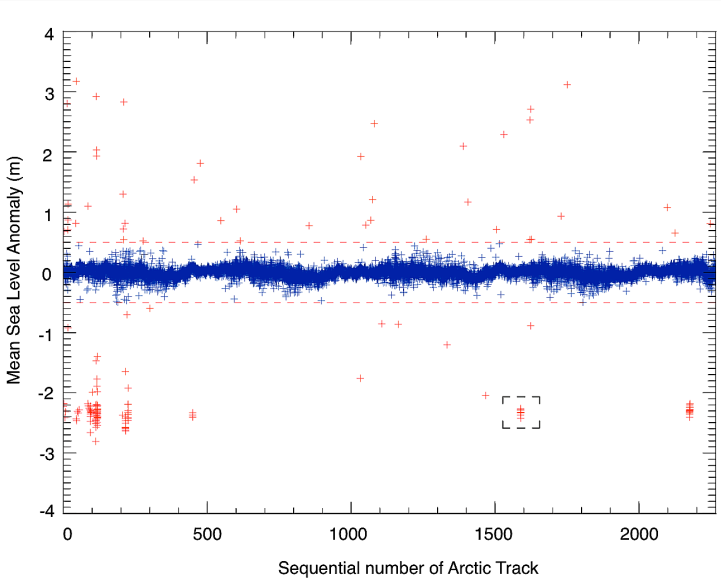

Figure 3.7: Mean sea level anomaly (SLA) from CryoSat-2. Mean SLA is shown for all Arctic satellite tracks up until January 2015. The tracks are numbered in sequence of when they occurred. The red dashed line marks the ±0.5 m mean SLA limit, outside of which tracks are removed from the processing. Red crosses are tracks that are removed. Blue crosses are tracks that remain. The black dashed rectangle encloses the cluster of tracks discussed in the main text.

3.4.7. Retracker bias

As different retracking methods are used for specular and diffuse waveforms (Section 3.4.4), a fixed bias is introduced between elevation estimates from leads and the sea ice surface, which will affect subsequent freeboard (Section 3.4.8) and thickness (Section 3.4.9) estimates. This bias arises because the tracking points on specular and diffuse ocean waveforms are approximated by different theoretical returns. Therefore for one or both types of waveform, the approximation may differ slightly from the true tracking point, leading to a range bias between the two retracking techniques. To investigate the nature of the bias, ocean elevation estimates are compared using the two retracking methods in the Hudson Bay, which is a region of seasonal ice cover. During June and July there in no MYI cover in the Hudson Bay and the rate of ice retreat is rapid. Therefore in some places specular echo returns from very thin ice are interspersed with diffuse echo returns from areas of open water, which are similar to those from ice floes. Two satellite ground tracks were selected from June and July 2011, where the SLA profile was relatively flat (no clear influence of tides or dynamic topography), and low-noise sequences of open water returns were interspersed with low-noise sequences of thin, flat ice returns. The thin ice echoes were then retracked

using the specular echo retracker (Section 3.4.4.1) and open water echoes using the diffuse echo retracker (Section 3.4.4.2), to produce SLA profiles for the two tracks (e.g. Figure 3.8). SLAs estimated using the diffuse echo retracker are positively biased with respect to those estimated using the specular echo retracker. To compute the bias a straight-line fit was performed through the SLAs from the specular echo retracker. Then the difference of each SLA from the diffuse echo retracker from this line was calculated. The mean value of the difference over both ground tracks, and therefore the bias, was 16.26 cm. This value is deducted from all elevation estimates returned by the diffuse echo retracker. It would be beneficial to repeat the analysis of retracker bias in different regions or at a different time of year, but it requires very specific conditions that are not common in regions of Arctic sea ice cover.

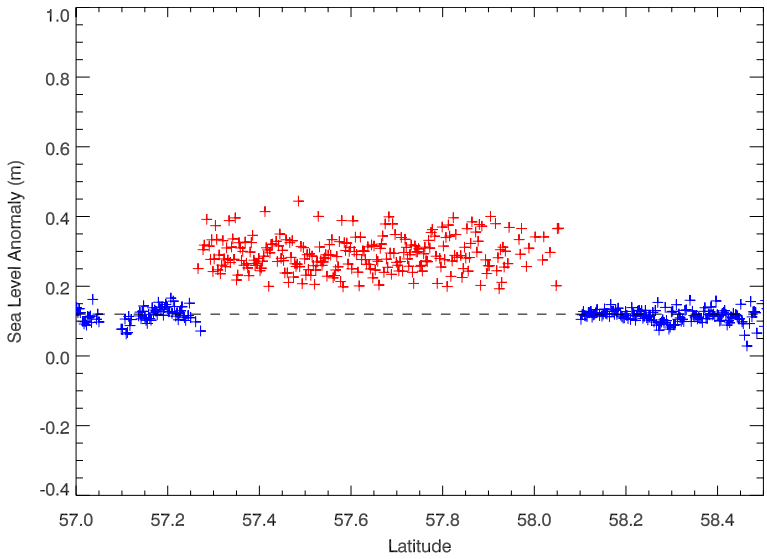

Figure 3.8: Sea level anomaly (SLA) profile from CryoSat-2. The profile is from a ~150 km Hudson Bay track on 16th July 2011. Red stars show the SLA computed using the diffuse echo retracker over open ocean. Blue stars show the SLA computed using the specular echo retracker at leads. The dashed blue line shows the interpolated SLA between leads, which is constructed using a straight line fit to all lead measurements. SLAs measured with the diffuse echo retracker are positively biased with respect to those measured with the specular echo retracker, with a mean value of 16.26 cm.

3.4.8. Calculation of sea ice freeboard

Sea ice freeboard is the elevation of the ice surface above the ocean. Before the calculation of sea ice freeboard, all lead measurements with a SLA of more than ±3 m are removed from processing (Figure 3.9). SLA values outside of this range are likely

to be caused by noise in the retracking step. For example, there might be a second peak in the specular waveform that is selected by the retracking algorithm, rather than the first peak. The majority of SLAs lie within the smaller range of ±0.5 m. Of the 81 million lead measurements collected between October 2010 and January 2015, 99.84% of the resulting SLAs lay within ±3 m and 98.06 % within ±0.5 m.

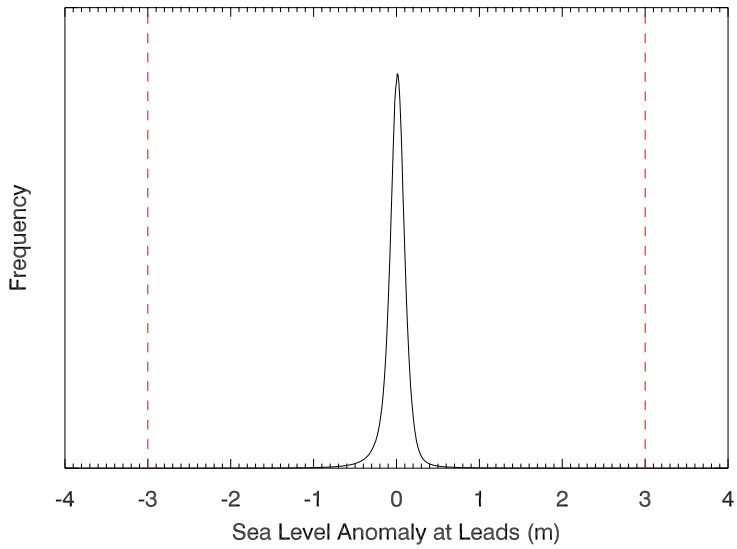

Figure 3.9: A normalised histogram of CryoSat-2 sea level anomaly (SLA) estimates. All lead measurements from October 2010 to January 2015 are included. SLA values outside the range ±3.0 m (red dashed lines) are removed from processing.

Sea ice freeboard is calculated for each waveform classed as containing an ice floe, or ice floes, which between October 2010 and January 2015 was 55 million waveforms. To calculate sea ice freeboard the ocean surface elevation beneath the ice floe is subtracted from the floe elevation. The ocean surface elevation beneath sea ice floes is calculated by interpolating the ocean surface elevation between leads, by using linear regression to perform a fit to the lead elevations extending 100 km either side of each floe location. The 100 km interpolation scale was chosen to ensure that ocean elevations were sufficiently interpolated without over-smoothing. At least one lead must be present on either side of the floe for the interpolation to be valid. Freeboard values outside the range -0.3 m to 3.0 m are removed from processing. These limits were selected by analysing a histogram of all freeboards between October 2010 and January 2015 (Figure 3.10). Large negative freeboard values are likely to be caused by errors in the floe retracking and are removed, but slightly negative freeboards are

permitted to allow for random noise in the returns from thin ice floes and ensure that the average freeboard is not biased high. The upper limit of 3 m was chosen as a means to remove extreme outliers, as the diffuse echo retracker occasionally returns anomalously large freeboard values. These values are likely a consequence of complex echoes whose leading edge width did not meet the removal criteria at the earlier stage of processing (Section 3.4.4.2), or of poor reconstruction of the ocean surface elevation through interpolation. Poor reconstruction of the ocean surface becomes more of an issue close to land, where fewer lead measurements are available. However, outliers of this magnitude are uncommon. For example, there was an average of 16 freeboard measurements larger than 3 m in March (towards the end of the ice growth season), for 2011-2014, and none exceeding 4 m. For all sea ice floe measurements from October 2010-January 2015, the mean freeboard was 14.75 cm with a standard deviation of 17.18 cm.

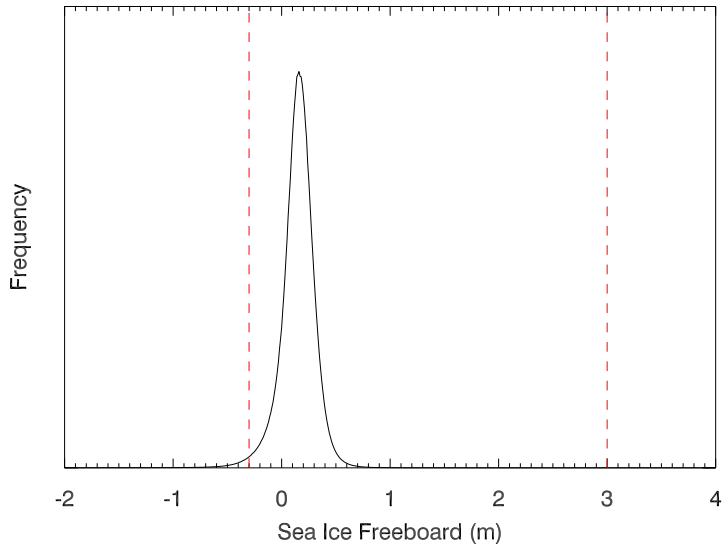

Figure 3.10: A normalised histogram of CryoSat-2 sea ice freeboard estimates. All floe measurements from October 2010 to January 2015 are included. The mean freeboard is 14.75 cm, with a standard deviation of 17.18 cm. Freeboard values outside the range -0.3 m to 3.0 m (red dashed lines) are removed from processing.

Finally a correction is applied to account for the reduced propagation speed of light through the snow cover on sea ice floes. The corrected freeboard is given by:

$$f_c = f_i + h_s\left(\frac{c_v}{c_s} - 1\right) \quad (3.12)$$

where f_c is the corrected sea ice freeboard, f_i is the original sea ice freeboard, h_s is the snow depth, c_v is the speed of light propagation in a vacuum (3.0×10^8 m s^{-1}), and c_s is the speed of light propagation in snow (2.4×10^8 m s^{-1}) [*Giles et al.*, 2008a; *Kwok et al.*, 2011]. Therefore corrected freeboard is simply expressed as:

$$f_c = f_i + 0.25h_s \quad (3.13)$$

3.4.9. Calculation of sea ice thickness

Sea ice freeboard is converted to sea ice thickness by assuming that the ice floes are floating in hydrostatic equilibrium [*Laxon et al.*, 2003] (Figure 3.11). This means that sea ice thickness can be calculated using:

$$h_i = \frac{f_c\rho_w + h_s\rho_s}{\rho_w - \rho_i} \quad (3.14)$$

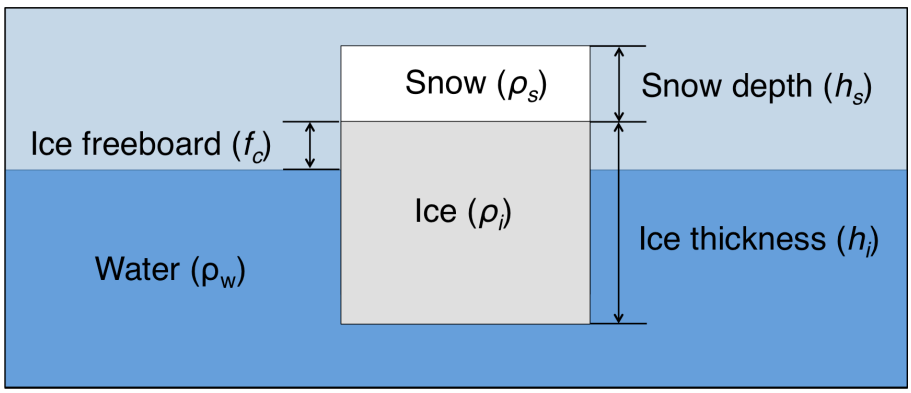

Figure 3.11: Schematic of a sea ice floe, floating in hydrostatic equilibrium

where h_i is the sea ice thickness, f_c is the corrected sea ice freeboard, ρ_w is seawater density (1023.9 kg m^{-3}) [*Wadhams et al.*, 1992], h_s is the snow depth, ρ_s is the snow density, and ρ_i is the sea ice density. The snow depth application is described in detail in Section 3.3.4. Fixed sea ice density values of 916.7 kg m^{-3} and 882.0 kg m^{-3} are

applied to FYI and MYI respectively [*Alexandrov et al.*, 2010], to account for the higher fraction of air-filled pores in MYI [*Wadhams*, 2000].

3.4.10. Calculation of sea ice volume

To calculate sea ice volume, each individual ice thickness measurement is assigned a corresponding ice concentration value from NSIDC concentration data, which is provided on a 25 km square grid (Section 3.3.1). The concentration assigned is the value from the NSIDC concentration grid cell that is nearest to the location of the thickness measurement, converted to a fractional ice concentration. Sea ice volume is calculated monthly, so all CryoSat-2 thicknesses and their corresponding concentrations are averaged onto a 0.5° longitude by 0.1° latitude grid for each month. The grid cells are considered empty if they contain less than five ice thickness measurements, and are filled using a nearest neighbour interpolation with a maximum search radius of 300 km.

Next a sea ice extent mask is computed, which is needed to define the sea ice edge, using NSIDC ice concentration data from the 15th day of each month. Each 0.5° by 0.1° grid cell is assigned the NSIDC concentration value that is nearest to its centre coordinates. If the concentration value from the 15th day is above 15%, then the cell falls within the ice extent mask and a value of one is set. A value of zero indicates that the cell is not within the extent mask. As a small number of grid cells will encompass land an additional dataset is produced that contains the fraction of ocean in each cell. This is done using the Generic Mapping Tools (GMT) function *grdlandmask* [*Wessel and Smith*, 1991; *Wessel et al.*, 2013]. The final 'cell volume' for each measurement location on the grid is the product of the sea ice thickness, the fractional sea ice concentration, the cell area, the sea ice extent mask, and the fraction of the cell believed to be ocean. The sum of all filled cell volumes gives the total, Arctic-wide, sea ice volume.

Sea ice volume is also computed for FYI and MYI separately. In each cell the thicknesses of FYI and MYI are summed, and then used to compute the cell fraction of FYI and MYI, as follows:

$$F_f = \frac{h_f}{h_f + h_m} \tag{3.15}$$

and:

$$F_m = \frac{h_m}{h_f + h_m} \tag{3.16}$$

where F_f is the cell fraction of FYI, h_f is the total FYI thickness falling in the cell, h_m is the total MYI thickness falling in the cell, and F_m is the cell fraction of MYI. The FYI and MYI fractions in empty cells are filled using a nearest neighbour interpolation with a maximum search radius of 300 km. The FYI and MYI fractions are used to calculate FYI and MYI sea ice volume, by multiplying the total cell volume by the fractions.

Finally, sea ice volume is computed for fixed oceanographic basins (Figure 3.12), so that volume changes can be documented in regions of oceanographic interest. These basins cover the major oceanographic regions of the Arctic [*Nurser and Bacon*, 2014], as well as the surrounding Seas and Gulfs at lower latitudes.

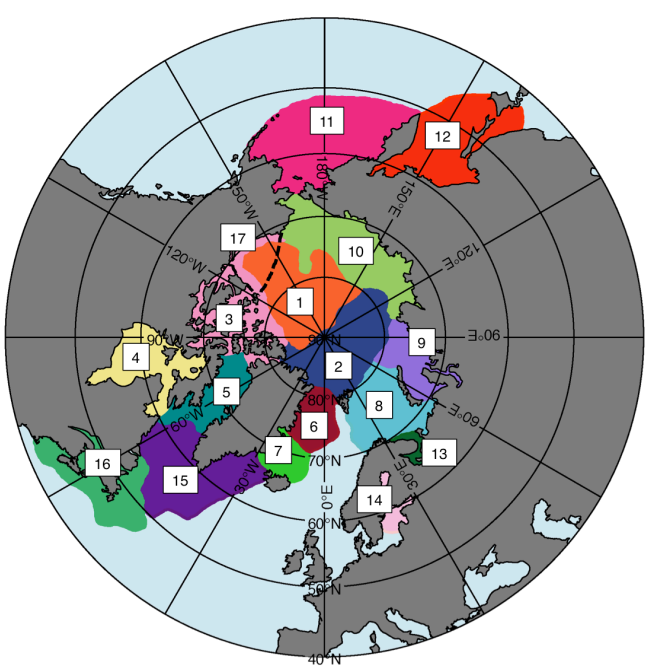

Figure 3.12: Arctic Ocean regions selected for analysis. The regions are the Amerasian Basin (1), Eurasian Basin (2), Canadian Archipelago and Northwest Passage (3), Hudson Bay & Foxe Bay (4), Baffin Bay (5), Greenland Sea (6), Iceland Sea (7), Barents Sea (8), Kara Sea (9), Siberian Shelf Seas (10), Bering Sea (11), Sea of Okhotsk (12), White Sea (13), Baltic Sea & surrounding Gulfs (14), Labrador Sea (15), the Gulf of St Lawrence & Nova Scotia Peninsula (16), and the Beaufort Sea (17). Regions 1-10 encompass all autumn sea ice, and regions 1-16 encompass all spring sea ice. Region 17 is a sub-region of region 1 and 3.

3.5. Estimation of uncertainties

3.5.1. Contributing factors

Monthly errors in sea ice thickness and volume are estimated by considering the contributions due to uncertainties in snow depth (4.0 to 6.2 cm from *Warren et al*. [1999]), snow density (60.0 to 81.6 kg m^{-3} cm from *Warren et al*. [1999]), sea ice density (7.6 kg m^{-3} from *Romanov* [2004]), sea ice extent (20,000 to 30,000 km^2 according to NSIDC), sea ice concentration (5% according to NSIDC), and sea ice freeboard (~9 cm from CryoSat-2 freeboard observations). Uncertainties in seawater density are neglected because they have a negligible impact on uncertainties in sea ice thickness and volume [*Kurtz et al.*, 2013; *Ricker et al*., 2014].

Uncertainties in snow depth and snow density are taken from a climatology [*Warren et al*., 1999], which was derived from fieldwork measurements acquired between 1954 and 1991. There are known differences between the climatology and the current snow depth on younger Arctic sea ice, as well as snow depth on sea ice in the peripheral Arctic where the climatology is not constrained by *in situ* measurements. The limitations and application of the climatology are described in detail in Section 3.3.4 The climatology provides, as an error estimate, the standard deviation of snow depth and density anomalies in each calendar month. The anomalies were defined as the snow depth or density measured at the North Pole stations operating in that year, minus the multiyear average for the latitude and longitude of the station. If more than one station was operating, the anomalies were averaged. According to the data authors, these errors are likely to be an overestimate, as the anomalies were calculated relative to measurements from only a few (typically 2) stations. Therefore to some extent the errors are recording regional anomalies that are accompanied by unsampled anomalies of opposite sign in other regions in the same month.

Uncertainties in sea ice density (FYI and MYI) are based on measurements acquired during the SEVER expeditions [*Romanov*, 2004]. These data consist of mean values of sea ice freeboard, sea ice thickness and snow depth on sea ice runways used for 689 aircraft landings between 1982 and 1988. A rearranged version of Equation (3.14) was used to calculate the ice density associated with each measurement location. For the ice density calculation, the densities of seawater and snow were set as 1,025 kg m^{-3} and 324 kg m^{-3}, respectively, following the method of *Alexandrov et al*. [2010] whose densities of FYI and MYI are applied in the CPOM UCL processing. Densities falling outside the range 860 to 970 kg m^{-3} were considered unrealistic and were discarded, and monthly averages where fewer than four measurements were available were also

discarded. Unlike the snow climatology, average sea ice densities are not available for all months as the SEVER expedition only ran in the spring. The ice density uncertainty was therefore calculated as the standard deviation of all available monthly averages, of which there were 18. This results in an uncertainty of 7.6 kg m^{-3}. This value is likely to be an overestimate of the true uncertainty due to under-sampling, as was the case with the snow depth and density uncertainties.

NSIDC estimate sea ice extent as the region where its concentration exceeds 15%, and they estimate the relative (year-to-year) error as approximately 20,000 to 30,000 km^2 (http://nsidc.org/arcticseaicenews/faq/#error_bars) – a small fraction (0.1 to 0.5%) of the total extent. NSIDC quote a figure of 5% for the uncertainty in their sea ice concentration values (http://nsidc.org/data/docs/daac/nsidc0051_gsfc_seaice.gd.html), which is important when considering local errors. As NSIDC do not estimate the distance over which the concentration uncertainty is correlated, it is assumed in this study, conservatively, that the uncertainty is correlated over the entire Northern Hemisphere for each month.

Individual freeboard measurements have a standard deviation averaging 9 cm Arctic-wide. This was calculated by computing the standard deviation of all individual freeboard measurements within a 25 km radius at 25 km increments in each month from October 2010-January 2015, then averaging over all months. The standard deviation arises through a.) uncertainties in the floe height measurement due to speckle in the radar echoes, which de-correlates from one measurement to the next, and b.) uncertainties in sea surface height, which may be correlated in space due to the interpolation scheme based on a linear regression of measurements along 200 km sections of each satellite ground track (Section 3.4.8). It is assumed that the principle source of uncertainty on an individual radar altimeter measurement of sea ice freeboard and consequent thickness is the speckle on the echo [*ESA/UCL*, 2001; *Laxon et al.*, 2013; *Wingham et al.*, 2006], which introduces noise in maps of sea ice freeboard and thickness. Therefore sea ice thickness data are output on to a 5 km square grid, to reduce speckle error to a point where it no longer dominates uncertainty estimates. The ice thickness grid is produced by averaging all thickness measurements within a 25 km radius of the centre of each grid cell, with all points receiving equal weighting. A radius of 25 km was chosen as it is sufficient to reduce the gaps between the ground tracks at lower latitudes and to suitably reduce the speckle error. Reducing the size of the averaging radius below 25 km does not reveal more detail in the maps, but does increase the noise. The uncertainty associated with each grid cell thickness is then calculated. To estimate the contribution of sea surface

height uncertainty to freeboard uncertainty, the variability of sea surface heights was examined over the 200 km interpolation length scale from October 2010-January 2015, and their standard deviation at orbit crossing points was 4 cm. As a conservative estimate, it is assumed that this variability remains correlated within the 200 km window of each freeboard calculation, and it is included as an additional source of uncertainty in the gridded thickness product. The freeboard error is then a combination of the 4 cm error due to spatially correlated errors in the interpolation of sea surface heights and that due to spatially uncorrelated errors in floe height measurement due to radar speckle. As the standard deviation on an individual freeboard measurement averages 9 cm Arctic-wide, and can be calculated through propagation of errors as the root-sum-square combination of the two sources of error [*Ku*, 1966], this leaves 8 cm for the floe height error. Although the number of floes heights averaged in each grid cell will be sufficient to reduce the 8 cm speckle error down to a negligible value, the 4 cm error in sea surface height will be reduced in the averaging only by the square root of the number of individual passes crossing the averaging window. When gridding monthly data this is typically 4 or more passes, resulting in a 2 cm freeboard uncertainty. This scales to ~20 cm thickness, or 11% of a typical growth season thickness of 1.8 m [*Tilling et al.*, 2015] for gridded monthly thicknesses.

3.5.2. Method

To calculate uncertainties in sea ice volume, the monthly rate of change of volume is calculated with respect to each parameter that has an associated error. For most parameters, its value is individually adjusted six times, at even increments, and the volume re-computed each time. The computed rates of change are then multiplied by the error in each parameter in question to estimate their partial contributions to the total volume error (Table 3.1). Taking snow depth as an example, the volume time series is computed seven times, changing the snow depth on each point-by-point freeboard measurement by 6 cm, 4 cm, 2 cm, 0 cm, +2 cm, +4 cm and +6 cm, to compute the monthly rate of change of volume per centimetre change in snow depth. This rate is multiplied by the monthly estimate of the snow depth error to estimate the contribution to error in sea ice volume.

To estimate the rate of change of sea ice volume with respect to sea ice extent, sea ice volume is recomputed using ice extent masks that use concentration data from the 10th day and the 20th day of each month, as well as the standard 15th day (Section 3.4.10). From these additional estimates, it is possible to compute the monthly rate of change of sea ice volume with respect to ice extent and hence assess the impact of this on volume error (Table 3.1). At 0.25% or less, the error in sea ice volume

associated with year-to-year uncertainties in sea ice extent is insignificant. At sub-annual timescales, it is important to consider seasonal biases in sea ice extent when charting variability. During the period of sea ice freeze up, sea ice extent could be consistently underestimated by as much as 1 million km^2 (http://nsidc.org/arcticseaice news/faq/#error_bars). Although the influence of this uncertainty on the volume error is not insignificant (Table 3.1), it does not affect year-to-year comparisons, and so it is not included in the error budget, which is designed to highlight uncertainties in inter-annual trends.

The contribution of sea ice concentration uncertainty to the total sea ice volume uncertainty is complicated, because the concentration data is used at two stages of sea ice processing – to discriminate between radar echoes returning from ice floes and open water, and to weight the volume calculation according to the density of leads within the sea ice pack. Therefore, the monthly rate of change of sea ice volume with respect to sea ice concentration is not calculated. Instead, the uncertainty in volume due to a 5% error in concentration is estimated. To do this the volume time series is recomputed twice for each month. In the first case the sea ice concentration at every point-by-point measurement location is lowered by 5% and any ice floes where the concentration falls below the threshold of 75% are removed from the processing. In the second case the sea ice concentration at every location is raised by 5%, but capped at 100%. The monthly volume error is estimated as half the difference between these two recomputed volume time series.

Finally, the monthly contributions to the volume error for all significant error sources are combined in a root-sum-square manner to arrive at an estimate of the total monthly sea ice volume error, using:

$$\sigma_V = \sqrt{\left(\frac{\partial V}{\partial h_s} \cdot \sigma_{h_s}\right)^2 + \left(\frac{\partial V}{\partial \rho_s} \cdot \sigma_{\rho_s}\right)^2 + \left(\frac{\partial V}{\partial \rho_i} \cdot \sigma_{\rho_i}\right)^2 + \left(\frac{\partial V}{\partial e_i} \cdot \sigma_{e_i}\right)^2 + {\sigma_{V_c}}^2} \quad (3.17)$$

where σ_V is the uncertainty in sea ice volume in a given month, V is sea ice volume, h_s is Arctic-wide snow depth, σ_{h_s} is the uncertainty in snow depth, ρ_s is Arctic-wide snow density, σ_{ρ_s} is the uncertainty in snow density, ρ_i is Arctic-wide ice density, σ_{ρ_i} is the uncertainty in sea ice density, e_i is sea ice extent, σ_{e_i} is the uncertainty in sea ice extent, and σ_{V_c} is the uncertainty in sea ice volume due to uncertainty in sea ice concentration. A term for the contribution of sea ice freeboard uncertainty is not included in Equation (3.17) as there are typically more than 1 million floe height measurements and 10,000 200 km arc segments included in each monthly volume

calculation, so the impact of both of these errors will be negligible on the monthly volume uncertainty. Year-to-year, uncertainties in Arctic-wide sea ice volume are typically about 13.5%, with small variations from month to month (Table 3.1).

Table 3.1: The sea ice volume error budget. The October and April error columns give a value for the Arctic-wide error, with respect to the mean value, for each significant error source. The October volume error and April volume error columns show the contribution of each source to the total estimated sea ice volume error. These are then combined in a root-sum-square manner to give an estimate of the total monthly sea ice volume error.

Factor	October error	October volume error	April error	April volume error
Snow Depth	23.3 %	10.3 %	19.5%	9.0 %
Snow Density	30.4 %	6.9 %	21.6%	5.5 %
FYI Density	0.8%	6.1 %	0.8%	6.7 %
MYI Density	0.9%	6.1 %	0.9%	6.7 %
Sea ice concentration	5.0 %	4.5 %	5.0 %	3.4 %
Inter-annual ice extent	0.4 %	0.25 %	0.2%	0.15 %
Seasonal ice extent	14.7%	8.4 %	0.4%	0.25 %
TOTAL (root-sum-square)		**14.5 %***		**13.0 %***

*Excluding errors in seasonal ice extent

Estimating local errors in sea ice thickness is complicated due to a lack of knowledge of the distances over which the contributing factors de-correlate. The main factors for which this information is important and lacking are snow depth, snow density, and sea ice density. In the sea ice volume error budget, their uncertainty is estimated over large scales as the standard deviation of monthly-averaged sparse field observations collected across the 9 million km^2 central Arctic region. However, it is assumed that these factors, and their variability, are influenced by synoptic-scale meteorology, so the length scale over which they are correlated is estimated to be comparable to that of a typical polar vortex – around 2000 km in diameter (http://www.cpc.ncep.noaa.gov/products/stratosphere/polar/ polar.shtml). Taking snow depth as an example, over areas that are large in comparison to this correlation scale, the variability of spatially averaged snowfall fluctuations will diminish in the ratio $1/\sqrt{n}$. Here, n is the effective number of independent values of accumulation sampled, and is

calculated as $n \sim A/(\pi 2000^2)$, where A is the area of the central Arctic (where field observations were collected) in square kilometres. If $n < 1$, it is set equal to 1. For the 9 million km^2 central Arctic region, over which the large scale sea ice volume and thickness uncertainty is estimated to be 13.5%, $n \sim 3$, leading to an uncertainty of 23%. Using this approach, and accounting additionally for short-scale correlated errors in freeboard associated with interpolating sea surface heights, it is estimated that the uncertainty in sea ice thickness increases to 25% at the 5 km scale of gridded monthly thicknesses.

A 25% local error in gridded monthly estimates of Arctic sea ice thickness derived from CryoSat-2 observations corresponds to an uncertainty of 45 cm for a typical thickness of 1.8 m. This uncertainty is consistent with the spread of differences relative to independent estimates acquired from airborne and ocean-based platforms (34 to 66 cm in Section 4.3). The uncertainty is at odds with a study by *Kern et al*. [2015] who suggest that using radar altimetry, the impact of sea ice density on sea ice thickness retrievals is as large as the impact of snow load, and that the difference in MYI and FYI density could alter sea ice thickness estimates by as much as 50 cm. However, the results of the *Kern at al.* [2015] study are not directly comparable to those presented here, as they were obtained by comparing satellite estimates of sea ice thickness with campaign data only – they did not develop a comprehensive uncertainty budget based on how incremental changes in each parameter impact on independent sea ice thickness retrievals. They also relied on altimeter data from the ERS and Envisat missions, which are likely to be associated with larger uncertainties than CryoSat-2 retrievals due to a reduction in data coverage and lack of measurements within the central Arctic. Both the *Kern at al.* [2015] method and the method outlined in this Section are only a first attempt to characterise local uncertainty in sea ice thickness. More detailed observations of snow depth, snow density, and sea ice density are required to establish the extent to which their variability impacts on the retrieval accuracy.

3.6. Conclusions

The fine spatial sampling and high-latitude orbit of ESA's CryoSat-2 mission provide unparalleled coverage of the Arctic Ocean, meaning that CryoSat-2 data can be used to produce sea ice thickness and volume estimates across the Northern Hemisphere. This chapter provides an end-to-end, comprehensive description of the data processing steps used to obtain these estimates, along with a detailed analysis of sources of error and uncertainty in the retrieval of sea ice thickness and volume from CryoSat-2.

3.7. Recent developments

Although the sea ice processing chain presented in this chapter has been under constant development at CPOM UCL since the early 1990s [*Laxon*, 1994], two core contributions were implemented for the first time during this study. Firstly, sea ice thickness and volume are now estimated across the Northern Hemisphere rather than being confined to the ICESat domain. Secondly, an error budget was developed for CryoSat-2 estimates of sea ice thickness and volume for the first time at CPOM UCL. These two developments are discussed in more detail in Sections 3.7.1 and 3.7.2 respectively.

3.7.1. Hemisphere-wide sea ice thickness and volume estimates

The first estimates of Arctic sea ice thickness and volume from CryoSat-2, which were produced at CPOM UCL by *Laxon et al*. [2013], were limited to the ICESat domain (Figure 1.8). Within the ICESat domain, climatology values of snow depth and density are constrained by *in situ* measurements. However, estimates of ice thickness and volume have now been extended across the Northern Hemisphere, due to the application of a mean climatological snow load for each month (Section 3.3.4). The efficacy of the mean climatological snow load for sea ice processing is discussed in detail in Appendix A.

3.7.2. Development of a CryoSat-2 error budget

The estimates of Arctic sea ice thickness and volume produced by *Laxon et al*. [2013] did not have an associated error budget, but quoted a value of 46 cm as the estimated error on gridded ice thicknesses. The value was calculated by *Giles et al*. [2007], who used ERS-2 radar altimeter data to conduct the only previous analysis of errors on sea ice thickness at CPOM UCL. The analysis was for May ice thicknesses only and assumed that the uncertainties of all contributing factors were uncorrelated from one measurement to the next. The uncertainty analysis presented in this chapter builds on the work of *Giles et al*. [2007] to estimate a percentage uncertainty value for grid cell sea ice thicknesses that can be applied throughout the growth season (Section 3.5). The analysis assumes a de-correlation length for contributing uncertainty factors (Section 3.5.2). To do this it was first necessary to compute monthly estimates of sea ice volume uncertainty (Section 3.5).

4. Arctic sea ice thickness and volume results from CryoSat-2

4.1. Introduction

There are now sufficient Baseline-B CryoSat-2 L1b data (Section 3.2) to produce estimates of Arctic sea ice thickness and volume from October 2010-January 2015, using the methods outlined in Chapter 3. These estimates cover four complete seasons of sea ice growth (October-April). The following chapter summarises the CryoSat-2 thickness and volume results (Section 4.2 and Section 4.4.1, respectively). The inter-annual variations in sea ice volume Arctic-wide and regionally are then discussed in more detail (Section 4.4.3). The chapter provides an evaluation of the CPOM UCL sea ice thickness product by comparison with a combination of airborne and buoy data (Section 4.3) and an evaluation of the volume product by comparison with model estimates (Section 4.5).

4.2. Arctic sea ice thickness results

Over the CryoSat-2 period, there have been marked variations in the thickness of sea ice in key sectors of the Arctic, both seasonally and inter-annually (Figure 4.1). During this period, the average thickness of Northern Hemisphere sea ice in spring (March/April) was 2.09 ± 0.28 m. In autumn (October/November), after the summer melting season, the average thickness reduced to 1.41 ± 0.19 m. While the thickest sea ice is in most years concentrated around the coast north of Greenland and Ellesmere Island, it often extends into the central Arctic – a region that has been, until now, beyond the limit of satellite altimetry. As a result, earlier estimates of satellite-derived Arctic-wide sea ice thickness (Section 1.6.2) from ERS-1 and -2 [*Laxon et al.*, 2003], Envisat [*Giles et al.*, 2008a], and ICESat [*Kwok et al.*, 2009], will have been biased low. For example, the CryoSat-2 thickness observations presented in this chapter show that below 81.5°N (the latitudinal limit of the ERS and Envisat satellites) sea ice is, on average, 13% thinner than Arctic-wide estimates. Regionally, the amount of sea ice in Fram Strait is quite variable, with the thickest ice appearing in spring 2012. There are also marked inter-annual variations in the spread of thick ice across the central Arctic region and the Beaufort Sea. Around the coast of Greenland and the Canadian Archipelago, the amount of thick ice in autumn (the period following the sea ice minimum extent) has also fluctuated from year to year.

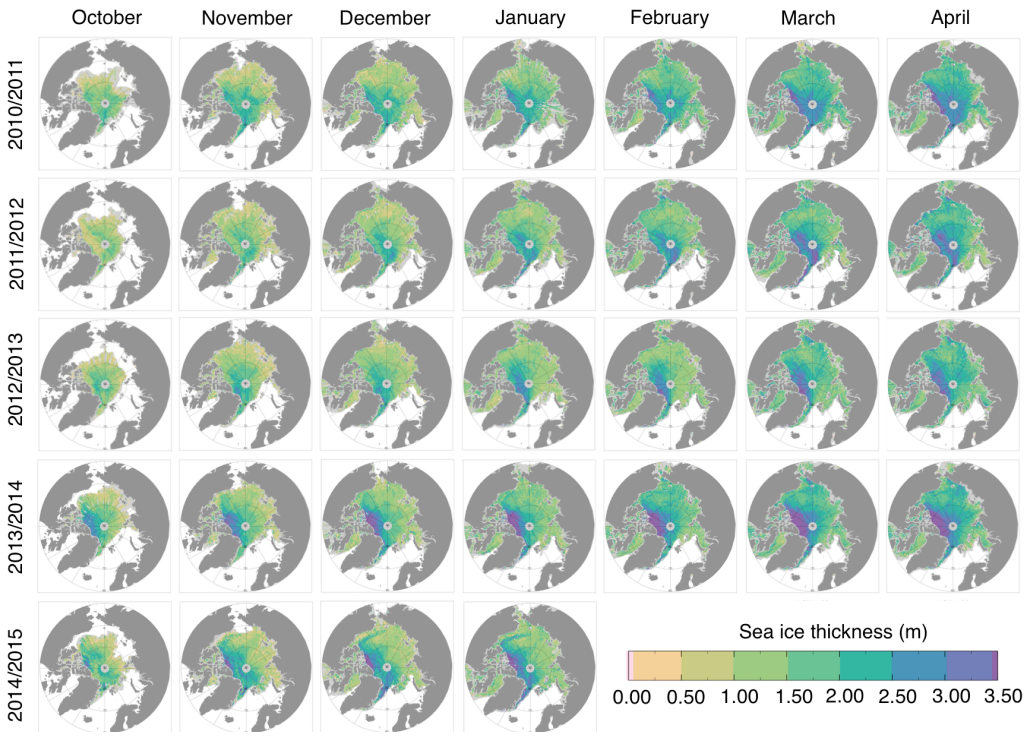

Figure 4.1: Northern Hemisphere sea ice thicknesses as measured by CryoSat-2, from 2010–2015. Thicknesses are shown at 50°N and above, where the majority of ice is located. The thickness maps shown were produced using Baseline-B CryoSat-2 data only. From February 2015, the Baseline-C processor was applied to the raw satellite data (Section 3.2).

4.3. Evaluation of the CryoSat-2 sea ice thickness product

To assess the accuracy of the CryoSat-2 measurements, they were compared to independent estimates of sea ice thickness and draft (ice thickness below the waterline) acquired from airborne and ocean-based platforms. For this, 772,090 estimates of sea ice thickness derived from NASA Operation IceBridge (OIB) airborne radar and laser altimeter measurements [*Kurtz et al.*, 2013] were used, along with 430 estimates of sea ice plus snow thickness derived from the ESA CryoSat-2 Validation Experiment (CryoVEx) airborne laser altimetry and electromagnetic sounding [*Haas et al.*, 2009], and 80 million estimates of sea ice draft derived from ULS buoy observations collected and made available by the BGEP based at WHOI (http://www.whoi.edu/beaufortgyre). The data used for the OIB comparison were collected over the period 2011-2014, 2011-2012 for the CryoVEx comparison, and 2010-2013 for the BGEP comparison. Although the OIB and CryoVEx measurements are only available in spring, they survey a range of ice thicknesses and type, mostly in the western Arctic (Figure 4.2a and b, respectively). The BGEP observations, in

contrast, are available year round, but sample a restricted distribution of ice as the moorings are fixed (Figure 4.2c). Like CryoSat-2 estimates of sea ice thickness, the OIB and CryoVEx estimates of sea ice thickness and sea ice plus snow thickness, respectively, are derived products. It is necessary to use these derived campaign products for evaluation due to the limited spatial and temporal coverage of *in situ* measurements of sea ice freeboard and thickness as well as ice density, snow depth, and snow density (Section 1.6.2). The campaign products have improved spatial resolution compared to satellite data,

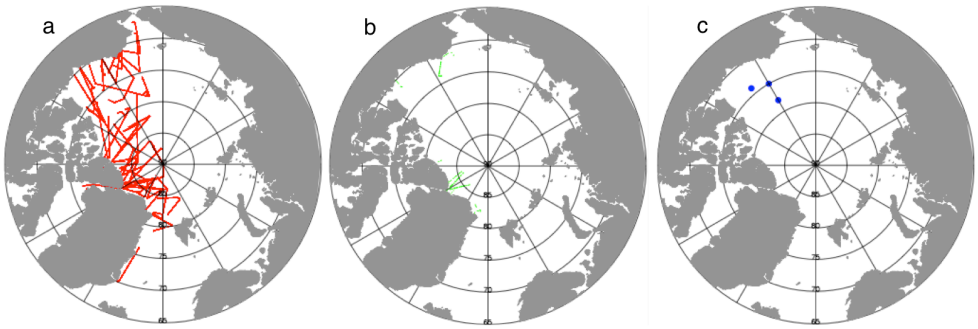

Figure 4.2: Locations of independent evaluation datasets. (a) NASA Operation IceBridge (OIB) airborne radar and laser altimeter measurements, (b) ESA CryoSat-2 Validation Experiment (CryoVEx) airborne laser altimetry and electromagnetic sounding measurements, and (c) ULS buoy observations collected as part of the Beaufort Gyre Exploration Project (BGEP).

To compare CryoSat-2 estimates to CryoVEX estimates of ice plus snow thickness, the mean climatological snow depth (Section 3.3.4) was applied to each CryoSat-2 thickness value. CryoSat-2 thicknesses were then compared to the OIB and CryoVEx data by gridding all datasets onto a 0.4° latitude by 4° longitude grid, which resulted in 1110 distinct OIB values and 64 CryoVEx values. To compare CryoSat-2 estimates to BGEP data, CryoSat-2 sea ice drafts were calculated by assuming that ice floes float in hydrostatic equilibrium [*Laxon et al.*, 2003] (Figure 3.11). Therefore CryoSat-2 sea ice drafts, d_i, were calculated using:

$$d_i = \frac{f_c \rho_i + h_s \rho_s}{\rho_w - \rho_i} \tag{4.1}$$

where f_c is the corrected sea ice freeboard measured by CryoSat-2, ρ_i is the sea ice density, h_s is the snow depth, ρ_s is the snow density and ρ_w is seawater density

(Section 3.4.9). Monthly averages of all CryoSat-2 draft estimates were then taken within 100 km of each ULS mooring and compared with monthly averages of ice draft obtained by each, resulting in 58 distinct values. Overall, the CryoSat-2 measurements agree with the OIB, CryoVEx, and BGEP measurements of sea ice thickness, sea ice plus snow thickness, and sea ice draft to within 0.5, 21.0, and 10.0 cm on average, respectively (Figure 4.3a-c).

To assess the overall bias in the CryoSat-2 observations, sea ice thickness was computed from the BGEP estimates of sea ice draft and the CryoVEx estimates of snow plus ice thickness, and these and the OIB estimates of thickness were compared to the satellite data (Figure 4.3d). BGEP sea ice thicknesses were calculated from BGEP draft by again assuming that ice floes float in hydrostatic equilibrium. Therefore BGEP sea ice thicknesses, h_i, were calculated using:

$$h_i = \frac{d_i \rho_w - h_s \rho_s}{\rho_i} \tag{4.2}$$

where d_i is the sea ice draft measured by BGEP ULS buoys, ρ_w is seawater density, h_s is the snow depth, ρ_s is the snow density and ρ_i is the sea ice density (Section 3.4.9). To convert CryoVEx ice plus snow thickness to ice thickness, the mean climatological snow depth (Section 3.3.4) was removed from each gridded CryoVEx measurement. When combined, the average difference between the OIB, CryoVEx, and BGEP estimates of ice thickness and those derived from CryoSat-2 is 2 mm. Given that the standard deviation in spring ice thickness derived from CryoSat-2 is 28 cm, it is concluded that there is no significant bias in the satellite data. The standard deviation between the CryoSat-2 and the OIB, CryoVEx, and BGEP estimates (66, 55, and 34 cm, respectively) are comparable to the estimated accuracy of the satellite (13 cm) [*Wingham et al.*, 2006] and independent (40 cm, 10 cm, and 10 cm, respectively) [*Farrell et al.*, 2012; *Haas et al.*, 2009; *Melling et al.*, 1995] measurements themselves, and will be dominated by spatial variations in thickness at length scales smaller than the satellite footprint. The absolute differences between ice thickness estimates derived from the satellite and independent observations may arise through uncertainties in either dataset.

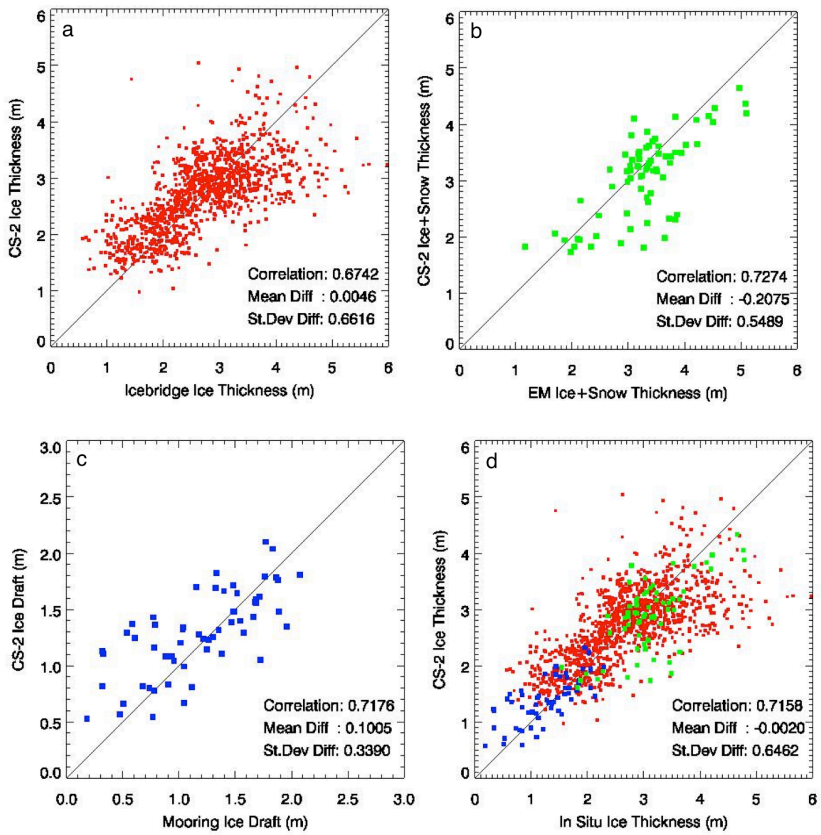

Figure 4.3: Evaluation of the CryoSat-2 sea ice product. (a) Comparison of Operation IceBridge and CryoSat-2 thickness for March and April 2011-2014. (b) Comparison of CryoVEx and CryoSat-2 ice plus snow thickness for March and April 2011 and 2012. (c) Comparison of monthly average ice draft from the Beaufort Gyre Exploration Project upward looking sonar buoys with monthly average CryoSat-2 ice draft from within 100 km of each mooring, for October-April 2010/11-2012/13. (d) Comparison of ice thicknesses estimated from all three in situ datasets and from CryoSat-2. Values for the mean difference and standard deviation of the difference are expressed in metres.

4.4. Arctic sea ice volume results

4.4.1. Summary of Arctic sea ice volume results

There have been clear seasonal and inter-annual variations in the volume of Arctic-wide sea ice over the CryoSat-2 period (Figure 4.4 and Table 4.1). For all years, the total sea ice volume increases each month over a given growth season from October to March, and drops slightly in April due to the onset of summer melt. This is also true for the volume of FYI, except in 2012 when the March and April volume were similar. There is, however, more variation in MYI volume growth. There is still a general trend of increasing MYI volume over each growth season but this is punctuated with more variability from month-to-month. The inter-annual variations

in Arctic-wide sea ice volume for FYI, MYI and total ice cover will be discussed in detail in Section 4.4.3. The uncertainties on FYI, MYI and total ice volume increase through the growth season due to an increase in the depth uncertainties. The climatology [*Warren et al.*, [1999] used for snow depth (Section 3.3.4) and its associated uncertainties (Section 3.5.1) provides, as an error estimate, the standard deviation of snow depth anomalies in each calendar month, which increases as snow depth increases. These errors are likely to be an overestimate, as the anomalies were calculated relative to measurements from only a few (typically 2) stations (Section 3.5.1 and *Warren et al.* [1999]). Sea ice volume has also been computed for fixed oceanographic basins (Figure 3.12), so that volume changes can be documented in regions of oceanographic interest (Table 4.2). It is crucial to consider the influence of regional variations on sea ice volume when considering Arctic-wide inter-annual variability, and this is also discussed in Section 4.4.3.

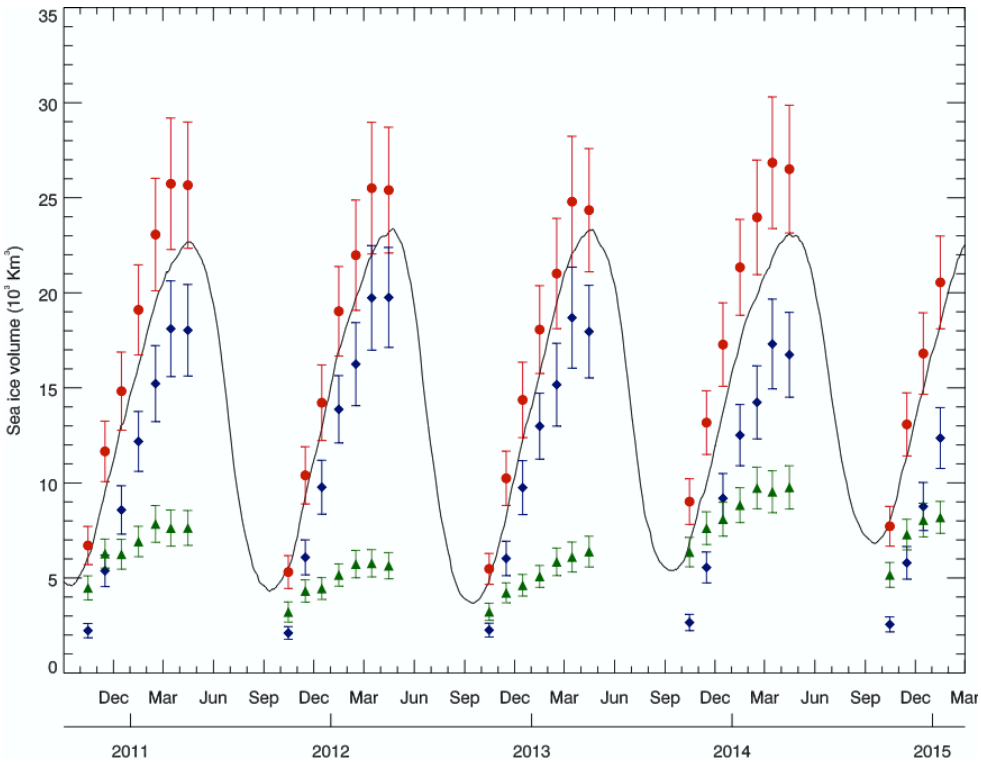

Figure 4.4: Cryosat-2 estimates of total (red stars), first-year (blue diamonds) and multi-year (green triangles) sea ice volume. Also shown are model estimates of volume from the Pan-Arctic Ice-Ocean Modelling and Assimilation System (PIOMAS) (black line). The estimation of volume uncertainties is described in Section 3.5.

Table 4.1: Average CryoSat-2 Northern Hemisphere sea ice volume (10^3 km^3) for autumn (October/November) 2010-2014 and spring (March/April) 2011-2014.

Year	Volume (MYI)		Volume (FYI)		Volume (total)	
	Autumn (Oct/Nov)	Spring (Mar/Apr)	Autumn (Oct/Nov)	Spring (Mar/Apr)	Autumn (Oct/Nov)	Spring (Mar/Apr)
2010/11	5.34 ± 0.69	7.64 ± 0.94	3.69 ± 0.59	17.99 ± 2.44	9.03 ± 1.28	25.63 ± 3.37
2011/12	3.75 ± 0.56	5.72 ± 0.71	4.11 ± 0.63	19.57 ± 2.66	7.86 ± 1.19	25.29 ± 3.36
2012/13	3.70 ± 0.48	6.23 ± 0.80	4.05 ± 0.62	18.20 ± 2.53	7.75 ± 1.10	24.43 ± 3.32
2013/14	6.95 ± 0.82	9.63 ± 1.12	3.99 ± 0.61	16.96 ± 2.29	10.94 ± 1.43	26.59 ± 3.41
2014/15	6.18 ± 0.73	-	4.08 ± 0.62	-	10.26 ± 1.34	-

Table 4.2: Regional changes in sea ice volume from CryoSat-2. The mean ice volume (10^3 km^3) and rate of volume change (km^3 $year^{-1}$) are given for autumn (October/November) 2010-2014 and spring (March/April) 2011-2014, for 16 Arctic Ocean regions (see Figure 3.12 for region locations). For each region, the ocean-covered area is given in 10^3 km^2 and uncertainties on the mean volume and rate of volume change are the interannual variation.

Region	Area	Autumn (Oct/Nov)		Spring (Mar/Apr)	
		Mean volume	dV/dt	Mean volume	dV/dt
Amerasian Basin (1)	2570	3.34 ± 0.63	0.30 ± 0.15	5.99 ± 0.50	0.28 ± 0.19
Eurasian Basin (2)	2090	2.64 ± 0.31	0.01 ± 0.11	4.57 ± 0.36	-0.13 ± 0.18
Canadian Archipelago & Northwest Passage (3)	1340	1.09 ± 0.27	0.11 ± 0.12	2.58 ± 0.25	0.05 ± 0.13
Hudson Bay (4)	1250	0.04 ± 0.03	0.01 ± 0.01	1.96 ± 0.06	0.04 ± 0.02
Baffin Bay (5)	940	0.18 ± 0.04	0.00 ± 0.01	1.19 ± 0.03	0.00 ± 0.02
Greenland Sea (6)	730	0.44 ± 0.06	0.02 ± 0.02	0.83 ± 0.10	-0.03 ± 0.05
Iceland Sea (7)	510	0.05 ± 0.02	0.00 ± 0.01	0.31 ± 0.03	0.00 ± 0.02
Barents Sea (8)	1500	0.10 ± 0.13	0.05 ± 0.05	0.72 ± 0.22	0.01 ± 0.12
Kara Sea (9)	860	0.26 ± 0.11	0.03 ± 0.04	1.14 ± 0.13	0.00 ± 0.07
Siberian Shelf Seas (10)	2190	1.02 ± 0.20	0.02 ± 0.07	3.71 ± 0.12	0.06 ± 0.05
6 other regions	8370	0.00 ± 0.00	0.00 ± 0.00	2.44 ± 0.42	0.08 ± 0.23
Total	**22 350**	**9.16 ± 1.8**	**0.55 ± 0.54**	**25.44 ± 2.22**	**0.20 ± 0.47**

4.4.2. Arctic sea ice growth rates

CryoSat-2 sea ice volume estimates can be used to quantify the rate of sea ice growth from autumn to winter (Table 4.3), which influences peak annual ice thickness and volume [*Holland et al.*, 2001] and, in turn, affects the Arctic heat budget by moderating heat exchange between the ocean and the atmosphere (Section 1.3.1). The rate of autumn-to-winter sea ice growth (the period of maximum volume increase) during each calendar year across the entire Arctic was computed by fitting a linear trend to volume measurements acquired between October and January inclusive. The average rate of growth was 4.22 km^3 $month^{-1}$, with only small (4% standard deviation) variations from year to year. The rate of growth of FYI and MYI was also computed separately, and these showed markedly larger temporal variability (8% and 23% standard deviation, respectively) reflecting interannual transitions between each class of ice cover. It is noted that the growth rate from October 2013-January 2014 was larger than the 2010-2011 equivalent, despite the total volume increase over the growth season being smaller. This is possible when the sea ice cover thickens rapidly in the first few months of the growth season and reaches a state where the under-ice surface is sufficiently insulated from the cool atmosphere to reduce the rate of congelation growth, where seawater beneath the ice freezes to the under-ice surface (Section 1.2.2), for the remainder of the growth season.

Table 4.3: CryoSat-2 Arctic sea ice volume growth. Growth rates (km^3/month) are given for autumn to winter (October-January) for four seasons of ice growth, for first-year ice (FYI), multi-year ice (MYI) and the total ice volume. Also given are values for the total volume growth (km^3) over the whole growth season (October-April).

Year	October-January growth rate			Growth season volume increase
	FYI	MYI	Total	
2010/11	3.32	0.72	4.04	19.14
2011/12	3.89	0.60	4.50	19.92
2012/13	3.58	0.60	4.19	18.91
2013/14	3.27	0.81	4.08	17.55
2014/15	3.27	1.01	4.28	-
Mean	**3.47**	**0.75**	**4.22**	**18.88**
Std. Deviation	**0.27**	**0.17**	**0.18**	**0.99**

4.4.3. Inter-annual variations in sea ice volume

Since 2010, there have been large inter-annual fluctuations in the amount of Northern Hemisphere sea ice (Figure 4.3 and Table 4.1). MYI is the most variable ice type and, between 2010 and 2012, a 31% (1,640 km^3) decline in its autumn volume was recorded, followed by an 88% (3,251 km^3) increase in 2013 and an 11% (771 km^3) decrease in 2014. These changes impact on the total autumn sea ice volume, which declined by 14% (1,279 km^3) between 2010 and 2012, increased by 41% (3,184 km^3) in 2013, and decreased by just 6% (673 km^3) in 2014. The peak autumn volume in 2013 manifested as a thick ice cover in the MYI region north of Greenland and Ellesmere Island (Figure 4.1), with ice being 21% thicker, on average, than the five year mean. The volume of autumn FYI is much less variable. Inter-annual variations in hemisphere-wide volume in spring are less significant than in autumn for all ice types – there was a 9% volume increase in spring 2014, following the autumn 2013 increase, but this was not significant. At the scale of oceanographic basins (Figure 3.12), only the Amerasian basin, which encompasses the Beaufort Sea, exhibits a significant trend in sea ice volume over the CryoSat-2 period (Table 4.3). The 40% growth of ice in this sector in autumn 2013 contributed significantly to the overall increase in Arctic sea ice volume. The driving factors behind this increase are explored in the following chapter – Chapter 5.

4.5. Evaluation of the CryoSat-2 sea ice volume product

The PIOMAS model [*Zhang and Rothrock*, 2003] provides an alternative approach to estimating regional trends in volume, as it assimilates sea ice data by including measurements of NRT sea ice concentration and drift (Section 1.5.2). The PIOMAS volume output is compared to CryoSat-2 estimates in Figure 4.3. At 4.22 km^3 $month^{-1}$, the average October-January sea ice growth rate during the CryoSat-2 measurement period is 15% higher than estimates derived from PIOMAS, leading to springtime sea ice volumes that are 12% higher. The difference between the PIOMAS and CryoSat-2 domains, which are truncated at 45°N and 40°N, respectively, cannot explain the shortfall, because the volume of sea ice in the regions omitted by PIOMAS (parts of the Sea of Okhotsk and the Gulf of St Lawrence) are too small (< 0.15% of total Arctic sea ice, on average). Although PIOMAS does reproduce, qualitatively, many aspects of the observed variability, including the seasonal progression and the step increases in sea ice volume recorded in the autumns of 2013 and 2014, the discrepancy in growth

rates, springtime volume, and inter-annual springtime volume variability all point to a need for further investigation.

4.6. The relationship between Arctic sea ice area, thickness and volume

The monthly area, mean thickness and volume of Arctic sea ice from CryoSat-2 are shown in Figure 4.4, for FYI, MYI, and total ice. For all years, the total ice area increases month-by-month over the growth season from October to March, and drops slightly in April due to the onset of summer melt. The pattern is the same for the area of FYI, although the MYI area experiences a slight decrease over the growth season (Figure 4.5a). This is because the area of MYI in the Arctic is dependent on two key processes. The first is the ageing of FYI to MYI and the second is ice export out of the high Arctic to more southern regions [*Kwok*, 2004; *Kwok et al.*, 2013]. The ageing of sea ice dominates at the start of the sea ice growth season, but sea ice export continues throughout the year. Therefore, the MYI area experiences a continuous decreases after October/November time [*Ye et al.*, 2016]. In contrast to the ice area, the total ice, FYI and MYI mean thickness (Figure 4.5b) increase from March to April each year, as Arctic sea ice continues to thicken through congelation growth (Section 1.2.2) after it has reached its maximum annual area. Dynamics can also influence the area and mean thickness of the sea ice pack. Net thinning of the sea ice cover can occur due to the divergence of sea ice, but this in turn provides new areas of open water for FYI growth. Net thickening of the ice pack can occur through ice convergence, without any thermodynamic growth [*Kwok and Cunningham*, 2015]. Despite all ice types thickening from March to April, the total and FYI volume follow that of total and FYI area – they increase each month over a given growth season from October to March, and drop slightly in April. The volume of MYI also increases over the growth season, although there is more variation from month to month. This suggests that seasonally, the total ice area and volume of sea ice in the Arctic are dominated by temperature-driven fluctuations in the FYI area and volume and start to decrease at the onset of melt and the loss of the weakest seasonal FYI at the sea ice edge.

Inter-annually, changes in the MYI cover have a significant impact on the total amount of Arctic sea ice (a summary of the inter-annual variations in the volume of FYI, MYI and total ice is provided in Table 4.1). For example, the minimum total ice area (Figure 4.5a) and volume (Figure 4.5c) over the CryoSat-2 period were observed in autumn 2012, which coincided with the minimum MYI area and volume. Despite these record lows in area and volume, the mean thickness of total and MYI reached their minimum in autumn 2011 (Figure 4.5b). This shows that, in autumn 2012 at least, the low area of the Arctic sea ice cover dominated the sea ice volume. After the record low total ice

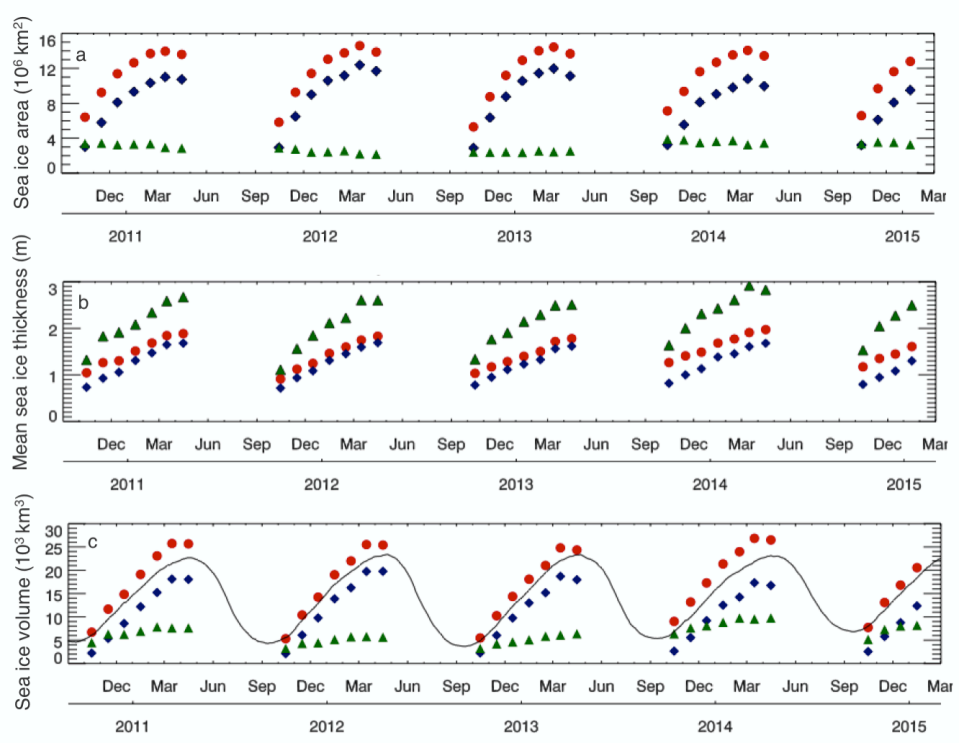

Figure 4.5: Estimates of total (red stars), first-year (blue diamonds) and multi-year (green triangles) sea ice parameters. (a) Sea ice area output by the CPOM UCL sea ice processor. The area calculation is described in Section 3.4.2 and Section 3.4.10). (b) CryoSat-2 estimates of mean sea ice thickness. (c) CryoSat-2 estimates of sea ice volume. Also shown are model estimates of volume from the Pan-Arctic Ice-Ocean Modelling and Assimilation System (PIOMAS) (black line). This is equivalent to Figure 4.3 and is replicated here for comparison with area and mean thickness.

volume in autumn 2012, the volume at the end of the growth season, in spring 2013, was still the lowest of the CryoSat-2 record. This coincided with the lowest spring MYI volume, and the growth of FYI was not enough to compensate for the MYI deficit. The importance of inter-annual changes in MYI on the total ice cover was also demonstrated in 2013, which saw the highest autumn area and volume of total ice. This corresponded to a peak in area, mean thickness and volume of MYI. The high volume of autumn 2013 remained throughout the growth season, and the spring of 2014 had the highest total ice volume of the CryoSat-2 record, which was associated with a peak in area, mean thickness and volume of MYI. The total ice area in spring 2014 was actually the lowest over the CryoSat-2 period, but was compensated by a peak in total ice mean thickness. This demonstrates that a decreasing ice area does not necessarily result in a proportionate decrease in ice volume, and so thickness information is required to assess the true state of the sea ice pack.

4.7. Conclusions

In this chapter, CryoSat-2 data have been used to produce the first estimates of sea ice thickness and volume across the entire Northern Hemisphere. CryoSat-2 estimates of ice thickness agree with independent estimates of thickness and draft derived from springtime airborne laser and electromagnetic sensor campaigns and year-round ULS observations to within 2 mm, on average. Sea ice volume estimates from CryoSat-2 display, qualitatively, many aspects of the observed variability in volume from the PIOMAS model, including seasonal progression and the step increase in sea ice volume recorded in the autumn of 2013. However, the discrepancy in growth rates, springtime volume, and inter-annual springtime volume variability between the two approaches requires further investigation. CryoSat-2 data have also been used to assess the inter-annual variability in Northern Hemisphere sea ice volume. Inter-annual variations in hemisphere-wide volume in autumn are more significant than in spring, for FYI, MYI and total ice. Between autumn 2010 and 2012, there was a 14% reduction in total Arctic sea ice volume, in keeping with the long-term decline in extent. However, 33% and 25% more ice was observed in autumn 2013 and 2014, respectively, relative to the 2010-2012 seasonal mean, offsetting earlier losses. The peak autumn volume in 2013 manifested as a thicker than average sea ice cover in the MYI region north of Greenland and Ellesmere Island. The drivers of this variability form the basis of the following chapter.

5. Understanding the drivers of Arctic sea ice variability

5.1. Introduction

This chapter examines the potential drivers of inter-annual variability in Arctic sea ice volume, as measured by CryoSat-2. The variability was discussed in detail in Section 4.4.3, and summarised in Section 4.7. The following chapter introduces a method to identify the cause of the variability by using ERA-Interim reanalysis data [*Dee et al.*, 2011] to investigate the influence of fluctuations in snow loading, wind-driven ice drift, and ice melting on sea ice volume (Section 5.3). The chapter concludes that the increase in autumn sea ice volume observed in 2013 was associated with a 5% drop in the number of days on which melting occurred. This corresponds to conditions more typical of the late 1990's. The sharp increase in sea ice volume after just one cool summer indicates that Arctic sea ice may be more resilient than has been previously considered, but equally demonstrates the ability of Arctic sea ice to respond rapidly to a changing environment (Sections 5.4 and 5.5). The work presented in this chapter was the subject of a Nature Geoscience paper published by *Tilling et al.* [2015] titled "Increased Arctic sea ice volume after anomalously low melting in 2013".

5.2. Background and approach

The inter-annual variability in sea ice volume observed by CryoSat-2 could be an artefact of the data processing, or of real changes caused by physical drivers. For example, the changes could be a consequence of applying a climatological snow depth (Section 3.3.4) in the ice thickness calculation (Equation (3.14)) that does not vary from year-to-year. In reality, the snow depth on Arctic sea ice varies inter-annually [*Warren et al.*, 1999; *Webster et al.*, 2014]. This is an important consideration, as an overestimate (underestimate) of snow depth for a given month will result in an overestimate (underestimate) of sea ice thickness, according to Equation (3.14). Physically, variations in sea ice volume could be related to dynamic or thermodynamic forcing, or a combination of both.

In 2003, *Laxon et al.* [2003] used ERS-1 and ERS-2 data to show that there was a high interannual variability in mean Arctic sea ice thickness from 1993-2001. They concluded that the dominant control on this variability was summer ice melt and not wind or ocean forcing. Following this, *Kwok et al.* [2009] observed a thinning and volume loss of the Arctic sea ice cover over 2003-2008 from ICESat, which they attributed to a combination of the export of thick MYI through the Fram Strait and other

passages into peripheral seas, ice melt, and later formation of the seasonal ice cover. It has also been suggested by *Kwok et al*. [2015] that the increase in Arctic sea ice volume in autumn 2013 compared to previous years over the CryoSat-2 observation period was a consequence of cooler Arctic temperatures in summer 2013 and large-scale ice convergence west of the Canadian Archipelago due to wind-driven onshore drift. However, none of these previous observational studies have been supported by statistical analysis.

In this study ERA-Interim reanalysis data [*Dee et al.*, 2011] were used to investigate the factors that might influence sea ice volume. The aim was to identify whether there was a dominating driver of the observed inter-annual variability, by applying a statistical approach. ERA-Interim reanalysis data were chosen over alternative climate reanalyses as they have been found to be more consistent with independent observations in the Arctic, and specifically for the parameters required for this study [*R Lindsay et al*., 2014]. The reanalysis data were used to calculate the mean autumn snow load, annual wind convergence (a proxy for wind-driven ice convergence), and the annual number of melting degree days ($M_{DD;}$ a proxy for ice melt) [*Kwok*, 2007] in the Amerasian and Eurasian basins (Figure 3.12). It was then possible to investigate the relationship between each parameter and the volume of sea ice in the Amerasian and Eurasian basins at the start of the ice growth season, in autumn, when there is most variability. The focus was on the Amerasian and Eurasian basins because they contain the majority of all Northern Hemisphere sea ice – 65% and 42% in autumn and spring, respectively (Table 4.2). They comprise the main region of near-persistent sea ice cover (Figure 5.1) and can therefore be used to investigate influences on volume throughout the sea ice growth season. The impact of ocean-driven changes on sea ice dynamics and volume changes was not assessed, as contemporaneous observations of sea ice drift were not available.

5.3. Determining climate forcing from ERA-Interim reanalysis data

5.3.1. Snow load

A time-varying snow load was derived from the ERA-Interim climate reanalyses, to provide alternative estimates of the snow load on Arctic sea ice in the Amerasian and Eurasian basins, from October 2010 to November 2014. The precipitation (P) and evaporation (E) fields from the reanalysis data were used to calculate monthly values of snow load. Both fields are provided on a 0.75 by 0.75 degree grid in latitude and longitude and contain daily estimates of P and E in mm of water equivalent. Daily values

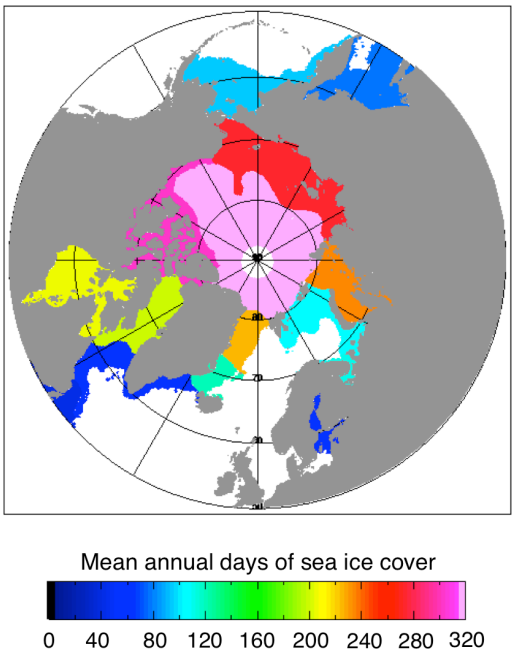

Figure 5.1: Regional variation in days of sea ice cover. The map shows mean annual days of sea ice cover from August 1st-July 31st for each Arctic Ocean region (see Figure 3.12 for region locations), over the CryoSat-2 period. The Amerasian and Eurasian basins have been combined. A location is considered ice covered if the sea ice concentration is above 15%.

of snow load were calculated by subtracting ERA-interim E from P. As P and E are provided in mm of water equivalent, snow load in this context refers to the snow water equivalent (SWE), which is the amount of water contained within the snowpack. It can be thought of as the depth of water that would result if the snowpack were melted. Mathematically, the time-varying SWE can be written as:

$$\mathrm{SWE} = \frac{h_s \rho_s}{\rho_w} \tag{5.1}$$

where h_s is the time-varying snow depth, ρ_s is snow density, and ρ_w is seawater density. Equation (5.1) shows that the time-varying snow load derived from ERA-Interim data is proportional to the time-varying snow depth, as throughout this thesis snow density is taken from a monthly climatology (Section 3.3.4) and seawater density is a constant (Section 3.4.9). Daily snow load values were accumulated (temporally integrated) over each month to produce maps of net monthly snow accumulation. The total snow load for each month was then estimated by assuming that all snow diminishes by August 1st each year, so that the snow load is zero on that date. This eliminates the need to adjust the snow load over FYI, as is done when employing a

climatological snow load (Section 3.3.4). Therefore the total snow load by the end of each month was computed by accumulating monthly snow loads beginning from the preceding August, in each grid cell. Finally, monthly average values of the snow load were produced over the Amerasian and Eurasian basins combined. A time-varying snow load is relatively simple to produce in the Amerasian and Eurasian basins as sea ice persistence is high (Figure 5.1) and the accumulation calculation can be simplified by assuming that a year-round ice cover is present. The snow load developed does not account for snow drift, which is likely to affect the snow load during persistent wind conditions. However, it is considered sufficient for its propose in this instance – to assess whether over- or under-estimating snow load when using a fixed monthly climatology significantly influences sea ice volume estimates.

5.3.2. Wind convergence

To compute annual wind convergence into the Amerasian and Eurasian basins, it is first necessary to calculate the wind divergence, using surface wind field components from the ERA dataset. The ERA wind field is resolved into U and V components, where U is the component in the x-direction (eastward) and V is the component in the y-direction (northward). The wind components are provided on a 0.75 by 0.75 degree grid in latitude and longitude and contain daily values of U and V, in ms^{-1}. The daily values were averaged over each month to give maps of monthly mean U and V wind speeds. The U and V wind speeds were then resampled on to a 25 km by 25 km polar stereographic grid so that grid cells were evenly spaced for the divergence calculation. On the new polar stereographic grid the x-axis points south down the 90°E longitude line and the y-axis points south down the 180°E longitude line. So, if $\boldsymbol{w}(x,y)$ is the wind field and $\boldsymbol{i}$ and $\boldsymbol{j}$ are unit vectors in the x and y directions:

$$\boldsymbol{w}(x,y) = U(x,y)\boldsymbol{i} + V(x,y)\boldsymbol{j} \tag{5.2}$$

and the wind divergence at each location in the grid is:

$$\boldsymbol{\nabla} \cdot \boldsymbol{w} = \frac{\partial U}{\partial x} + \frac{\partial V}{\partial y} \tag{5.3}$$

The partial derivatives were computed numerically. Where the wind components diverge the divergence will be positive and where they converge it will be negative. For comparison with CryoSat-2 autumn volume data, the wind divergence in each grid cell was accumulated from November 1st of the previous autumn to November 1st of the autumn under consideration, to get a value of annual wind divergence. To compute the

mean convergence of the wind components over the Amerasian and Eurasian basins negative values of $\nabla . \boldsymbol{w}$ were considered, then area averaged. The magnitude of the result is the convergence.

Wind convergence was used as a proxy for sea ice convergence into the Amerasian and Eurasian basins, as unlike sea ice drift data, ERA-interim wind fields were available daily and year-round throughout the CryoSat-2 period. This was not so for daily sea ice motion data at the time that the study was performed. However, since March 2016, NSIDC have hosted the NASA-produced Polar Pathfinder sea ice motion vector dataset [*Tschudi et al.*, 2016]. The data are derived from a number of passive microwave and scatterometer satellite instruments and buoy data, and are provided year-round at daily resolution. Similarly, OSI SAF have started to provide preliminary sea ice motion data with year-round coverage at 2-day resolution, which are derived from a combination of passive microwave and scatterometer satellite instruments [*Lavergne*, 2015]. The OSI SAF data are currently only available from January 2013 and would need to be available from November 2009 for use with this study.

To assess the validity of wind as a proxy for ice drift, ERA-Interim wind fields were compared with sea ice drift from drifting buoy data obtained from the International Arctic Buoy Program (IABP) at the University of Washington (available via ftp at ftp://iabp.apl.washington.edu/pub/IABP/). To assess the similarities between wind and buoy direction of motion, the mean motion of each active buoy was computed by creating a vector joining its start and finishing location for each month of the CryoSat-2 period. The buoy motions were compared with the monthly mean ERA-Interim wind vector at each buoy start location (e.g. Figure 5.2a). A good agreement was found in the Amerasian and Eurasian basins in each month that buoy data was available. Next a crossplot was produced to compare the magnitude of buoy motion with the magnitude of the wind field at each monthly buoy location, to assess the similarities in the magnitude of wind and buoy displacement (Figure 5.2b). This showed that wind velocity (km hour^{-1}) and buoy displacement (km) are correlated ($r^2 = 0.60$).

The correlation found between wind velocity and buoy displacement echoes the work of Thorndike and Colony [*Thorndike and Colony*, 1982], who found that on monthly time scales and in all seasons, more than 70% of the variance of the ice velocity in the central Arctic Ocean was explained by the geostrophic wind. The remainder of the variance was assigned to internal ice stress and the influence of ocean currents, which could also explain some of the remaining variance in this study. They also suggest that geostrophic winds have less of an impact on ice motion within about 400 km of coastal regions, due to internal ice stresses opposing the ice velocity. More

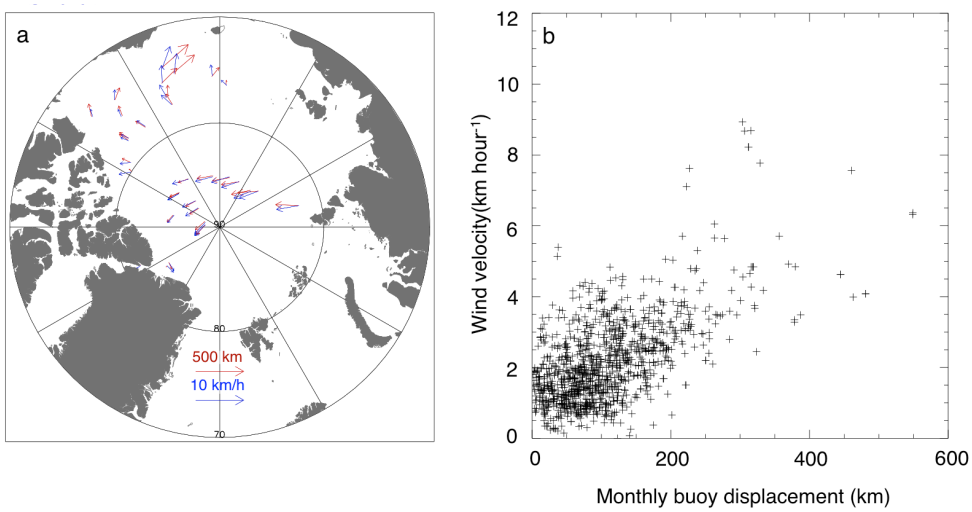

Figure 5.2: An example comparison of ERA-Interim wind field data with sea ice drift data from the International Arctic Buoy Program. (a) Vectors of monthly buoy displacement (in km; red arrows) and corresponding mean monthly wind velocity (in km hour^{-1}; blue arrows) for December 2011. (b) The relationship between the magnitude of wind velocity and buoy displacement at each monthly buoy location; r^2 = 0.60.

recently, the variability in Arctic sea ice drift speed has been attributed to changes in the ice concentration [*Olason and Notz*, 2014], and the ice thickness and strength [*Kwok et al.*, 2013]. By eye, the differences between the wind velocity and buoy displacement data used in this study are greatest in the western Beaufort Sea and approaching the Bering Strait, where the sea ice cover is more seasonal. Hence the spread between wind velocity and buoy displacement in these regions may be explained by increased variability in the ice concentration and strength (which will influence momentum transfer between the atmosphere and sea ice [*Tsamados et al.*, 2014]), in addition to internal ice stress and the influence of ocean currents. On the scale of the Amerasian and Eurasian basins it is expected that changes in sea ice thickness due to ice motion will be primarily driven by geostrophic winds, with ocean currents having a more modest impact on changes in ice thickness.

5.3.3. Melting degree days

Melting degree days (M_{DD}) defines the number of days that experienced a daily mean temperature above 0°C, for a specified time frame. In this study, M_{DD} was used as a proxy for ice melt. Annual M_{DD} were calculated using the 2m-temperature dataset from ERA-Interim reanalysis data. The dataset is provided on a 0.75 by 0.75 degree grid in latitude and longitude and contains daily values of near surface (2m from the surface)

temperature in K, which were converted to °C. For each grid cell, M_{DD} is the collective sum of the daily air temperatures above 0°C, for a specified time frame. For comparison with CryoSat-2 autumn volume data, the M_{DD} in each grid cell was calculated from November 1st of the previous autumn to November 1st of the autumn under consideration. M_{DD} was then spatially averaged over the Amerasian and Eurasian basins. It is noted that M_{DD} is a variable of atmospheric origin and that temperature and melt of the sea ice surface will depend on the heat-transfer mechanisms through the snow pack. However, M_{DD} has previously displayed a significant correlation with MYI area in the Arctic at the end of summer [*Kwok*, 2007], which suggests that it acts as a reasonable proxy for ice melt.

5.4. Relationship between changes in sea ice volume and climate forcing

If the observed inter-annual variations in autumn sea ice volume were a consequence of applying a climatological snow depth that does not vary from year-to-year (Section 3.3.4) in the ice thickness calculation (Equation (3.14)) then a negative correlation would be expected between the time-varying autumn snow load (Section 5.3.1) and autumn sea ice volume in the Amerasian and Eurasian basins. This is because an overestimate of snow depth from the climatology will result in an overestimate of sea ice thickness and subsequent volume (Section 5.2 and Equation (3.14)), leading to an overestimate of volume in months where the true (time-varying) snow accumulation is less than that assumed (and vice versa). However, a comparison between the time-varying autumn snow load and autumn sea ice volume in the Amerasian and Eurasian basins shows that, although negative, the correlation is very weak (r^2 = 0.05; Figure 5.3), suggesting that inter-annual variations in sea ice volume are driven by other factors.

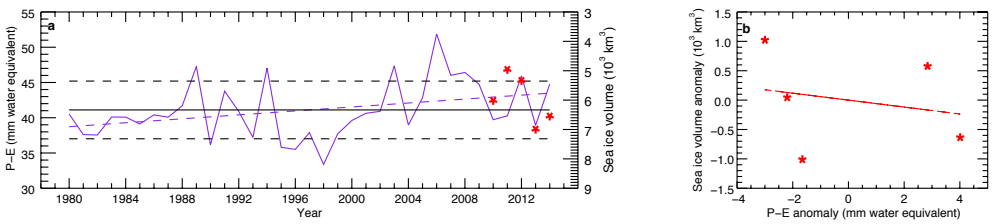

Figure 5.3: The relationship between autumn sea ice volume in the Amerasian and Eurasian basins, and snow load derived from ERA-Interim reanalysis data. (a) Time series of autumn snow load in the Amerasian and Eurasian basins for 1980-2014 (solid purple line), and CryoSat-2 autumn ice volume for 2010-2014 (red stars). The 34-year snow load mean (solid black line) and standard deviation (dashed black line) are shown. (b) The relationship between anomalies of CryoSat-2 ice volume and autumn snow load. The correlation is very weak (r^2 = 0.05).

A comparison of the annual wind convergence with autumn sea ice volume in the combined basins returns a weak correlation (r^2 = 0.38; Figure 5.4). However, there is a strong correlation between autumn sea ice volume and M_{DD} in the combined basins (r^2 = 0.73; Figure 5.5), which implies that Arctic sea ice volume come autumn is strongly affected by the degree of melting over the summer. Although other environmental factors may have influenced Arctic sea ice volume in the region, such as ocean-driven changes in dynamics, the analysis presented here suggests that thermodynamics play an important role. This is in agreement with the work published by *Laxon et al*. [2003] who concluded that inter-annual variations in mean winter sea ice thickness from 1993-2001 were dominated by summer melt (Section 5.2).

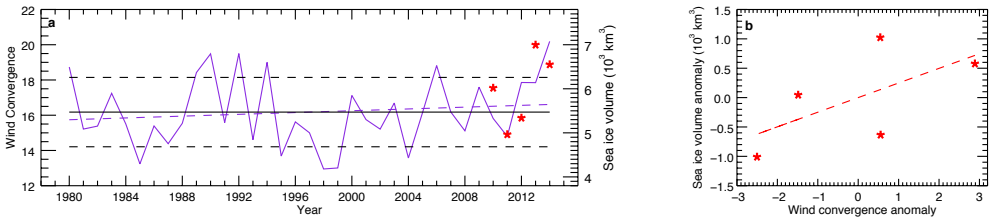

Figure 5.4: The relationship between autumn sea ice volume in the Amerasian and Eurasian basins, and annual wind convergence derived from ERA-Interim reanalysis data. (a) Time series of wind convergence accumulated (November-November) by autumn in the Amerasian and Eurasian basins for 1980-2014 (solid purple line), and CryoSat-2 autumn ice volume for 2010-2014 (red stars). The 34-year wind convergence mean (solid black line) and standard deviation (dashed black line) are shown. (b) The relationship between anomalies of wind convergence and autumn CryoSat-2 ice volume. There is a weak, positive correlation (r^2 = 0.38).

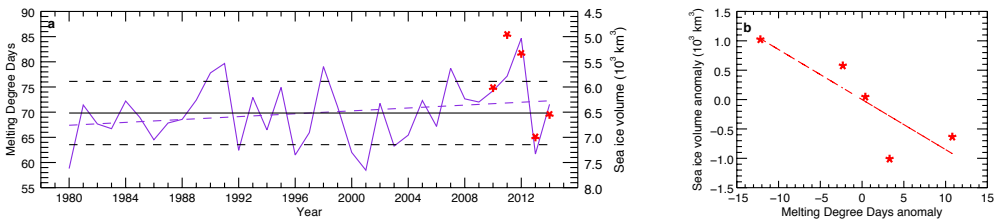

Figure 5.5: The relationship between autumn sea ice volume in the Amerasian and Eurasian basins, and annual melting degree days (M_{DD}) derived from ERA-Interim reanalysis data. (a) Time series of M_{DD} accumulated (November-November) by autumn in the Amerasian and Eurasian basins for 1980-2014 (solid purple line), and CryoSat-2 autumn ice volume for 2010-2014 (red stars). The 34-year M_{DD} mean (solid black line) and standard deviation (dashed black line) are shown. (b) The relationship between anomalies of M_{DD} and autumn CryoSat-2 ice volume. There is a strong, negative correlation (r^2 = 0.73).

The next aim of this study was to establish whether inter-annual variations in melting strongly affect the quantity of autumn sea ice elsewhere in the Arctic. Firstly, the hemisphere-wide trends in both parameters were compared (Figures 5.6a and 5.6b), and correlations calculated over the CryoSat-2 period (Figure 5.6c). At the hemisphere scale, the correlation between total autumn sea ice volume and the number of M_{DD} (r^2 = 0.75) is even stronger than in the Amerasian and Eurasian basins – on average, 142 km^3 of ice is lost per additional M_{DD}. The relationship is stronger still for hemisphere-wide MYI volume and M_{DD} (r^2 = 0.78), but weak for FYI and M_{DD} (r^2 = 0.12). This suggests that the

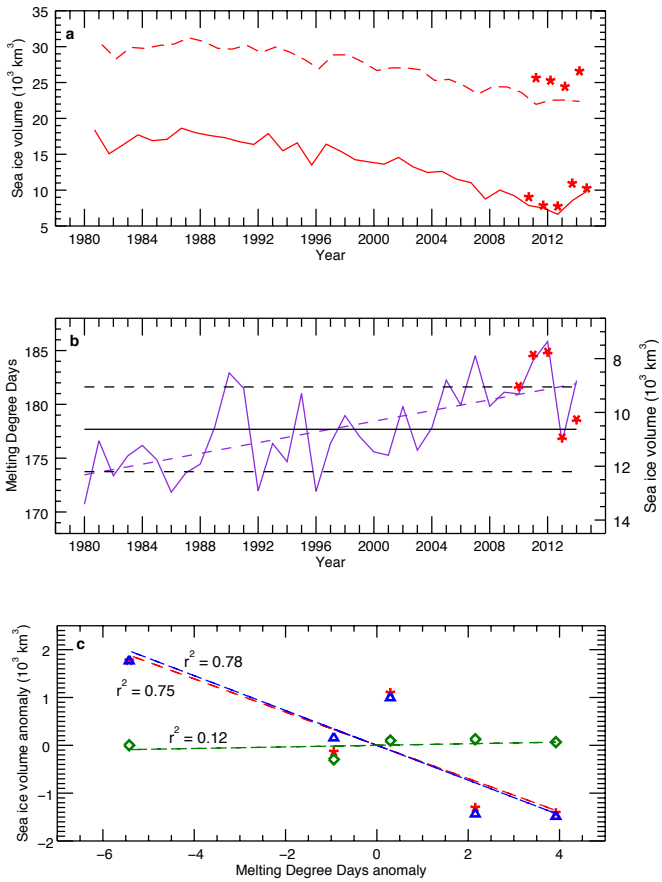

Figure 5.6: The relationship between Arctic sea ice volume and summer melting. (a) Time series of PIOMAS model arctic sea ice volume for autumn 1980-2014 (solid line) and spring 1981-2014 (dashed line). CryoSat-2 volume estimates (red stars) are plotted for 2010-2014. (b) Time series of average melting degree days (M_{DD}) across the Arctic Ocean for 1980-2014 (solid purple line), and CryoSat-2 autumn ice volume for 2010-2014 (red stars). The M_{DD} time series mean (solid black line) and standard deviation (dashed black lines) are shown. (c) The relationship between anomalies of CryoSat-2 autumn ice volume and the number of M_{DD} during the preceding year, for first-year ice (green diamonds; r^2 = 0.12), multi-year ice (blue triangles; r^2 = 0.78) and total ice (red stars; r^2 = 0.75).

total amount of Arctic sea ice come autumn is dependent on the amount of MYI that has survived the summer melt. This is evident from maps of sea ice thickness (Figure 4.1), which show a thicker than average (by 21%) ice cover in the autumn of 2013, in the MYI region north of Greenland and Ellesmere Island.

Next, regional correlations were calculated between autumn sea ice volume and M_{DD}. This showed that there are regional variations in the strength of the relationship (Table 5.1). The poorest correlations are in the Greenland ($r^2 = 0.10$), Iceland ($r^2 = 0.17$), and Barents ($r^2 = 0.26$) Seas, which is likely related to the strong influence of atmospheric circulation and wind forcing [*Serreze et al.*, 1993] on sea ice transport, and therefore volume, in these regions. Sea ice conditions in the Greenland Sea are also influenced by ocean-driven ice fluxes through the Fram Strait, which is the primary region of sea ice export out of the central Arctic [*Kwok*, 2004]. In contrast, ice volumes in Hudson Bay and the Canadian Archipelago and Northwest Passage are highly correlated with M_{DD} ($r^2 \geq 0.90$). The Hudson Bay is almost entirely surrounded by land and the Canadian Archipelago and Northwest Passage region consists of numerous islands and narrow channels, preventing significant ice motion out of both regions for most of the year [*Flato and Brown*, 1996]. As a consequence, ice volume is likely to be dominated by in situ growth and decay due to local temperature fluctuations. The volume of ice lost per M_{DD} is dependent on the size of the region (Figure 5.7). These findings illustrate the need to survey large fractions of the Arctic sea ice pack to understand the influence of climate on hemisphere-wide changes in the ice cover, or else results may be biased by local dependences on sea ice drift.

It is possible that estimates of M_{DD} and sea ice volume are correlated through their common dependence on sea ice concentration data. M_{DD} were computed from air temperatures derived from ERA-Interim reanalysis, which incorporates sea ice concentration measurements in the model data assimilation system [*Dee et al.*, 2011], and the sea ice volume estimates also used sea ice concentration data in the scaling from thickness to volume (Section 3.4.10). However, the degree of co-dependence is expected to be small, because sea ice thicknesses are only weakly related to sea ice concentration as they are computed only in regions of high concentration (75% or more). Moreover, if the reanalysis data were strongly dependent on sea ice concentration, then a co-dependence should also exist between estimates of sea ice volume and snow loading, due to different evaporation parameters being applied in the reanalysis depending on whether sea ice or ocean is present [*Dee et al.*, 2011]. Yet the correlation between volume and snow loading was very weak ($r^2 = 0.05$). It is concluded, therefore, that the high correlation between changes in sea ice volume and

Table 5.1: The relationship between CryoSat-2 autumn sea ice volume and the number of melting degree days (M_{DD}) during the preceding year, for 2010-2014. The area (10^3 km^2) and rate of volume loss (km^3/M_{DD}) are given, for 10 Arctic Ocean regions (see Figure 3.12 for region locations).

Region	Area	r^2	Rate of volume loss per M_{DD}
Amerasian Basin (1)	2570	0.67	37.77
Eurasian Basin (2)	2090	0.66	29.36
Canadian Archipelago and Northwest Passage (3)	1340	0.98	20.11
Hudson Bay (4)	1250	0.90	10.10
Baffin Bay (5)	940	0.40	2.60
Greenland Sea (6)	730	0.10	3.32
Iceland Sea (7)	510	0.17	-1.30
Barents Sea (8)	1500	0.26	-4.60
Kara Sea (9)	860	0.48	8.47
Siberian Shelf Seas (10)	2190	0.86	27.23

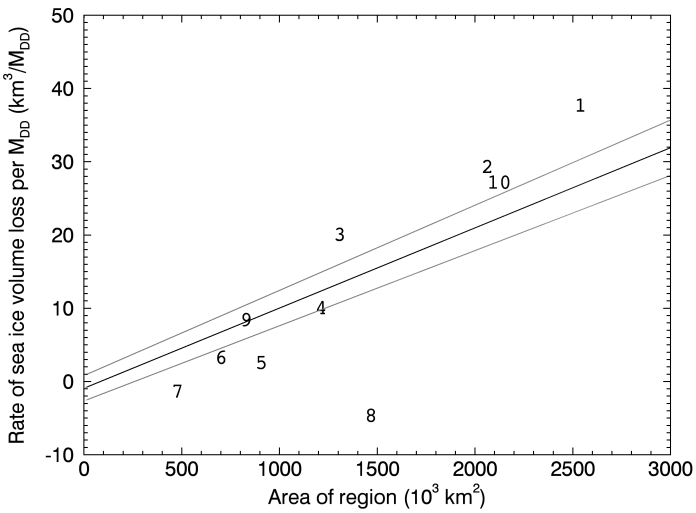

Figure 5.7: The influence of regional area on the rate of sea ice volume loss per melting degree day (M_{DD}). The rate of volume loss (Table 5.1) for Arctic regions 1-10 (see Figure 3.12 for region locations) is, to a degree, dependent on the area of the region (r^2 = 0.56). The solid black line shows the linear fit to results for rate of volume loss per M_{DD} vs. area, for 400 randomly selected Arctic Ocean regions. The solid grey lines are the standard deviation of this fit.

melting is a result of their thermodynamic relationship and not an artefact of their co-dependence on sea ice concentration data.

5.5. Conclusions

In this chapter, the first five years of CryoSat-2 mission data have been used in conjunction with ERA-Interim reanalysis data to provide insight into the drivers of inter-annual variations in Northern Hemisphere sea ice volume. A modest reduction in total and MYI volume was observed between autumn 2010 and spring 2013. These reductions were followed by a marked increase in volume in the autumn of 2013, with total volume increasing by 41% compared to the previous year and remaining higher than the 5-year average through to autumn 2014. The increase was due to the retention of thick, predominantly MYI, north of Greenland and Ellesmere Island over the summer of 2013. By autumn 2013 the sea ice cover was on average 21% thicker, and presumably stronger, than during the previous three autumns. Although Arctic-wide melting has increased steadily over recent decades – by 0.25 M_{DD} $year^{-1}$, on average, since 1980 (Figure 5.6b) – there was a marked (5% M_{DD}) reduction in 2013 prior to the sharp increase in autumn sea ice volume. This made 2013 an anomalously cool year, with temperatures that were more typical of conditions during the late 1990's. If Arctic temperatures continue to rise, as is widely predicted [*Overland and Wang*, 2013], the volume of sea ice will diminish further, and the ice pack may become increasingly dependent on regional responses to thermodynamic, wind and ocean forcing. Although a longer observational record is needed before trends in Arctic sea ice volume can be established with confidence, the recent increases do not reverse the long-term decline apparent in model-based reanalyses (Figure 5.6a) [*Holland et al.*, 2010; *Schweiger et al.*, 2011]. However, they do demonstrate that the long-term decline is punctuated by inter-annual variability, which allows for positive, negative and stable variations in the range ±600 km^3 yr^{-1}. These measurements also highlight the importance of obtaining Arctic-wide observations when attempting to quantify trends or to establish their origins.

6. Near real time Arctic sea ice thickness and volume estimates from CryoSat-2

6.1. Introduction

Chapters 3-5 have introduced and analysed Arctic sea ice thickness estimates produced using final release CryoSat-2 data. The latency of the final release datasets is typically one month, due to the time required to determine precise satellite orbits. However, since April 2015 ESA have provided fast delivery CryoSat-2 data based on preliminary orbits, and have backdated the data availability to the start of the mission in October 2010. This chapter introduces the fast delivery CryoSat-2 data (Section 6.1) and the method applied to compute Northern Hemisphere sea ice thickness and volume in NRT (Section 6.2). The data are analysed for one sea ice growth season from October 2014 to April 2015. This includes a direct comparison with the archive product that is computed using final release CryoSat-2 data (Section 6.3), and an analysis of the spatial and temporal coverage of the NRT data (Section 6.4). The work presented in this chapter is the subject of a paper that has been published in The Cryosphere by *Tilling et al*. [2016] titled "Near Real Time Arctic sea ice thickness and volume from CryoSat-2".

NRT measurements of sea ice thickness will allow timely assessments of Arctic environmental change. In addition, although day-to-day operational activities in the Arctic region (Section 1.4.3) require measurements with greater spatial and temporal sampling than can be achieved using a single satellite altimeter, NRT satellite thickness data have the potential to improve the skill of short-term model forecasts. These are, in turn, a resource for operational activities. The U.S. Navy's ACNFS (Section 1.5.2) [*Hebert et al*., 2015; *Posey et al*., 2015], for example, provides short-term (1 to 7 day) forecasts of conditions such as the location of the sea ice edge, which can improve the safety and efficiency of the Navy's operational missions [*Navy*, 2014; *Posey et al*., 2015]. Although the ACNFS currently assimilates NRT sea ice concentration data, it has been suggested that forecast model skill could be further improved by assimilating NRT measurements of sea ice thickness also [*Day et al*., 2014]. On slightly longer (seasonal) timescales, forecast models are currently able to predict the area of September sea ice with good confidence if the distribution of sea ice thickness is known in late spring [*Sigmond et al*., 2013]. To initialize such models with known thickness distributions, and analyse their output, [*Chevallier and Salas-Melia*, 2012], rapid and reliable satellite observations are required. Despite these potential benefits, it is nevertheless recognised that the value of NRT sea ice thickness

observations derived from repeat satellite altimetry does have limits. For example, some model systems show higher forecast skill when initialized with thickness distribution (and for some months volume anomaly) estimates from early summer [*Chevallier and Salas-Melia*, 2012]. Summer is a period when sea ice thickness measurements from satellite are traditionally unavailable in the Arctic due to the presence of melt ponds (Section 3.4.2). Similarly, although forecasts could benefit the planning of Arctic operations [*Meier et al.*, 2014; *Stewart et al.*, 2007], the data themselves are likely too sparse to be utilised directly.

6.2. Estimating near real time sea ice thickness and volume from fast delivery CryoSat-2 data

6.2.1. Fast delivery CryoSat-2 data

NRT estimates of Northern Hemisphere sea ice thickness and volume are produced using L1b fast delivery CryoSat-2 data, which are available from ESA an average of 36 hours after acquisition by the satellite. The data format and measurement information are identical to the final release L1b data, described in Section 3.2. As with the final release, ESA perform an on ground processing chain to the raw fast delivery data before releasing the L1b product. Prior to March 26th 2015, ESA applied the Baseline-B processing chain to the raw fast delivery data, and Baseline-C has been applied since. This is different to the final release, where Baseline-B was used before February 21st 2015, Baseline-C since April 1st 2015, and Baseline-BC between February 22nd and March 31st 2015. The number of range bins for each waveform depends on the satellite operating mode and the baseline of the data – Baseline-B SAR mode has 128 bins, Baseline-C SAR mode has 256 bins, Baseline-B SARIn mode has 512 bins and Baseline-C SARIn mode has 1024 bins. In the fast delivery data the wet tropospheric, dry tropospheric and inverse barometric corrections are missing in 94% of cases for Baseline-B data, but in less than 1% of cases for Baseline-C data. In these instances, all three of the corrections are missing. When available, these corrections are applied when calculating sea ice and ocean elevations, along with the modelled ionospheric, ocean tide, long period equilibrium tide, ocean loading tide, solid earth tide, and geocentric polar tide corrections (Section 3.4.5).

The major difference between the fast delivery and final release CryoSat-2 data is the orbits applied. An accurate determination of the satellite orbit is required to compute surface elevations above a reference ellipsoid (Sections 2.2 and 3.4.5) from either dataset. For all L1b data ESA apply the satellite orbit to the window delay, and the orbit is also provided in the L1b product (Section 3.2). For the final release data product,

ESA perform a ground-based Precise Orbit Determination (POD), which requires a dense set of measurements regarding the position and velocity of the satellite [*Wingham et al.*, 2006]. These are used on-ground to create a model of the precise orbit, which also involves modelling of the forces acting on the satellite. The primary means of making position and velocity measurements is with the on-board Doppler Orbit and Radio positioning Integration by Satellite (DORIS) receiver, which measures the relative velocity of the satellite to an extensive network of ground beacons. The messages uplinked from the beacons include time signals that allow the DORIS receiver time to be accurately determined. The DORIS receiver also includes software to determine the satellite's position in real-time and perform on-board computation of the orbit, which is then relayed to the ground segment. This is known as the DORIS navigator orbit and it is included in the fast delivery CryoSat-2 data to provide good quality orbit estimates before the POD can be produced. The DORIS navigator orbit is estimated to be accurate to 30 cm in the radial direction. The fast delivery data are more susceptible to orbit dropout, meaning that certain orbits, for which the orientation of the satellite could not be sufficiently determined, are not included in the dataset.

6.2.2. Method and uncertainties

The processing steps used to estimate NRT Arctic sea ice thickness from L1b fast delivery SAR and SARIn mode CryoSat-2 data are identical to those applied to the final release L1b Baseline-B data to produce archive values of sea ice thickness and volume. These are described in detail in Chapter 3. To allow for identical processing of both SAR and SARIn mode Baseline-B and Baseline-C fast delivery data acquired over Arctic sea ice, all waveforms are cropped to 128 bins, ensuring that the waveforms are positioned at approximately the same location within the 128 bins. To rapidly compute the NRT data product, the timely availability of ancillary data is crucial. Sea ice concentration values are taken from the NSIDC NRT product [*Maslanik and Stroeve*, 1999, updated daily], rather than the final release NSIDC concentration data that is used with final release CryoSat-2 data (Section 1.6.1 and 3.3.1). The NRT ice concentration data are provided on the same grid as the final data, and are available by 01:00 UTC two days after measurement. The ice type data used is the same as that described in Section 3.3.2 and is available by 01:00 UTC the day after measurement. Values for sea ice density (Section 3.3.3), and snow depth and density (Section 3.3.4), and are taken from the same historical datasets as before. The fast delivery CryoSat-2 data are typically available 36 hours after acquisition from the satellite, but this can vary from 1-3 days, so the NRT sea ice processor is run at a latency of three days to ensure sufficient data is available. NRT sea ice thickness data are output Arctic-wide

on to a 5 km square grid for the previous 2, 14 and 28 days (Figure 6.1), by averaging all thickness measurements within a 25 km radius of the centre of each grid cell and assigning equal weighting to all points. Although this resolution is coarser than the maximum afforded by the CryoSat-2 altimeter and the satellite orbit (Section 2.4) it allows the NRT sea ice thickness product to be compared with estimates computed from the entire archive of CryoSat-2 data which, because it extends over a greater time period, has been evaluated with respect to in situ observations (Section 4.3). Sea ice volume is then computed Arctic-wide and within fixed oceanographic basins, as described in Section 3.4.10. Again, NRT sea ice concentration data is used. The NRT sea ice thickness and volume data produced are publicly available to download at http://www.cpom.ucl.ac.uk/csopr/seaice.html.

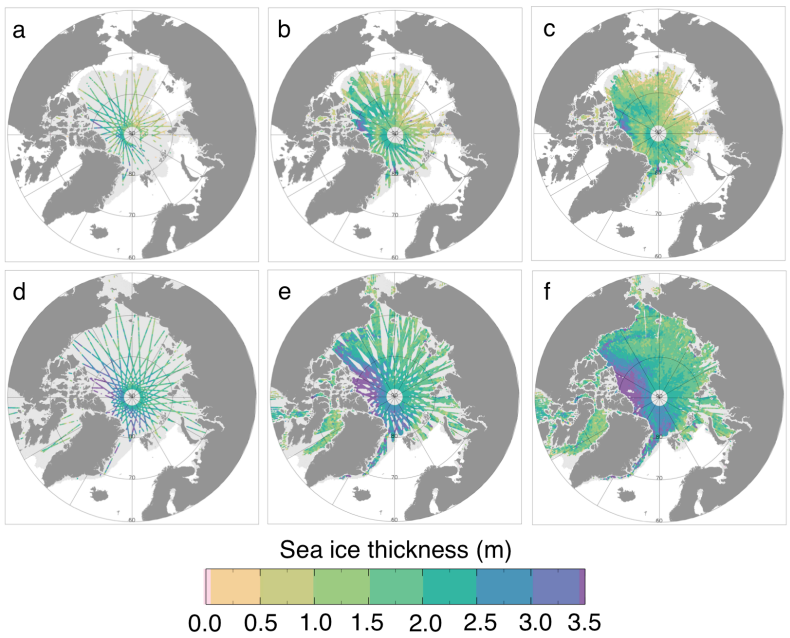

Figure 6.1: Near real time (NRT) Arctic sea ice thickness estimates from CryoSat-2. (a)-(c) Thickness estimates for the final 2, 14 and 28 days in October 2014, respectively. (d)-(f) Thickness estimates for the final 2, 14 and 28 days in March 2015, respectively. NRT sea ice thickness data are output Arctic-wide on a 5 km square grid. All thickness measurements within a 25 km radius of the centre of the grid are averaged, with all points receiving equal weight. The sea ice extent mask is shaded in light grey, and highlights unmapped areas of the sea ice.

It is assumed that uncertainties in Arctic-wide NRT sea ice volume are equivalent to the uncertainties on archive estimates of sea ice volume – typically about 13.5%, with

small variations from month to month (Section 3.5). However, it is now necessary to consider that the uncertainty on a grid cell thickness will increase with fewer days of data coverage. This is due to the spatially correlated errors in the interpolation of sea surface heights (Section 3.5.1). As before, the 4 cm error in sea surface height will be reduced in the averaging only by the square root of the number of individual passes crossing the averaging window. When gridding a month or 28 days data this is typically 4 or more passes, resulting in a 2 cm freeboard uncertainty. This scales to ~20 cm thickness, or 11% of a typical growth season thickness of 1.8 m [*Tilling et al.*, 2015] for gridded 28-day thicknesses. Combined with the error of 23% from other sources (Section 3.5.2) this brings the total error on the 28-day 5 km grid sea ice thickness data to 25%. However, for 14 days of data the averaged freeboard measurement comes from an average of 1.5 satellite passes, resulting in a 3.3 cm freeboard uncertainty due to the error in sea surface height. This scales to ~33 cm thickness, or 18% of a typical growth season thickness of 1.8 m, which brings the total error on 14-day gridded sea ice thickness to 29% when combined with the error of 23% from other sources. For 2 days of data the averaged freeboard measurements often come from just one satellite pass. Therefore the full 4 cm uncertainty in sea surface height contributes to the freeboard error, which scales to ~40 cm for thickness, or 22% of a typical thickness of 1.8 m. Combined with the error of 23% from other sources this brings the total error on the 2-day 5 km grid sea ice thickness data to 32%. As with the error budget calculated for the archive sea ice product, this is a first attempt to characterise local uncertainties in sea ice thickness. These could be refined with improved knowledge of snow depth, snow density, and sea ice density and the lengths over which their uncertainties are correlated.

6.3. A comparison of near real time and archive sea ice thickness estimates

To assess the reliability of the NRT sea ice dataset it was compared to the archive product, which is derived from the final CryoSat-2 data release. Archive data have shown excellent agreement with an extensive set of independent observations (Section 4.3 and *Tilling et al.* [2015]). It is currently not possible to directly evaluate the NRT sea ice product against *in situ* measurements, as the overlap between coverage periods is too short.

First, the NRT processing was assessed at orbit-scale by calculating point-by-point differences between NRT and archive sea ice freeboards using a single track of CryoSat-2 data from April 2015, for which all geophysical corrections were present in

both datasets. The track consists of 3,968 lead and 5,246 freeboard measurements for the NRT data compared with 3,970 lead and 5,242 freeboard measurements for the archive data. Along this track, NRT and archive freeboards show excellent agreement, with a mean difference of 0.02 cm (Figure 6.2a).

Next, sea ice thickness and volume were compared based on the NRT and archive products, using seven months of data acquired between October 2014 and April 2015, which corresponds to a season of ice growth. The thickness comparison was done over the 5 km square grid on which NRT data are output. In general, NRT and archive estimates of sea ice thickness are in excellent agreement, with a mean difference of 0.9 cm (Figure 6.2b). NRT and archive estimates of sea ice volume are also in excellent agreement, with an average difference of 175 km^3 (Figure 6.2c) across the entire Arctic region. The negative freeboard and thickness values apparent in Figure 6.2a and Figure 6.2b respectively are likely a consequence of negative freeboard measurements that occur due to random noise in radar echoes from thin ice floes, caused by radar speckle (Section 3.4.8). These freeboards are included in the processing to ensure that the average freeboard, and therefore thickness, is not biased high. Overall, differences between NRT and archive estimates of sea ice thickness and volume fall well within the corresponding estimates of their uncertainties (Section 6.2.2).

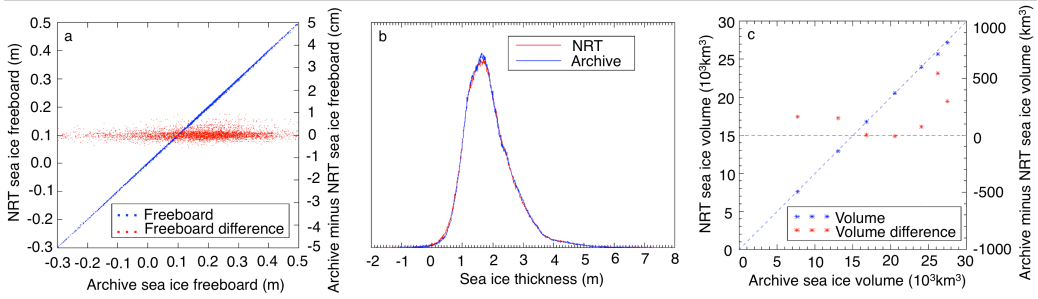

Figure 6.2: Comparison of near real time (NRT) and archive estimates of Arctic sea ice freeboard, thickness, and volume, from CryoSat-2. (a) Crossplot of point-by-point sea ice freeboard for an Arctic track in April 2015. Also shown is the difference (archive minus NRT) in sea ice freeboard between the datasets. (b) Normalised distribution of NRT and archive thickness estimates over the period October 2014-April 2015, for all grid cells where measurements are available for both datasets. (c) Crossplot of sea ice volume for October 2014-April 2015. Also shown is the difference (archive minus NRT) in sea ice volume between the datasets.

Archive estimates of sea ice volume are larger than NRT estimates partly as they are computed using the final sea ice concentration dataset, which contains higher values than the NRT concentration dataset. For example, sea ice volumes were recalculated using NRT sea ice thickness values but final sea ice concentration and this reduced the departure from the archive estimates of sea ice volume to an average of 100 km^3. A contribution to the remaining difference is likely the combined absence of the wet tropospheric, dry tropospheric and inverse barometer corrections in 93.8% of the Baseline-B fast delivery CryoSat-2 data. This is reduced to 0.3% for Baseline-C data. The mean sea ice thickness for both the NRT and archive datasets is ~1.8 m, and there is no bias between them, with or without geophysical corrections applied. When the corrections are missing the NRT and archive thickness values at any given location differ, on average, by just 1.1 cm with a standard deviation of 23.0 cm (Figure 6.3a). This is reduced to 0.1 cm with a standard deviation of 7.4 cm when the corrections are present (Figure 6.3b). There is no spatial pattern to these differences. Despite the improvement in performance of Baseline-C NRT data compared with Baseline-B it

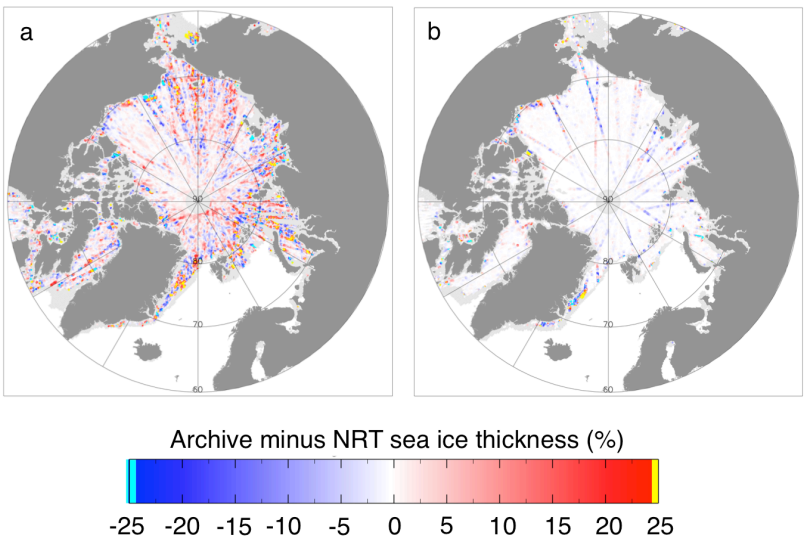

Figure 6.3: The impact of geophysical corrections on near real time (NRT) Arctic sea ice thickness estimates from CryoSat-2. (a) Percentage change in archive minus NRT thickness estimates for the final 28 days of March 2015. In March 2015 the wet tropospheric, dry tropospheric and inverse barometer corrections were missing in 80% of cases. (b) Percentage change in archive minus NRT thickness estimates for the final 28 days of April 2015. In April 2015 the wet tropospheric, dry tropospheric and inverse barometer corrections were missing in 0% of cases.

is concluded that the satellite orbits and on-ground processing applied to fast delivery CryoSat-2 data are sufficient to determine accurate measurements of Arctic sea ice thickness and volume for both baselines. The thickness differences between the archive and NRT data products are not significant for either baseline given the estimated uncertainty on thickness and the typical thickness of sea ice floes.

6.4. Near real time data coverage

The spatial distribution of the NRT sea ice thickness data (Figure 6.1) for any given time period depends on the nature of the CryoSat-2 orbit over that period. CryoSat-2 has an orbit repeat period of 369 days, which is built up by successive shifts of a 30-day repeat sub-cycle, meaning that uniform coverage of the Arctic Ocean is achieved every 30 days (Section 2.4.1). The density of orbit crossovers increases with latitude up to the CryoSat-2 limit of 88°N, and also with the number of days of coverage. CryoSat-2 orbit patterns are visible in maps of sea ice thickness for 2 days (Figures 6.1a and 6.1d) and 14 days (Figures 6.1b and 6.1e) coverage. The orbits are clearer at lower latitudes, below about 80°N. Over 28 days (Figures 6.1c and 6.1f), almost complete coverage across the sea ice pack is achieved. However, there are still small areas of unmapped sea ice, and these typically occur at the ice edge. In these unmapped areas the sea ice concentration is above 15%, which is the value used as the sea ice margin threshold (Section 3.4.10), but below 75%, which is the concentration required for a region to be classed as containing sea ice (Section 3.4.2).

To determine the utility of the 5 km grid measurements of NRT sea ice thickness, a detailed assessment of the spatial and temporal distribution of the data was performed, and compared to the equivalent for archive data. The percentage of sea ice covered by NRT and archive data in 1 degree latitude bands from 60-90°N was calculated, for the final 2, 14 and 28 days of each month of the 2014-2015 sea ice growth season. This was done for data from October 2014 to April 2015, and averaged over all months (Figure 6.4a). The equivalent plot was produced for the mean data separation in each latitude band, where separation is simply the square root of the sea ice covered area, divided by the number of measurements in each band (Figure 6.4b). For 28 days data coverage, sea ice at latitudes between 85-88°N is mapped in its entirety by the NRT and archive products and the data separation drops to 5.0 km in each 1 degree latitude band, which is simply the grid separation. For 14 days coverage the CryoSat-2 orbit pattern achieves its maximum coverage for NRT data, of 98%, between 86 and 87°N but achieves 100% coverage for archive data between 86-88 °N. These correspond to a mean data separation of 5.1 km and 5.0 km (the grid separation), respectively. The maximum NRT coverage over 2 days is 91%, between 87 and 88°N, where the mean

data separation is 5.2 km. This increases to 99%, between 87 and 88°N for archive data, with a mean data separation of 5.1 km. For both NRT and archive data the percentage of ice mapped decreases with decreasing latitudes, and the separation between data points increases, although there is some fluctuation in these trends that is likely due to the shift in the CryoSat-2 orbit pattern producing less favourable coverage for a given month. CryoSat-2 does not observe sea ice north of 88°N, so the percentage of ice mapped drops to 0% for 2, 14 and 28 days coverage in the region 88-90°N for both datasets. On average, the NRT sea ice thickness data maps 20, 51 and 66% of the Arctic sea ice north of 60°N every 2, 14 and 28 days respectively. This corresponds to a measurement within 14, 7 and 6 km of each location in the Arctic every 2, 14 and 28 days. For archive data the coverage increases to 23, 57 and 69% every 2, 14 and 28 days respectively, which corresponds to a measurement within 13, 7 and 6 km of each location in the Arctic.

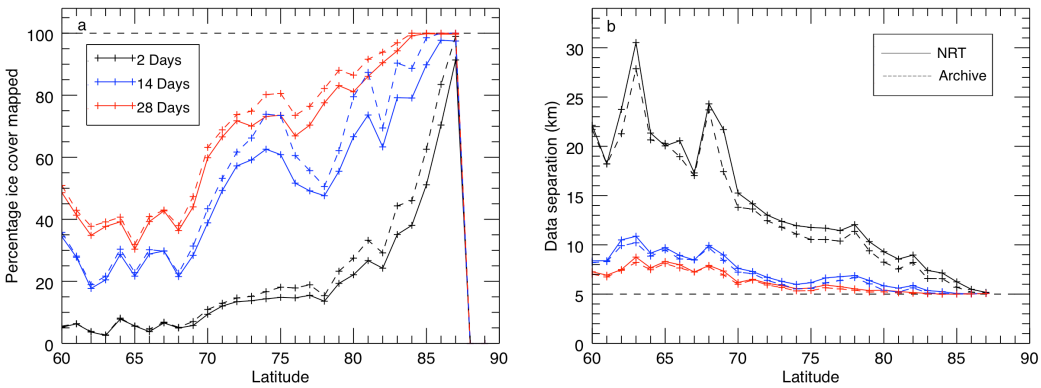

Figure 6.4: Spatial and temporal sampling of near real time (NRT) and archive Arctic sea ice thickness, north of 60°N. (a) Percentage of sea ice cover mapped in 1° latitude bands, averaged over each month from October 2014-April 2015. Data are plotted for the final 28, 14, and 2 days of all months. (b) Mean separation between measurement points in 1° latitude bands, averaged over each month from October 2014-April 2015. Data are plotted for the final 28, 14, and 2 days of all months. Solid lines = NRT data, dashed lines = archive data.

The distribution of the NRT sea ice thickness measurements also varies with oceanographic basin and month, and the nature of the monthly variation depends on the region being observed. This is an important consideration for those wishing to use the data in a specific region of interest, or over the entirety of the sea ice growth season. The percentage of ice cover mapped by the NRT product was calculated for six key oceanographic regions – the Amerasin basin, Eurasian basin, Canadian Archipelago and

Northwest Passage, Hudson Bay, Greenland Sea, and Beaufort Sea – for the final 28 days of each month of the 2014-2015 sea ice growth season (Figure 6.5a). This was compared to the percentage of ice cover mapped by archive data in the same regions (Figure 6.5b). Region locations are shown in Figure 3.12. The percentage of the ice cover mapped in the Amerasian and Eurasian basins is high (≥ 76% for NRT data and ≥ 83% for archive data), with just a small increase over the growth season. Both regions are almost entirely covered in sea ice year-round, which means that the areal fraction of unmapped sea ice at the ice edge is fairly consistent throughout the year. However, this is not the case for regions with more seasonal ice cover, such as the Canadian Archipelago and Northwest Passage, Hudson Bay, and the Beaufort Sea, where NRT and archive coverage improves throughout the growth season and peaks in February or March. In these regions, as the extent of the sea ice cover increases through winter, the unmapped area at the sea ice edge becomes a decreasing fraction of the ice-covered area, and a greater percentage of the ice cover is mapped. In addition, as the sea ice concentration increases through winter, echoes from sea ice floes becomes less noisy and are more likely to be included in the processing (Sections 3.4.2 and 3.4.4.2). Coverage in the Greenland Sea generally improves throughout the growth season, although there is some variation in this pattern due to fluctuations in the width of the unmapped area at the sea ice edge, which could be a consequence of the rapid sea ice transport in this sector. Overall, coverage is lowest for the Greenland Sea, Canadian Archipelago and Northwest Passage, and Hudson Bay. Due to the location of the Greenland Sea, there is also a persistent presence of unmapped sea ice along its eastern edge. The Canadian Archipelago and Northwest Passage, and Hudson Bay

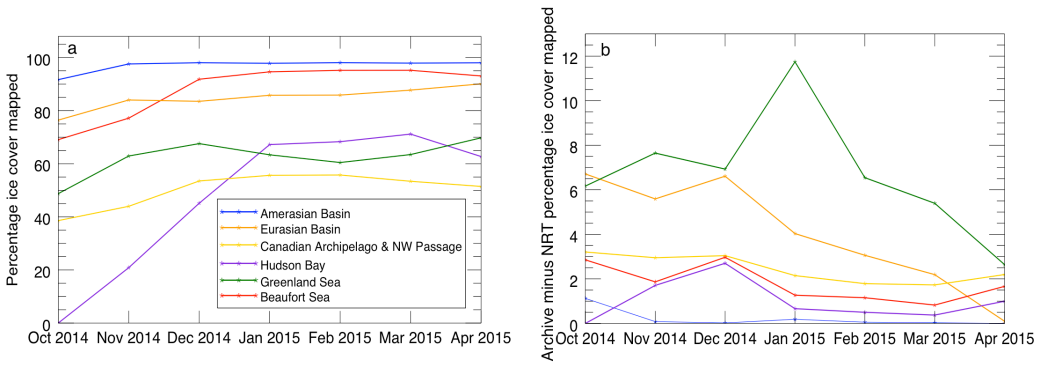

Figure 6.5: Regional and temporal sampling of near real time (NRT) and archive Arctic sea ice thickness. See Figure 3.12 for region locations. (a) The percentage of sea ice cover mapped by the NRT product in each month, for six key oceanographic basins. (b) The difference (archive – NRT) in percentage ice cover mapped, in each month, for six key oceanographic basins.

are in close proximity to substantial coastal areas, where it is difficult to construct sea surface height due to the absence of leads in the sea ice pack. Although there is spatial variation in the coverage of the NRT sea ice thickness data, both with latitude (Figure 6.4) and oceanographic basin (Figure 6.5a), there is no significant spatial variability in the difference between the NRT and archive data coverage (Figure 6.4 and Figure 6.5b).

The analysis of NRT data sampling was extended by calculating the percentage of sea ice mapped in all Arctic Ocean basins (Figure 3.12) at the beginning and end of the sea ice growth season (Table 6.1), for the final 2, 14 and 28 days of each month of the 2014-2015 growth season. In each month the coverage improves with the number of days sampling, in every basin. The coverage also improves from October to March, for each time period, for all but one basin; the Canadian Archipelago/Northwest Passage experiences a drop in coverage over the growth season, for the 2-day observation period. However, this change is very small, and over short observation periods some variability is expected in the proportion of ice cover mapped as a consequence of the CryoSat-2 orbital repeat pattern. This becomes more important in regions such as the Canadian Archipelago, where there is a high fraction of land interspersed with ocean. The Bering Sea, the Sea of Okhotsk, the White Sea, the Baltic Sea and surrounding Gulfs and the Labrador Sea have the smallest proportional ice cover mapped in March 2015. These are regions of highly seasonal sea ice cover, and by the end of the growth season the unmapped area at the ice edge still constitutes a sizable fraction of the ice–covered area. In addition, they are all southerly basins (below 70°N), which are sampled with reduced spatial density by CryoSat-2. The most extensively sampled areas are in the central Arctic – the Amerasian and Eurasian basins – which experience substantial year-round sea ice cover and are at high latitudes. In conclusion, the location, seasonality, and dynamic nature of any sea ice region are important considerations when assessing the reliability of the NRT Arctic sea ice thickness product.

6.5. Conclusions

This chapter shows that NRT estimates of sea ice thickness determined from fast delivery CryoSat-2 data can be computed within a few days of the raw data acquisition, and with a certainty that is comparable to that of the standard archive product, which is typically available six months later. This allows for timely and reliable assessments of local and regional sea ice conditions, which should benefit activities that depend on such data (Section 1.4.3). A good example is seasonal forecasts of Arctic sea ice properties that have previously utilised sparse airborne measurements to adjust model-

Table 6.1: Variations in the sampling of CryoSat-2 near real time (NRT) sea ice thickness products in 17 Arctic Ocean regions (see Figure 3.12 for region locations).

Region	Data Coverage (% of ice cover mapped)					
	2 days		14 days		28 days	
	Oct 2014	Mar 2015	Oct 2014	Mar 2015	Oct 2014	Mar 2015
Amerasian Basin (1)	33	38	78	82	92	98
Eurasian Basin (2)	24	44	58	73	76	88
Canadian Archipelago & Northwest Passage (3)	9	7	31	37	39	53
Hudson Bay (4)	0	6	0	48	0	71
Baffin Bay (5)	0	15	0	56	0	81
Greenland Sea (6)	8	13	31	50	49	63
Iceland Sea (7)	0	16	0	44	0	57
Barents Sea (8)	0	9	17	32	18	47
Kara Sea (9)	2	17	15	46	16	58
Siberian Shelf Seas (10)	11	20	38	60	49	85
Bering Sea (11)	n/a	3	n/a	35	n/a	40
Sea of Okhotsk (12)	n/a	0	n/a	21	n/a	33
White Sea (13)	n/a	0	n/a	6	n/a	6
Baltic Sea & surrounding Gulfs (14)	n/a	0	n/a	0	n/a	0
Labrador Sea (15)	n/a	1	n/a	13	n/a	19
Gulf of St Laurence & Nova Scotia Peninsula (16)	n/a	n/a	n/a	n/a	n/a	n/a
Beaufort Sea (17)	17	20	59	83	69	95

based initial ice thickness distributions [*R W Lindsay et al.*, 2012]. Although of coarser spatial resolution, the NRT thickness estimates produced for this study complement the airborne data because of their wider spatial and temporal extent [*Chevallier and Salas-Melia*, 2012; *Posey et al.*, 2015], and even though the data do not extend into the summer season (Section 1.4.3), their use should nevertheless lead to improved model skill [*Day et al.*, 2014; *Sigmond et al.*, 2013]. A previous study [*Rinne and Similä*, 2016] has highlighted the potential value of fast delivery CryoSat-2 data for the

classification of sea ice into discrete stages of its development – thin (<70 cm) and thick (>70 cm) FYI and MYI – in the Kara Sea. In this chapter that initial analysis of the mission potential has been extended to provide continuous measurements of sea ice thickness across the entire northern hemisphere. Together with records of NRT sea ice concentration [*Cavalieri et al.*, 1996, updated yearly; *Maslanik and Stroeve*, 1999, updated daily], which are also available in NRT, NRT estimates of sea ice thickness determined from CryoSat-2 will allow routine assessments of Arctic environmental conditions [*Stroeve et al.*, 2005] to additionally report changes in sea ice thickness and volume.

In addition to the CryoSat-2 measurements, NRT sea ice thickness estimates depend also on timely availability of sea ice concentration estimates [*Maslanik and Stroeve*, 1999, updated daily] and of classification of sea ice type (http://osisaf.met.no/p/ice/#type). The sea ice concentration and sea ice type datasets are currently available two days and one day after their measurement, respectively. Because the fast delivery CryoSat-2 data are typically available 1 to 3 days after acquisition, the latency of the NRT sea ice thickness product is in practice limited by the altimeter data. A more rapidly delivered product, to support by day-to-day activities in the Arctic, would require first improvements in the latency of the CryoSat-2 data, followed by either improvements in the latency of sea ice concentration data or the use of older sea ice concentration measurements as an approximation.

The NRT estimates are of comparable accuracy to those produced using the final release CryoSat-2 data, with a mean difference of 0.9 cm between NRT and archive estimates of sea ice thickness. The NRT and archive thickness differences, although small, vary temporally. The differences are reduced when all geophysical corrections are present in the fast delivery CryoSat-2 data, which is the case in 99.7% of the data since March 26th 2015, when the ESA on-ground processing chain switched from Baseline-B to Baseline-C. There is no spatial variability in the differences between the CPOM UCL NRT and archive data products. For the period from October 2014 to April 2015, the NRT dataset covers an average of 20, 51 and 66% of the Arctic sea ice north of 60°N every 2, 14 and 28 days respectively. This is equivalent to a measurement within 14, 7 and 6 km of each location in the Arctic every 2, 14 and 28 days. However, there are temporal and spatial variations in the data coverage. The time of year, location, and dynamic nature of any region of interest must be considered when assessing the reliability of the data. The next major steps in the advancement of the data are to develop improved estimates of snow loading on Arctic sea ice and to extend sea ice thickness observations in to the summer months. It would also be

beneficial to investigate the impact of different gridding methods, including the application of a distance weighting, on the gridded NRT sea ice thickness product. The sea ice thickness and volume error budget could be further constrained with improved knowledge on uncertainties in snow loading and sea ice density, and also by accounting for uncertainties in the propagation speed of the radar signals through the snow pack. NRT Arctic sea ice thickness data will continue to be publicly available over a 2, 14 and 28 day period at http://www.cpom.ucl.ac.uk/csopr/seaice.html.

7. Summary and outlook

7.1. Aims and achievements

In section 1.8, the primary aims of this research were stated. The first was to:

1.) Advance the development of the CPOM UCL sea ice processor

Chapter 3 provided an end-to-end, comprehensive description of the data processing steps employed to estimate Northern Hemisphere sea ice thickness and volume using CryoSat-2 radar altimeter data. This is a sea ice processing chain that has been under constant development at CPOM UCL since the early 1990s. However, two key developments were made as part of this project. Firstly, sea ice thickness and volume are now estimated across the entire CryoSat-2 Northern Hemisphere ROC whereas before they were confined to the ICESat domain (Figure 1.8 and Section 3.7.1). Secondly, an error budget was developed for CryoSat-2 estimates of sea ice thickness and volume (Section 3.7.2). The provision of sea ice thickness data from satellite is crucial to understanding how the Arctic ice cover is changing, due to cost and logistical difficulties associated with obtaining *in situ* sea ice thickness measurements. Despite a number of Arctic fieldwork campaigns (Section 1.6.2), *in situ* measurements are spatially and temporally sparse, especially in the Arctic summer when it is often unsafe to access the sea ice. This is also true of measurements of sea ice density and the depth and density of the snow cover on Arctic sea ice.

The second was to:

2.) Utilise CPOM UCL measurements of Arctic sea ice thickness and volume to investigate the factors that drive their interannual variability

Chapter 4 presented Arctic sea ice thickness and volume results output by the CPOM UCL processor. The inter-annual variability in these results was discussed in Section 4.4.3. In summary, between autumn 2010 and 2012, there was a 14% reduction in Arctic sea ice volume, in keeping with the long-term decline in extent. However, 33% and 25% more ice was observed in autumn 2013 and 2014, respectively, relative to the 2010-2012 seasonal mean, offsetting earlier losses. The peak autumn volume in 2013 manifested as a thicker than average sea ice cover in the MYI region north of Greenland and Ellesmere Island. Chapter 5 then examined the potential drivers of this variability by using ERA-Interim reanalysis data to investigate the influence of fluctuations in snow loading, wind-driven ice drift, and ice melting on sea ice volume. It

was concluded that the increase in autumn sea ice volume observed in 2013 was associated with a 5% drop in the number of days on which melting occurred. This corresponds to conditions more typical of the late 1990's. The sharp increase in sea ice volume after just one cool summer demonstrates the ability of Arctic sea ice to respond rapidly to a changing environment.

During the course of this project, a NRT product of Arctic sea ice thickness and volume became available. As a result, an additional project aim was adopted – namely to:

3.) Assess the utility of the NRT data product for operational use and assimilation into short-term forecast models, by investigating its spatial and temporal distribution

Chapter 6 introduced the NRT product and assessed its reliability by comparing it to the archive product, which is derived from the final CryoSat-2 data release. The NRT estimates are of comparable accuracy to the archive estimates, with a mean difference of 0.9 cm between NRT and archive sea ice thicknesses and a mean difference of 175 km^3 between NRT and archive sea ice volumes (Section 6.3). Next, the spatial and temporal coverage of the NRT data was assessed. This analysis found that the NRT dataset covers an average of 20, 51 and 66% of the Arctic sea ice north of 60°N every 2, 14 and 28 days respectively. This is equivalent to a measurement within 14, 7 and 6 km of each location in the Arctic every 2, 14 and 28 days. However, there are temporal and spatial variations in the data coverage. The time of year, location, and dynamic nature of any region of interest must be considered when assessing the reliability of the data (Section 6.4).

Accurate and timely information on sea ice thickness is required among Arctic operational services (Section 1.4.3). Knowing the current state of the Arctic sea ice thickness in a specific location is crucial when considering building specifications and costs for exploration platforms and ice-classed ships, transit speeds, and navigation difficulties and risks. At present, the NRT sea ice thickness data presented here are likely too sparse to be utilised directly by operational services. However, Arctic-wide observations of sea ice thickness in NRT have the potential to improve the skill of short-term model forecasts, which are, in turn, a resource for operational activities (Section 6.1). Some short-term forecast models have shown an improvement in forecast skill when initialized with sea ice thickness distribution information in late spring. However, other model systems show higher forecast skill when initialized with thickness distribution estimates from early summer (Section 6.1). Summer is a period when sea ice thickness measurements from satellite are traditionally unavailable in the

Arctic due to the presence of melt ponds (Section 3.4.2). Therefore a major aim of future work will be to further advance the CPOM UCL sea ice processor to identify radar returns from melt ponds, in addition to the current discrimination between lead, floe and open ocean returns. This will enable the provision of sea ice thickness and volume estimates during summer months.

7.2. Assessment of methods

The current sea ice processing method employed at CPOM UCL (Chapter 3) has been evaluated by comparing sea ice thickness estimates to independent estimates of sea ice thickness and draft acquired from airborne and ocean-based platforms (Section 4.3). CryoSat-2 estimates of ice thickness agree with these independent measurements to within 2 mm, on average – a difference that is much smaller than the accuracy of either dataset (10 to 40 cm). Whilst this in encouraging, it would be beneficial to quantify the certainty of point measurements of sea ice thickness. This is currently hampered by a lack of knowledge regarding the factors that contribute to the sea ice thickness calculation, such as snow depth and density, and sea ice density (Section 3.5). However, the evaluation of CryoSat-2 thickness data with independent data could be improved by using OIB and CryoVEx CryoSat-2 underflights and only gridding and comparing data that are exactly, or near exactly coincident. This will form the basis of future work. Sea ice volume estimates from CryoSat-2 display, qualitatively, many aspects of the observed variability in volume from the PIOMAS model (Section 4.5), including seasonal progression and the step increases in sea ice volume recorded in the autumns of 2013 and 2014. However, the discrepancy in growth rates, springtime volume, and inter-annual springtime volume variability between the two approaches requires further investigation. They key contributor to uncertainty in sea ice thickness and volume estimates is the snow load (Table 3.1). Each month, snow depth and snow density contribute an average of 10% and 6% to the total estimated sea ice volume error, respectively. Although these contributions are likely to be an overestimate (Section 3.5.1), a next step in Arctic sea ice research is to develop improved estimates of snow loading. The most comprehensive way to achieve this would be to develop a model of snow on Arctic sea ice, initialised with any available *in situ* data, or data from a reanalysis (Section 7.3.1). Reanalysis data is likely to be superior, due to the current lack of field measurements of snow depth and density over Arctic sea ice (Section 1.6.2 and Section 7.1).

To further develop the CPOM UCL sea ice processor it would be beneficial to investigate the impact of different gridding methods on the gridded archive and NRT sea ice thickness products. This could include the application of a distance weighting

rather than the equal weighting currently used (Section 3.5.1 and Section 6.2.2). In addition to improved estimates of the snow load on Arctic sea ice, the sea ice thickness and volume error budget could be further constrained with improved knowledge on uncertainties in sea ice density. Finally, the contribution of the uncertainty in the propagation speed of radar signals through the snow pack should be investigated, and accounted for in the thickness and volume error budgets. Whilst this is likely to be minimal in comparison to other parameters (Table 3.1), for transparency it is important to include all possible uncertainty factors in the error budget.

Whilst improving the CPOM UCL sea ice thickness algorithm, it is necessary to consider the potential limitations of the measurements made by the CryoSat-2 satellite. It has been suggested that ice thickness measurements from CryoSat-2 and other radar altimeter satellites become less reliable below ~0.5 m thickness. A solution could be to produce a blended dataset, by including microwave radiometer data such as those from MIRAS on-board the ESA SMOS satellite, which operates in the L-band at a frequency of 1.4 GHz (Section 1.6.2).

7.3. Further work

7.3.1. Development of a dynamic snow load

Arctic sea ice thickness and volume estimates from satellite radar altimetry will benefit from improved estimates of snow loading. As part of this project a time-varying snow load was derived from ERA-Interim climate reanalyses (Section 5.3.1 and Appendix A), to provide alternative estimates of the snow load on Arctic sea ice in the Amerasian and Eurasian basins (Figure 3.12). However, the time-varying snow load has not yet been applied across the entire Arctic, because the approach is complicated in regions of seasonal ice cover where the sea ice age, and therefore days of snow accumulation have to be taken into account. In future the time-varying snow load will be extended across the Northern Hemisphere by accounting for days of snow accumulation, using daily sea ice concentration data. Further considerations will include the movement of sea ice according to daily sea ice motion from Polar Pathfinder daily sea ice motion vectors (which have been available from NSIDC since mid-2016), air temperature from ERA-Interim reanalysis data, the redistribution of snow by wind, and the consideration of spatial variations in snow density.

7.3.2. Model assimilation of CryoSat-2 sea ice data

The NRT data presented in Chapter 6 provide a new resource and opportunity for the developers of short-term sea ice forecast models. These in turn can provide operational users with the information that they require regarding the state of the Arctic sea ice cover, such as sea ice location, drift speed and thickness (Section 1.4.3, Section 6.1 and Section 7.1). In addition to short-term forecast models, it is hoped that the archive data will be used as a validation tool for longer-term climate models (Section 1.5.2). It is these models that form the basis of future climate projections in the Arctic and globally, and can be used to investigate the influence of a changing Arctic sea ice cover on biological, physical and human aspects of the climate. For example, past model studies have shown that changes in the Arctic sea ice cover could impact on the climate in Europe, America and much of the Northern Hemisphere through, for example, an increase in heavy snowfall, or changes in evaporation and rainfall patterns (Section 1.3.1). For both short-term predictions and long-term climate modelling, it is important to consider the limitations of CryoSat-2 data for model assimilation. That a number of model systems show higher forecast or predictive skill when initialized with sea ice thickness estimates from summer months highlights the importance of working to expand satellite thickness observations into the melt season (Section 7.1). The utilisation of currently available sea ice observations for model development and analysis will form the basis of a meeting scheduled at the NCAR, Colorado in November 2016, with the theme of 'Sea Ice Thickness: Innovative strategies to integrate measurements and modeling'.

7.3.3. Investigation of radar propagation into the snow on sea ice

The projected continuation of Arctic temperature rise (Section 1.2.3) is likely to influence the properties of the snow cover on sea ice (Section 3.4.5). Increased melt and re-freezing of the snow will form icy layers, which could complicate radar returns. The influence of these icy layers on snow depth measurements and radar returns will need to be investigated in order to ensure accurate retrievals of sea ice freeboard and thickness from satellite radar altimeters. Relevant data has already been collected as part of ESA's CryoVEx 2014 campaign (Section 1.6.2), and will be analysed in the coming months.

7.3.4. Analysis of heritage and future satellite altimeter data

The CPOM UCL sea ice processor has in the past been used to estimate sea ice thickness from ERS-1 and -2, and Envisat satellite radar altimeter data in the central

Arctic. The developments of the processor made during this study provide the potential for extending these heritage observations beyond the central Arctic, to produce Northern Hemisphere sea ice thickness maps over a 25-year period with associated uncertainties. This is dependent on sufficient leads being resolved in heritage altimeter data (Section 2.4.2 and Figure 2.5). The development of a sea ice volume time series may be hindered by the reduced orbital coverage of earlier satellites at lower latitudes (Section 2.4.2 and Figure 2.5). The limitations of lead resolution and orbit spacing on the usefulness of heritage data will form the basis of future research.

The mean climatological snow load applied to CryoSat-2 sea ice data during this project could also be applied to data from NASA's ICESat laser altimeter satellite to extend its observations of Arctic sea ice thickness (Section 1.6.2) and volume (1.6.3) beyond the central Arctic (Figure 1.8). In addition, there should be a crossover period between CryoSat-2 and NASA's ICESat-2, which is due for launch in late-2017. An evaluation of the differences between ICESat and Envisat estimates of sea ice thickness, and ICESat-2 and CryoSat-2 estimates of sea ice thickness in autumn and spring (when ICESat data is available – see section 1.6.2) could be used, in conjunction with improved snow loading estimates, to assess the assumption that radar altimeter returns over Arctic sea ice are dominated by the snow-ice interface.

Radar propagation through the snow on Arctic sea ice could also be investigated through dual-frequency radar altimeter studies. For example, it has been shown that the effective scattering horizon of a Ka-band satellite radar altimeter is higher in the snow pack than that of the Ku-band CryoSat-2 radar [*Armitage and Ridout*, 2015]. However, the study was hindered by the limited spatial and temporal coincidence of the two satellite datasets and the difference in their footprint size. Dual-frequency radar returns would also provide a much-need insight into the interaction of radar signals with the more complex snow cover on Antarctic sea ice (Section 1.7). Future satellite missions would therefore benefit from a multi-instrument payload such as a dual-frequency radar altimeter, or a combination of radar and microwave or radar and laser capabilities. To understand how sea ice behaves basin-wide on decadal timescales, the continuation of satellite monitoring of the ice is crucial, as is the capability to continue and improve ice thickness retrievals.

Appendices

Appendix A. Efficacy of a climatological snow load

The reliability of using a climatological snow load in the CPOM UCL sea ice processing was investigated using the time-varying snow load described in Section 5.3.1. The climatological snow load was calculated from mean climatological snow depth and density values from *Warren et al*. [1999], which are described in Section 3.3.4. In this context snow load refers to the SWE, in mm of water equivalent (Section 5.3.1). Therefore the climatological snow load was calculated by dividing the product of the mean climatological snow depth and density for a given month, by seawater density (Equation (5.1)). The value used for seawater density has been a constant throughout this thesis (1023.9 kg m^{-3} from *Wadhams et al*. [1992]). The time-varying and climatological snow loads were compared in the Amerasian and Eurasian basins (Figure 3.12) to establish the extent to which they agree (Figure A.1).

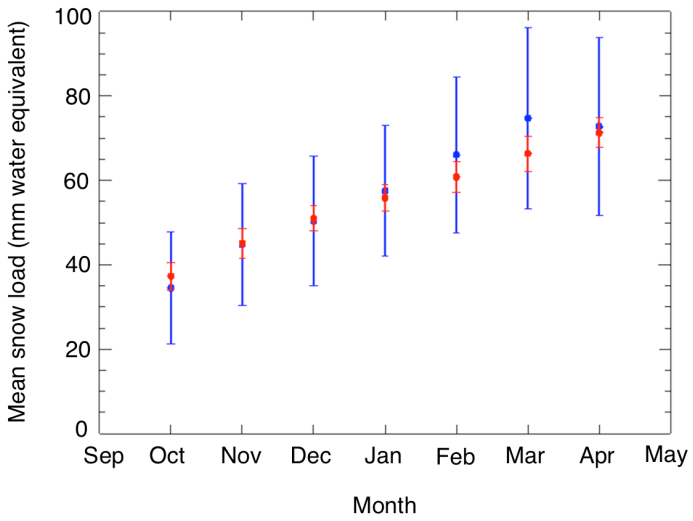

Figure A.1: Mean monthly snow load (in mm of water equivalent) on sea ice in the Amerasian and Eurasian basins. Snow load is determined from a climatology [*Warren et al*., 1999] (blue) and from a reanalysis of climate data [*Dee et al*., 2011] (red), for October 2010-November 2014. When computing the climatological snow load, the fraction of FYI and MYI in each month is accounted for. The vertical spread of each dataset illustrates the inter-annual variability of the data (± one standard deviations).

There is no significant difference between the two snow load datasets and, given their estimated uncertainties, the two datasets overlap. The uncertainties for both datasets are their inter-annual variability. For the climatological snow load this is calculated by converting the inter-annual variability in snow depth (which is described in Section

3.5.1) to SWE, using Equation (5.1). For the time-varying snow load this is calculated as the standard deviation in mean snow load for each month. Although the uncertainty of the reanalysis data set is smaller than that of the climatology, this is to be expected, as the climatological data are far more sparsely sampled (Section 3.5). The climatology and reanalyses data are independent from one another and, although this comparison does not eliminate the possibility that both datasets are similarly biased, it does suggest that they exhibit similar mean and temporal variability.

The time-varying snow load was also used to produce alternative estimates of Amerasian and Eurasian basin sea ice volume. In the Amerasian and Eurasian basins, there is only a small difference between sea ice volume calculated using the climatology-based retrieval and the reanalysis-based retrieval (Figure A.2), of 400 km^3 (< 5%) per month, on average. This comparison demonstrates that the use of a climatological snow load does not introduce any significant bias in the CryoSat-2 sea ice thickness retrieval, and does not appear to impact significantly on the temporal variability. However, the time-varying snow load has not yet been applied across the entire Arctic, because the approach is complicated in regions of seasonal ice cover where the sea ice age, and therefore days of snow accumulation have to be taken into

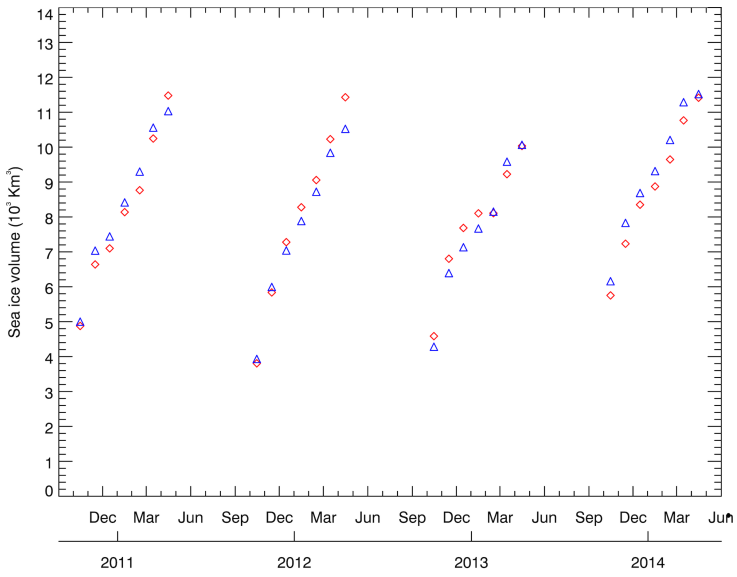

Figure A.2: The effect of snow load on CryoSat-2 sea ice volume estimates across the Amerasian and Eurasian basins. Volume estimates are produced using a climatological snow load (blue triangles), and a reanalysis-derived time-varying snow load (red diamonds). There is very little difference (a root-mean-square difference of < 5% per month) in sea ice volume using both methods.

account. The time-varying snow load and climatology should also be compared over smaller regions with high inter-annual variability in snowfall, to ensure that spatial variability in both snow loads is not being missed in the averaging.

Bibliography

Albritton, D. L., et al. (2001), Climate Change 2001: Synthesis Report, in *Contribution of Working Groups I, II, and III to the Third Assessment Report of the Intergovernmental Panel on Climate Change*, edited by R. T. Watson, pp. 1-398, Cambridge University Press, Cambridge, UK and New York, USA.

Alexander, M. A., U. S. Bhatt, J. E. Walsh, M. S. Timlin, J. S. Miller, and J. D. Scott (2004), The atmospheric response to realistic Arctic sea ice anomalies in an AGCM during winter, *Journal of Climate*, *17*(5), 890-905.

Alexandrov, V., S. Sandven, J. Wahlin, and O. M. Johannessen (2010), The relation between sea ice thickness and freeboard in the Arctic, *The Cryosphere*, *4*, 373-380.

Amstrup, S. C., E. T. DeWeaver, D. C. Douglas, B. G. Marcot, G. M. Durner, C. M. Bitz, and D. A. Bailey (2010), Greenhouse gas mitigation can reduce sea-ice loss and increase polar bear persistence, *Nature*, *468*(7326), 955-958.

Andersen, S., L.-A. Breivik, S. Eastwood, Ø. Godøy, T. Lavergne, M. Lind, M. Porcires, H. Schyberg, and R. Tonboe (2012), *Ocean and Sea Ice SAF, Sea Ice Product Manual, version 3.8, OSI SAF document no. SAF/OSI/met.no/TEC/MA/125*, 37 pp., EUMETSAT, Darmstadt, Germany.

Armitage, T. W. K., and M. Davidson (2014), Using the interferometric capabilities of the ESA CryoSat-2 mission to improve the accuracy of sea ice freeboard retrievals, *IEEE Transactions on Geoscience and Remote Sensing*, *52*(1), 529-536.

Armitage, T. W. K., and A. Ridout (2015), Arctic sea ice freeboard from AltiKa and comparison with CryoSat-2 and Operation IceBridge, *Geophysical Research Letters*, *42*(16), 6724-6731.

Arrigo, K. R., G. L. van Dijken, and S. Pabi (2008), Impact of a shrinking Arctic ice cover on marine primary production, *Geophysical Research Letters*, *35*(19), L19603.

Arrigo, K. R., et al. (2012), Massive Phytoplankton Blooms Under Arctic Sea Ice, *Science*, *336*(6087), 1408-1408.

Atlas, D., R. C. Beal, R. A. Brown, P. Demey, R. K. Moore, C. G. Rapley, and C. T. Swift (1986), Problems and future directions in remote sensing of the oceans and troposphere - A workshop report, *Journal of Geophysical Research-Oceans*, *91*(C2), 2525-2548.

Beaven, S. G., G. L. Lockhart, S. P. Gogineni, A. R. Hossetnmostafa, K. Jezek, A. J. Gow, D. K. Perovich, A. K. Fung, and S. Tjuatja (1995), Laboratory measurements of radar backscatter from bare and snow-covered saline ice sheets, *International Journal of Remote Sensing*, *16*(4), 851-876.

Beckers, J. F., C. Haas, B. C. Elder, C. Hiemstra, R. L. Tilling, and T. W. K. Armitage (2015), *CryoVEx2014 - In-situ measurements at MIZ/ONR and NORD (Greenland) ice camps, ESA Ground Team Report, ESA contract no. 4000110552/14/MP/vb*, 46 pp.

Behrendt, A., W. Dierking, E. Fahrbach, and H. Witte (2013), Sea ice draft in the Weddell Sea, measured by upward looking sonars, *Earth System Science Data*, *5*(1), 209-226.

Belt, S. T., and J. Mueller (2013), The Arctic sea ice biomarker IP25: a review of current understanding, recommendations for future research and applications in palaeo sea ice reconstructions, *Quaternary Science Reviews*, *79*, 9-25.

Belt, S. T., G. Masse, S. J. Rowland, M. Poulin, C. Michel, and B. LeBlanc (2007), A novel chemical fossil of palaeo sea ice: IP25, *Organic Geochemistry*, *38*(1), 16-27.

Bergthorsson, P. (1969), An estimate of drift ice and temperature in Iceland in 1000 years, *Jökull*, *19*, 94-101.

Bertino, L., and K. A. Lisaeter (2008), The TOPAZ monitoring and prediction system for the Atlantic and Arctic Oceans, *Journal of Operational Oceanography*, *1*(2), 15-18.

Bindoff, N. L., et al. (2013), Detection and attribution of climate change: From global to regional, in *Climate Change 2013: The Physical Science Basis. Contribution of Working Group I to the Fifth Assessment Report of the Intergovernmental Panel on Climate Change* edited by T. F. Stocker, D. Qin, G.-K. Plattner, M. Tignor, S. K. Allen, J. Boschung, A. Nauels, Y. Xia, V. Bex and P. M. Midgley, pp. 867-952, Cambridge, UK and New York, USA.

Bintanja, R., G. J. Van Oldenborgh, and C. A. Katsman (2015), The effect of increased fresh water from Antarctic ice shelves on future trends in Antarctic sea ice, *Annals of Glaciology*, *56*(69), 120-126.

Blake Jr, W. (1975), Radiocarbon Age Determinations and Postglacial Emergence at Cape Storm, Southern Ellesmere Island, Arctic Canada, *Geografiska Annaler. Series A, Physical Geography*, *57*(1), 1-71.

Broecker, W. S. (1997), Thermohaline circulation, the Achilles heel of our climate system: Will man-made CO2 upset the current balance?, *Science*, *278*(5343), 1582-1588.

Brown, G. S. (1977), The average impulse response of a rough surface and its applications, *Ieee Transactions on Antennas and Propagation*, *25*(1), 67-74.

Cavalieri, D. J., C. L. Parkinson, P. Gloersen, and H. J. Zwally (1996, updated yearly), Sea ice concentrations from Nimbus-7 SMMR and DMSP SSM/I-SSMIS passive microwave data [concentration], edited, NASA DAAC at the National Snow and Ice Data Center, Boulder, Colorado, USA.

Cavalieri, D. J., C. L. Parkinson, P. Gloersen, J. C. Comiso, and H. J. Zwally (1999), Deriving long-term time series of sea ice cover from satellite passive-microwave multisensor data sets, *Journal of Geophysical Research-Oceans*, *104*(C7), 15803-15814.

Cavalieri, D. J., et al. (1992), *NASA Sea Ice Validation Program for the DMSP SSM/I: Final Report, NASA Technical Memorandum 104559*, 112 pp., National Aeronautics and Space Administration, Washington, D. C., USA.

Chapman, W. L., and NCAR (2013), The Climate Data Guide: Walsh and Chapman Northern Hemisphere Sea Ice, edited, guide available at https://climatedataguide.ucar.edu/climate-data/walsh-and-chapman-northern-hemisphere-sea-ice.

Chelton, D. B., J. C. Ries, B. J. Haines, L.-L. Fu, and P. S. Callahan (2001), Satellite Altimetry, in *Satellite Altimetry and Earth Sciences*, edited by L.-L. Fu and A. Cazenave, pp. 1-131, Academic Press, London, UK and San Diego, USA.

Chevallier, M., and D. Salas-Melia (2012), The Role of Sea Ice Thickness Distribution in the Arctic Sea Ice Potential Predictability: A Diagnostic Approach with a Coupled GCM, *Journal of Climate*, *25*(8), 3025-3038.

Chylek, P., N. Hengartner, G. Lesins, J. D. Klett, O. Humlum, M. Wyatt, and M. K. Dubey (2014), Isolating the anthropogenic component of Arctic warming, *Geophysical Research Letters*, *41*(10), 3569-3576.

CMEMS (2014), *Marine Environment Monitoring Service (Copernicus), available at* http://www.copernicus.eu/sites/default/files/documents/Copernicus_Factsheets/Copernicus_MarineEnvironmentMonitoring_May2015.pdf, 2 pp., European Commission Vincennes, France.

Collins, M., et al. (2013), Long-term Climate Change: Projections, Commitments and Irreversibility, in *Climate Change 2013: The Physical Science Basis. Contribution of Working Group I to the Fifth Assessment Report of the Intergovernmental Panel on Climate Change* edited by T. F. Stocker, D. Qin, G.-K. Plattner, M. Tignor, S. K. Allen, J. Boschung, A. Nauels, Y. Xia, V. Bex and P. M. Midgley, pp. 1029-1136, Cambridge, UK and New York, USA.

Comiso, J. C. (2000, updated 2015), Bootstrap Sea Ice Concentrations from Nimbus-7 SMMR and DMSP SSM/I-SSMIS, Version 2 [concentration], edited, NASA DAAC at that National Snow and Ice Data Center, Boulder, Colorado USA.

Comiso, J. C., and R. Kwok (1996), Surface and radiative characteristics of the summer Arctic sea ice cover from multisensor satellite observations, *Journal of Geophysical Research-Oceans*, *101*(C12), 28397-28416.

Comiso, J. C., D. J. Cavalieri, C. L. Parkinson, and P. Gloersen (1997), Passive microwave algorithms for sea ice concentration: A comparison of two techniques, *Remote Sensing of Environment*, *60*(3), 357-384.

Cronin, T. M., S. A. Smith, F. Eynaud, M. O'Regan, and J. King (2008), Quaternary paleoceanography of the central arctic based on Integrated Ocean Drilling Program Arctic Coring Expedition 302 foraminiferal assemblages, *Paleoceanography*, *23*(1), Pa1s18.

Cronin, T. M., T. R. Holtz, R. Stein, R. Spielhagen, D. Futterer, and J. Wollenburg (1995), Late Quaternary paleoceanography of the Eurasian Basin, Arctic Ocean, *Paleoceanography*, *10*(2), 259-281.

Curlander, J. C., and R. N. McDonough (1991), *Synthetic Aperture Radar: Systems and Signal Processing*, 672 pp., John WIley & Sons, Inc., New York, USA.

Curran, P. J. (1985), *Principles of Remote Sensing*, 260 pp., Longman Group Limited, New York, USA.

Curry, J. A., J. L. Schramm, and E. E. Ebert (1995), Sea-ice albedo climate feedback mechanism, *Journal of Climate*, *8*(2), 240-247.

Day, J. J., S. Tietsche, and E. Hawkins (2014), Pan-Arctic and regional sea ice predictability: Initialization month dependence, *Journal of Climate*, *27*(12), 4371-4390.

de Vernal, A., C. Hillaire-Marcel, S. Solignac, T. Radi, and A. Rochon (2008), Reconstructing Sea Ice Conditions in the Arctic and Sub-Arctic Prior to Human Observations, in *Arctic Sea Ice Decline: Observations, Projections, Mechanisms, and Implications*, edited by E. T. DeWeaver, C. M. Bitz and L. B. Tremblay, pp. 27-45.

Dee, D. P., S. M. Uppalaa, A. J. Simmonsa, P. Berrisforda, P. Polia, S. Kobayashib, U. Andraec, M. A. Balmasedaa, G. Balsamoa, and e. al (2011), The ERA-Interim reanalysis: Configuration and performance of the data assimilation system, *Quarterly Journal of the Royal Meteorological Society*, *137*(656), 553-597.

Desaubies, Y. (2006), Mersea: Development of a European ocean monitoring and forecasting system - Ocean and marine applications for GMES, in *Ocean Weather Forecasting: An Integrated View of Oceanography*, edited by E. P. Chassignet and J. Verron, pp. 449-453.

Dethloff, K., et al. (2006), A dynamical link between the Arctic and the global climate system, *Geophysical Research Letters*, *33*(3), L03703.

Doherty, T. J., and S. Clayton (2011), The Psychological Impacts of Global Climate Change, *American Psychologist*, *66*(4), 265-276.

Drevillon, M., et al. (2008), The GODAE/Mercator-Ocean global ocean forecasting system: results, applications and prospects, *Journal of Operational Oceanography*, *1*(1), 51-57.

Drinkwater, M. R. (1991), Ku band airborne radar altimeter observations of marginal sea ice during the 1984 marginal ice-zone experiment, *Journal of Geophysical Research-Oceans*, *96*(C3), 4555-4572.

Drinkwater, M. R., C. R. Francis, G. Ratier, and D. J. Wingham (2004), The European Space Agency's Earth Explorer Mission CryoSat: Measuring Variability in the Cryosphere, *Annals of Glaciology*, *39*, 313-320.

Durkalec, A., C. Furgal, M. W. Skinner, and T. Sheldon (2015), Climate change influences on environment as a determinant of Indigenous health: Relationships to place, sea ice, and health in an Inuit community, *Social Science & Medicine*, *136*, 17-26.

Dyke, A. S., J. Hooper, and J. M. Savelle (1996), A history of sea ice in the Canadian Arctic Archipelago based on postglacial remains of the bowhead whale (Balaena mysticetus), *Arctic*, *49*(3), 235-255.

Dyke, A. S., J. Hooper, C. R. Harington, and J. M. Savelle (1999), The Late Wisconsinan and Holocene record of walrus (Odobenus rosmarus) from North America: A review with new data from Arctic and Atlantic Canada, *Arctic*, *52*(2), 160-181.

Ebert, E. E., and J. A. Curry (1993), An intermediate one-dimensional thermodynamic sea-ice model for investigating ice-atmosphere interactions, *Journal of Geophysical Research-Oceans*, *98*(C6), 10085-10109.

Eggertsson, O. (1993), Origin of the driftwood on the coasts of Iceland: A dendrochronological study, *Jökull*, *43*, 15-32.

Eisenman, I., N. Untersteiner, and J. S. Wettlaufer (2007), On the reliability of simulated Arctic sea ice in global climate models, *Geophysical Research Letters*, *34*(10), L10501.

Eppler, D. T., L. D. Farmer, and A. W. Lohanick (1992), Passive microwave signatures of sea ice, in *Microwave Remote Sensing of Sea Ice*, edited by F. D. Carsey, pp. 47-72, American Geophysical Union, Washington D.C., USA.

ESA/MSSL (2013), *CryoSat Product Handbook*, 103 pp., ESRIN, ESA and Mullard Space Science Laboratory/University College London Frascati, Italy and Surrey, UK.

ESA/UCL (2001), *CryoSat Data Processing Concept, ESA document no. CS-PL-UCL-SY-0005*, 12 pp., University College London, London, UK.

Farrell, S. L., N. Kurtz, L. N. Connor, B. C. Elder, C. J. Leuschen, T. Markus, D. C. McAdoo, B. Panzer, J. Richter-Menge, and J. G. Sonntag (2012), A first assessment of IceBridge snow and ice thickness data over Arctic sea ice, *Ieee Transactions on Geoscience and Remote Sensing*, *50*(6), 2098-2111.

Feltham, D. L. (2008), Sea ice rheology, *Annual Review of Fluid Mechanics*, *40*, 91-112.

Femenias, P., R. Raizonville, and J. F. Minster (1993a), Analysis of satellite-altimeter height measureInents above continental ice sheets, *Journal of Glaciology*, *39*(133), 591-600.

Femenias, P., F. Remy, R. Raizonville, and J. F. Minster (1993b), Analysis of satellite-altimeter height measurements above continental ice sheets, *Journal of Glaciology*, *39*(133), 591-600.

Ferreira, D., J. Marshall, C. M. Bitz, S. Solomon, and A. Plumb (2015), Antarctic Ocean and Sea Ice Response to Ozone Depletion: A Two-Time-Scale Problem, *Journal of Climate*, *28*(3), 1206-1226.

Fetterer, F., K. Knowles, W. Meier, and M. Savoie (2002, updated daily), Sea Ice Index [index], edited, National Snow and Ice Data Center - Digital Media, Boulder, Colorado, USA.

Fetterer, F., M. R. Drinkwater, K. Jezek, S. Laxon, R. Onstott, and L. M. H. Ulander (1992), Sea Ice Altimetry, in *Microwave Remote Sensing of Sea Ice*, edited by F. D. Carsey, pp. 111-136, American Geophysical Union, Washington DC, USA.

Flato, G. M., and R. D. Brown (1996), Variability and climate sensitivity of landfast Arctic sea ice, *Journal of Geophysical Research-Oceans*, *101*(C11), 25767-25777.

Flocco, D., D. L. Feltham, and A. K. Turner (2010), Incorporation of a physically based melt pond scheme into the sea ice component of a climate model, *Journal of Geophysical Research-Oceans*, *115*, C08012.

Francis, C. R. (2007), *CryoSat Mission and Data Description; ESA document no. CS-RP-ESA-SY-0059 issue 3.0*, 82 pp., ESTEC, Noordwijk, Holland.

Francis, J. A., and S. Vavrus (2012), Evidence linking Arctic amplification to extreme weather in mid-latitudes, *Geophysical Research Letters*, *39*(6), L06801.

Francis, J. A., and N. Skific (2015), Evidence linking rapid Arctic warming to mid-latitude weather patterns, *Philosophical Transactions of the Royal Society a-Mathematical Physical and Engineering Sciences*, *373*(2045), 20140170.

Francis, J. A., W. Chan, D. J. Leathers, J. R. Miller, and D. E. Veron (2009), Winter Northern Hemisphere weather patterns remember summer Arctic sea-ice extent, *Geophysical Research Letters*, *36*(7), L07503.

Fu, L.-L., and A. Cazenave (2000), *Satellite altimetry and Earth Sciences: A handbook of techniques and applications*, 463 pp., Academic Press, San Diego, USA.

Galley, R. J., B. G. T. Else, S. J. Prinsenberg, D. Babb, and D. G. Barber (2013), Summer sea ice concentration, motion, and thickness near areas of proposed offshore oil and gas development in the Canadian Beaufort Sea - 2009, *Arctic*, *66*(1), 105-116.

Giles, K. A., S. W. Laxon, and A. L. Ridout (2008a), Circumpolar thinning of Arctic sea ice following the 2007 record ice extent minimum, *Geophysical Research Letters*, *35*(22), L22502.

Giles, K. A., S. W. Laxon, and A. P. Worby (2008b), Antarctic sea ice elevation from satellite radar altimetry, *Geophysical Research Letters*, *35*(3), L03503.

Giles, K. A., S. Laxon, A. Ridout, D. J. Wingham, and S. Bacon (2012), Western Arctic Ocean freshwater storage increased by wind-driven spin-up of the Beaufort Gyre, *Nature Geoscience*, *5*, 194-197.

Giles, K. A., S. W. Laxon, D. J. Wingham, D. W. Wallis, W. B. Krabill, C. J. Leuschen, D. McAdoo, S. S. Manizade, and R. K. Raney (2007), Combined airborne laser and radar altimeter measurements over the Fram Strait in May 2002, *Remote Sensing of Environment*, *111*(2-3), 182-194.

Gillett, N. P., D. A. Stone, P. A. Stott, T. Nozawa, A. Y. Karpechko, G. C. Hegerl, M. F. Wehner, and P. D. Jones (2008), Attribution of Polar warming to human influence, *Nature Geoscience*, *1*(11), 750-754.

GISTEMP (2015), GISS Surface Temperature Analysis (GISTEMP), edited, NASA Goddard Institute for Space Studies, data available at http://data.giss.nasa.gov/gistemp/.

GODAE (2008), *Global Ocean Data Assimilation Experiment: Observing and Forecasting the Oceans*, 7 pp., GODAE Project Office, Exeter, UK.

Goosse, H. (2015), *Climate System Dynamics and Modelling*, 273 pp., Cambridge University Press, New York, USA.

Gossett, J. (1996), Arctic research using nuclear submarines, *Sea Technology*, *37*(3), 33-40.

Graversen, R. G., and M. Wang (2009), Polar amplification in a coupled climate model with locked albedo, *Climate Dynamics*, *33*(5), 629-643.

Graversen, R. G., P. L. Langen, and T. Mauritsen (2014), Polar Amplification in CCSM4: Contributions from the Lapse Rate and Surface Albedo Feedbacks, *Journal of Climate*, *27*(12), 4433-4450.

Grebmeier, J. M., J. E. Overland, S. E. Moore, E. V. Farley, E. C. Carmack, L. W. Cooper, K. E. Frey, J. H. Helle, F. A. McLaughlin, and S. L. McNutt (2006), A major ecosystem shift in the northern Bering Sea, *Science*, *311*(5766), 1461-1464.

Haas, C., J. Lobach, S. Hendricks, L. Rabenstein, and A. Pfaffling (2009), Helicopter-borne measurements of sea ice thickness, using a small and lightweight, digital EM system, *Journal of Applied Geophysics*, *67*(3), 234-241.

Haggblom, A. (1982), Driftwood in Svalbard as an indicator of sea ice conditions - A preliminary report, *Geografiska Annaler Series a-Physical Geography*, *64*(1-2), 81-94.

Hansen, J., R. Ruedy, M. Sato, and K. Lo (2010), Global surface temperature change, *Reviews of Geophysics*, *48*, Rg4004.

Harsem, O., A. Eide, and K. Heen (2011), Factors influencing future oil and gas prospects in the Arctic, *Energy Policy*, *39*(12), 8037-8045.

Hartmann, D. L., A. M. G. Klein Tank, M. Rusticucci, L. V. Alexander, S. Bronnimann, Y. Charabi, and F. J. Dentener (2013), Observations: Atmosphere and Surface, in *Climate Change 2013: The Physical Science Basis. Contribution of Working Group I to the Fifth Assessment Report of the Intergovernmental Panel on Climate Change*, edited by T. F. Stocker, D. Qin, G.-K. Plattner, M. Tignor, S. K. Allen, J. Boschung, A. Nauels, Y. Xia, V. Bex and P. M. Midgley, pp. 159-254, Cambridge, UK and New York, USA.

Hebert, D. A., R. A. Allard, E. J. Metzger, P. G. Posey, R. H. Preller, A. J. Wallcraft, M. W. Phelps, and O. M. Smedstad (2015), Short-term sea ice forecasting: An assessment of ice concentration and ice drift forecasts using the US Navy's Arctic Cap Nowcast/Forecast System, *Journal of Geophysical Research-Oceans*, *120*(12), 8327-8345.

Helm, V., A. Humbert, and H. Miller (2014), Elevation and elevation change of Greenland and Antarctica derived from CryoSat-2, *The Cryosphere*, *8*, 1539-1559.

Hock, R., and B. Holmgren (2005), A distributed surface energy-balance model for complex topography and its application to Storglaciaren, Sweden, *Journal of Glaciology*, *51*(172), 25-36.

Holland, M. M., C. M. Bitz, and A. J. Weaver (2001), The influence of sea ice physics on simulations of climate change *Journal of Geophysical Research*, *106*(C9), 19639-19655

Holland, M. M., M. C. Serreze, and J. C. Stroeve (2010), The sea ice mass budget of the Arctic and its future change as simulated by coupled climate models, *Climate Dynamics*, *34*(2-3), 185-200.

Hunke, E. C. (2010), Thickness sensitivities in the CICE sea ice model, *Ocean Modelling*, *34*(3-4), 137-149.

Hunke, E. C. (2014), Sea ice volume and age: Sensitivity to physical parameterizations and thickness resolution in the CICE sea ice model, *Ocean Modelling*, *82*, 45-59.

Hunke, E. C., W. H. Lipscomb, A. K. Turner, N. Jeffery, and S. Elliott (2015), *CICE: the Los Alamos Sea Ice Model Documentation and Software User's Manual Version 5.1*, 116 pp., Los Alamos National Laboratory, Los Alamos, USA.

Hunter, C. M., H. Caswell, M. C. Runge, E. V. Regehr, S. C. Amstrup, and I. Stirling (2010), Climate change threatens polar bear populations: a stochastic demographic analysis, *Ecology*, *91*(10), 2883-2897.

Hurrell, J. W. (1995), Decadal trends in North-Atlantic Oscillation - Regional temperatures and precipitation, *Science*, *269*(5224), 676-679.

IACS (2016), *International Association of Classification Societies - Requirements concerning Polar Class*, 16 pp.

Intrieri, J. M., C. W. Fairall, M. D. Shupe, P. O. G. Persson, E. L. Andreas, P. S. Guest, and R. E. Moritz (2002), An annual cycle of Arctic surface cloud forcing at SHEBA, *Journal of Geophysical Research-Oceans*, *107*(C10), 8039.

Jensen, J. R. (1999), Angle measurement with a phase monopulse radar altimeter, *Ieee Transactions on Antennas and Propagation*, *47*(4), 715-724.

Kaleschke, L., X. Tian-Kunze, N. Maass, M. Makynen, and M. Drusch (2012), Sea ice thickness retrieval from SMOS brightness temperatures during the Arctic freeze-up period, *Geophysical Research Letters*, *39*, L05501.

Kelly, P. M., C. M. Goodess, and B. S. G. Cherry (1987), The interpretation of the Icelandic sea ice record, *Journal of Geophysical Research-Oceans*, *92*(C10), 10835-10843.

Kern, S., K. Khvorostovsky, H. Skourup, E. Rinne, Z. S. Parsakhoo, V. Djepa, P. Wadhams, and S. Sandven (2015), The impact of snow depth, snow density and ice density on sea ice thickness retrieval from satellite radar altimetry: results from the ESA-CCI Sea Ice ECV Project Round Robin Exercise, *Cryosphere*, *9*(1), 37-52.

Kinnard, C., C. M. Zdanowicz, D. A. Fisher, E. Isaksson, A. de Vernal, and L. G. Thompson (2011), Reconstructed changes in Arctic sea ice over the past 1,450 years, *Nature*, *479*(7374), 509-512.

Kirtman, B., et al. (2013), Near-term Climate Change: Projections and Predictability, in *Climate Change 2013: The Physical Science Basis. Contribution of Working Group I to the Fifth Assessment Report of the Intergovernmental Panel on Climate Change* edited

by T. F. Stocker, D. Qin, G.-K. Plattner, M. Tignor, S. K. Allen, J. Boschung, A. Nauels, Y. Xia, V. Bex and P. M. Midgley, pp. 953-1028, Cambridge, UK and New York, USA.

Koch, L. (1945), The East Greenland ice, *Meddelelser Om Gronland 130*(3), 1-375.

Ku, H. H. (1966), Notes on the use of propagation of error formulas, *Journal of Research of the National Bureau of Standars - C. Enginering and Instrumentation*, *70C*(4), 263-273.

Kurtz, N. T., and S. L. Farrell (2011), Large-scale surveys of snow depth on Arctic sea ice from Operation IceBridge, *Geophysical Research Letters*, *38*(20), L20505.

Kurtz, N. T., and T. Markus (2012), Satellite observations of Antarctic sea ice thickness and volume, *Journal of Geophysical Research-Oceans*, *117*, C08025.

Kurtz, N. T., N. Galin, and M. Studinger (2014), An improved CryoSat-2 sea ice freeboard retrieval algorithm through the use of waveform fitting, *The Cryosphere*, *8*, 1217-1237.

Kurtz, N. T., T. Markus, S. L. Farrell, D. L. Worthen, and L. N. Boisvert (2011), Observations of recent Arctic sea ice volume loss and its impact on ocean-atmosphere energy exchange and ice production, *Journal of Geophysical Research-Oceans*, *116*(C4), C04015.

Kurtz, N. T., S. L. Farrell, M. Studinger, N. Galin, J. P. Harbeck, R. Lindsay, V. D. Onana, B. Panzer, and J. G. Sonntag (2013), Sea ice thickness, freeboard, and snow depth products from Operation IceBridge airborne data, *The Cryosphere*, *7*(4), 1035-1056.

Kwok, R. (2004), Annual cycles of multiyear sea ice coverage of the Arctic Ocean: 1999-2003, *Journal of Geophysical Research-Oceans*, *109*(C11), C11004.

Kwok, R. (2007), Near zero replenishment of the Arctic multiyear sea ice cover at the end of 2005 summer, *Geophysical Research Letters*, *34*(5), L05501.

Kwok, R. (2011), Observational assessment of Arctic Ocean sea ice motion, export, and thickness in CMIP3 climate simulations, *Journal of Geophysical Research-Oceans*, *116*, C00d05.

Kwok, R., and D. A. Rothrock (2009), Decline in Arctic sea ice thickness from submarine and ICESat records: 1958-2008, *Geophysical Research Letters*, *36*(15), L15501.

Kwok, R., and J. Morison (2011), Dynamic topography of the ice-covered Arctic Ocean from ICESat, *Geophysical Research Letters*, *38*(2), L02501-02501 - L02501-02506.

Kwok, R., and G. F. Cunningham (2015), Variability of Arctic sea ice thickness and volume from CryoSat-2, *Philosophical Transactions of the Royal Society A-Mathematical Physical and Engineering Sciences*, *373*(2045), 20140157.

Kwok, R., G. Spreen, and S. Pang (2013), Arctic sea ice circulation and drift speed: Decadal trends and ocean currents, *Journal of Geophysical Research-Oceans*, *118*(5), 2408-2425.

Kwok, R., G. F. Cunningham, H. J. Zwally, and D. Yi (2007), Ice, Cloud, and land Elevation Satellite (ICESat) over Arctic sea ice: Retrieval of freeboard, *Journal of Geophysical Research-Oceans*, *112*(C12), C12013.

Kwok, R., G. F. Cunningham, M. Wensnahan, I. Rigor, H. J. Zwally, and D. Yi (2009), Thinning and volume loss of the Arctic Ocean sea ice cover: 2003-2008, *Journal of Geophysical Research-Oceans*, *114*(C7), C07005.

Kwok, R., B. Panzer, C. Leuschen, S. Pang, T. Markus, B. Holt, and S. Gogineni (2011), Airborne surveys of snow depth over Arctic sea ice, *Journal of Geophysical Research-Oceans*, *116*, C11018.

Laidre, K. L., I. Stirling, L. F. Lowry, O. Wiig, M. P. Heide-Jorgensen, and S. H. Ferguson (2008), Quantifying the sensitivity of arctic marine mammals to climate-induced habitat change, *Ecological Applications*, *18*(2), S97-S125.

Lavergne, T. (2015), *Ocean & Sea Ice SAF - Algorithm Theoretical Basis Document for the OSI SAF Low Resolution Sea Ice Drift Product, version 1.2. OSI SAF document no. SAF/OSI/CDOP/met.no/SCI/MA/130*, 37 pp., OSI SAF, Darmstadt, Germany.

Laxon, S. (1994), Sea ice altimeter processing scheme at the EODC, *International Journal of Remote Sensing*, *15*(4), 915-924.

Laxon, S., and C. G. Rapley (1987), Radar altimeter data quality flagging, *Advances in Space Research*, *7*(11), 315-318.

Laxon, S., N. Peacock, and D. Smith (2003), High interannual variability of sea ice thickness in the Arctic region, *Nature*, *425*(6961), 947-950.

Laxon, S., et al. (2013), CryoSat-2 estimates of Arctic sea ice thickness and volume, *Geophysical Research Letters*, *40*(4), 732-737.

Levermann, A., J. Mignot, S. Nawrath, and S. Rahmstorf (2007), The role of Northern sea ice cover for the weakening of the thermohaline circulation under global warming, *Journal of Climate*, *20*(16), 4160-4171.

Lindsay, R., M. Wensnahan, A. Schweiger, and J. Zhang (2014), Evaluation of Seven Different Atmospheric Reanalysis Products in the Arctic, *Journal of Climate*, *27*(7), 2588-2606.

Lindsay, R. W., and J. Zhang (2005), The thinning of Arctic sea ice, 1988-2003: Have we passed a tipping point?, *Journal of Climate*, *18*(22), 4879-4894.

Lindsay, R. W., C. Haas, S. Hendricks, P. Hunkeler, N. Kurtz, J. Paden, B. Panzer, J. Sonntag, J. Yungel, and J. Zhang (2012), Seasonal forecasts of Arctic sea ice initialized with observations of ice thickness, *Geophysical Research Letters*, *39*, L21502.

Liu, J., J. A. Curry, H. J. Wang, M. Song, and R. M. Horton (2012), Impact of declining Arctic sea ice on winter snowfall, *Proceedings of the National Academy of Sciences of the United States of America*, *109*(11), 4074-4079.

Liu, M., and J. Kronbak (2010), The potential economic viability of using the Northern Sea Route (NSR) as an alternative route between Asia and Europe, *Journal of Transport Geography*, *18*(3), 434-444.

Lohmann, G., and R. Gerdes (1998), Sea ice effects on the sensitivity of the thermohaline circulation, *Journal of Climate*, *11*(11), 2789-2803.

Maksym, T., and M. O. Jeffries (2000), A one-dimensional percolation model of flooding and snow ice formation on Antarctic sea ice, *Journal of Geophysical Research-Oceans*, *105*(C11), 26313-26331.

Marquardt, D. W. (1963), An algorithm for least-squares estimation of nonlinear parameters *Journal of the Society for Industrial and Applied Mathematics 11*(2), 431-441.

Martin, T., M. Tsamados, D. Schroeder, and D. L. Feltham (2016), The impact of variable sea ice roughness on changes in Arctic Ocean surface stress: A model study, *Journal of Geophysical Research-Oceans*, *121*(3), 1931-1952.

Maslanik, J., and J. C. Stroeve (1999, updated daily), Near-Real-Time DMSP SSM/I-SSMIS daily polar gridded sea ice concentrations [concentration], edited, NASA DAAC at the National Snow and Ice Data Center - Digital Media, Boulder, Colorado, USA.

Massom, R. A., and D. Lubin (2006), *Polar Remote Sensing: Volume II: Ice Sheets*, 426 pp., Springer Science & Business Media, Chichester, UK.

Massom, R. A., V. I. Lytle, A. P. Worby, and I. Allison (1998), Winter snow cover variability on East Antarctic sea ice, *Journal of Geophysical Research-Oceans*, *103*(C11), 24837-24855.

Massom, R. A., et al. (2001), Snow on Antarctic Sea ice, *Reviews of Geophysics*, *39*(3), 413-445.

McBean, G., G. V. Alekseev, D. Chen, E. Forland, J. C. Fyfe, P. Y. Groisman, R. King, H. Melling, R. S. Vose, and P. H. Whitfield (2004), Arctic Climate: Past and Present, in *Arctic: Arctic Climate Impact Assessment*, edited by C. Symon, L. Arris and H. B., pp. 21-60, Cambridge University Press, New York, USA.

McCandles Jr, S. W., and C. R. Jackson (2004), Principle of Synthetic Aperture Radar, in *Synthetic Aperture Radar Marine User's Manual*, edited by C. R. Jackson and J. R. Apel, pp. 1-24, U.S. Department of Commerce/NOAA, Washington, D.C., USA.

McLaren, A. S. (1989), The under-ice thickness distribution of the Arctic Basin as recorded in 1958 and 1970 *Journal of Geophysical Research-Oceans*, *94*(C4), 4971-4983.

McLaren, A. S., J. E. Walsh, R. H. Bourke, R. L. Weaver, and W. Wittmann (1992), Variability in sea-ice thickness over the North Pole from 1977 to 1990, *Nature*, *358*(6383), 224-226.

McMillan, M., A. Shepherd, A. Sundal, K. Briggs, A. Muir, A. Ridout, A. Hogg, and D. J. Wingham (2014), Increased ice losses from Antarctica detected by CryoSat-2, *Geophysical Research Letters*, *41*(11), 3899–3905.

Meehl, G. A., R. Moss, K. E. Taylor, V. Eyring, R. J. Stouffer, S. Bony, and B. Stevens (2014), Climate model intercomparisons: Preparing for the next phase, *Eos Transactions of the American Geophysical Union*, *95*(9), 77-78.

Meehl, G. A., C. Covey, T. Delworth, M. Latif, B. McAvaney, J. F. B. Mitchell, R. J. Stouffer, and K. E. Taylor (2007), The WCRP CMIP3 multimodel dataset: A new era in climate change research, *Bulletin of the American Meteorological Society*, 1383-1394.

Meier, W. N., et al. (2014), Arctic sea ice in transformation: A review of recent observed changes and impacts on biology and human activity, *Reviews of Geophysics*, *52*(3), 185-217.

Melling, H., P. H. Johnston, and D. A. Riedel (1995), Measurements of the underside topography of sea-ice by moored subsea sonar, *Journal of Atmospheric and Oceanic Technology*, *12*(3), 589-602.

Morice, C. P., J. J. Kennedy, N. A. Rayner, and P. D. Jones (2012), Quantifying uncertainties in global and regional temperature change using an ensemble of observational estimates: The HadCRUT4 data set, *Journal of Geophysical Research-Atmospheres*, *117*, D08101.

Najafi, M. R., F. W. Zwiers, and N. P. Gillett (2015), Attribution of Arctic temperature change to greenhouse-gas and aerosol influences, *Nature Climate Change*, *5*(3), 246-249.

Navy (2014), *U.S. Navy Arctic Roadmap 2014-2030*, 43 pp., CreateSpace Publishing, Washington, D.C., USA.

NOAA (2016), Arctic Oscillation Index, edited, National Oceanic and Atmospheric Administration, data available at https://http://www.ncdc.noaa.gov/teleconnections/ao/.

Notz, D. (2012), Challenges in simulating sea ice in Earth System Models, *Wiley Interdisciplinary Reviews-Climate Change*, *3*(6), 509-526.

NSIDC (2015), Near-Real-Time DMSP SSMIS Daily Polar Gridded Sea Ice Concentrations, edited, data available at https://nsidc.org/data/docs/daac/nsidc0081_ssmi_nrt_seaice.gd.html#doc_info.

Nurser, A. J. G., and S. Bacon (2014), The Rossby radius in the Arctic Ocean, *Ocean Science 10*, 967-975.

Ogilvie, A. E. J. (1984), The past climate and sea ice record from Iceland, part I: Data to A.D. 1780, *Climatic Change*, *6*, 131-152.

Olason, E., and D. Notz (2014), Drivers of variability in Arctic sea-ice drift speed, *Journal of Geophysical Research-Oceans*, *119*(9), 5755-5775.

Onstott, R. (1992), SAR and scatterometer signatures of sea ice, in *Microwave Remote Sensing of Sea Ice*, edited by F. D. Carsey, pp. 73-104, American Geophysical Union, Washington D.C., USA.

Overland, J. E., and M. Wang (2013), When will the summer Arctic be nearly sea ice free?, *Geophysical Research Letters*, *40*(10), 2097-2101.

Ozsoy-Cicek, B., S. Ackley, H. Xie, D. Yi, and J. Zwally (2013), Sea ice thickness retrieval algorithms based on in situ surface elevation and thickness values for application to altimetry, *Journal of Geophysical Research-Oceans*, *118*(8), 3807-3822.

Parkinson, C. L., and D. J. Cavalieri (1989), Arctic sea ice 1973-1987 - Seasonal, regional, and interannual variability, *Journal of Geophysical Research-Oceans*, *94*(C10), 14499-14523.

Parkinson, C. L., and D. J. Cavalieri (2012), Antarctic sea ice variability and trends, 1979-2010, *Cryosphere*, *6*(4), 871-880.

Pauling, A. G., C. M. Bitz, I. J. Smith, and P. J. Langhorne (2016), The Response of the Southern Ocean and Antarctic Sea Ice to Freshwater from Ice Shelves in an Earth System Model, *Journal of Climate*, *29*(5), 1655-1672.

Peacock, N. R., and S. W. Laxon (2004), Sea surface height determination in the Arctic Ocean from ERS altimetry, *Journal of Geophysical Research-Oceans*, *109*(C7), C07001.

Pedersen, C. A., E. Roeckner, M. Luthje, and J.-G. Winther (2009), A new sea ice albedo scheme including melt ponds for ECHAM5 general circulation model, *Journal of Geophysical Research-Atmospheres*, *114*, D08101.

Perovich, D. K., and C. M. Polashenski (2012), Albedo evolution of seasonal Arctic sea ice, *Geophysical Research Letters*, *39*, L08501.

Perovich, D. K., S. V. Nghiem, T. Markus, and A. Schweiger (2007), Seasonal evolution and interannual variability of the local solar energy absorbed by the Arctic sea ice-ocean system, *Journal of Geophysical Research-Oceans*, *112*(C3), C03005.

Petrich, C., and H. Eicken (2010), Growth, Structure and Properties of Sea Ice, in *Sea Ice, Second Edition*, edited by D. N. Thomas and G. S. Dieckmann, pp. 23-77, Wiley-Blackwell Oxford, UK.

Petty, A., D. L. Feltham, and P. R. Holland (2013), Impact of Atmospheric Forcing on Antarctic Continental Shelf Water Masses, *Journal of Physical Oceanography*, *43*(5), 920-940.

Pithan, F., and T. Mauritsen (2014), Arctic amplification dominated by temperature feedbacks in contemporary climate models, *Nature Geoscience*, *7*(3), 181-184.

Polyak, L., S. Korsun, L. A. Febo, V. Stanovoy, T. Khusid, M. Hald, B. E. Paulsen, and D. J. Lubinski (2002), Benthic foraminiferal assemblages from the southern Kara Sea, a river-influenced Arctic marine environment, *Journal of Foraminiferal Research*, *32*(3), 252-273.

Polyak, L., et al. (2010), History of sea ice in the Arctic, *Quaternary Science Reviews*, *29*(15-16), 1757-1778.

Posey, P. G., et al. (2015), Improving Arctic sea ice edge forecasts by assimilating high horizontal resolution sea ice concentration data into the US Navy's ice forecast systems, *Cryosphere*, *9*(4), 1735-1745.

Prange, M., G. Lohmann, and R. Gerdes (1997), Sensitivity of the thermohaline circulation for different climates - Investigations with a simple atmosphere-ocean model, *Paleoclimates*, *2*(1), 71-99.

Proshutinsky, A., R. Krishfield, M.-L. Timmermans, J. Toole, E. C. Carmack, F. McLaughlin, W. J. Williams, S. Zimmermann, M. Itoh, and K. Shimada (2009), Beaufort Gyre freshwater reservoir: State and variability from observations, *Journal of Geophysical Research-Oceans*, *114*.

Przybylak, R. (2016), *The Climate of the Arctic, Second Edition*, 287 pp., Springer International Publishing, Switzerland.

Purich, A., W. Cai, M. H. England, and T. Cowan (2016), Evidence for link between modelled trends in Antarctic sea ice and underestimated westerly wind changes, *Nature Communications*, *7*, 10409.

Randall, D. A., et al. (2007), Cilmate Models and Their Evaluation, in *Climate Change 2007: The Physical Science Basis. Contribution of Working Group I to the Fourth Assessment Report of the Intergovernmental Panel on Climate Change*, edited by S. Solomon, D. Qin, M. Manning, Z. Chen, M. Marquis, K. B. Averyt, M. Tignor and H. Miller, pp. 591-662, Cambridge, UK and New York, USA.

Raney, R. K. (1998), The delay/Doppler radar altimeter, *Ieee Transactions on Geoscience and Remote Sensing*, *36*(5), 1578-1588.

Raney, R. K. (1999), Radar Altimetry, in *Wiley Encyclopedia of Electrical and Electronics Engineering*, edited by J. G. Webster, pp. 547-560, John Wiley and Sons, New York, USA.

Rapley, C. G., M. A. J. Guzkowska, W. Cudlip, and I. M. Mason (1987), *An exploratory study of inland water and land altimetry using SEASAT data; ESTEC contract no. 6483/85/NL/BI*, University College London/Mullard Space Science Laboratory, Surrey, UK.

Rapley, C. G., et al. (1985), *Applications and Scientific Uses of ERS-1 Radar Altimeter Data; ESTEC contract no. 5684/83/NL/BI*, 232 pp., University College London/Mullard Space Science Laboratory, London, UK.

Rapley, C. G., et al. (1983), *A study of satellite radar atlimeter operation over ice-covered surfaces; ESA contract no. 5182/82/f/CG(SC)*, 224 pp., ESA Scientific and Techincal Publication Branch ESTEC Noordwijk, Holland.

Richter-Menge, J. A., D. K. Perovich, B. C. Elder, K. Claffey, I. Rigor, and M. Ortmeyer (2006), Ice mass-balance buoys: a tool for measuring and attributing changes in the thickness of the Arctic sea-ice cover, in *Annals of Glaciology, Vol 44, 2006*, edited by P. Langhorne and V. Squire, pp. 205-210.

Ricker, R., S. Hendricks, V. Helm, H. Skourup, and M. Davidson (2014), Sensitivity of CryoSat-2 Arctic sea-ice freeboard and thickness on radar-waveform interpretation, *The Cryosphere*, *8*(4), 1607-1622.

Ridout, A. (2012), *Sea Ice Climate Change Initiative: Phase 1 - Algorithm Theoretical Basis Document (ATBDv0), ESA document no. SICCI-ATBDv0-07-12*, 23 pp., ESRIN, ESA and Mullard Space Science Laboratory/University College London Frascati, Italy and Surrey, UK.

Ridout, A. (2014), *Tech Note - New Mean Sea Surface for the CryoSat-2 L2 SAR Chain; ESA document no. C2-TN-UCL-BC-0003 issue 1.0*, 9 pp., University College London, London, UK.

Rigor, I. G., J. M. Wallace, and R. L. Colony (2002), Response of sea ice to the Arctic oscillation, *Journal of Climate*, *15*(18), 2648-2663.

Rinne, E., and M. Similä (2016), Utilisation of CryoSat-2 SAR altimeter in operational ice charting, *The Cryosphere 10*, 121-131.

Romanov, I. P. (2004), Morphometric characteristics of ice and snow in the Arctic Basin: Aircraft landing observations from the former Soviet Union, 1928-1989 [ice freeboard, ice thickness, snow depth], edited, National Snow and Ice Data Center, Boulder, Colorado, USA.

Rothrock, D. A., J. Zhang, and Y. Yu (2003), The Arctic ice thickness anomaly of the 1990s: A consistent view from observations and models, *Journal of Geophysical Research-Oceans*, *108*(C3), 3083.

Saenko, O. A., M. Eby, and A. J. Weaver (2004), The effect of sea-ice extent in the North Atlantic on the stability of the thermohaline circulation in global warming experiments, *Climate Dynamics*, *22*(6-7), 689-699.

Sakov, P., F. Counillon, L. Bertino, K. A. Lisaeter, P. R. Oke, and A. Korablev (2012), TOPAZ4: an ocean-sea ice data assimilation system for the North Atlantic and Arctic, *Ocean Science*, *8*(4), 633-656.

Sanderson, R. M. (1975), Changes in area of Arctic sea ice 1966 to 1974, *Meteorological Magazine*, *104*(1240), 313-323.

Sato, K. (2014), Anthropogenic climate change in an integrated Energy Balance Model of global and urban warming, *Journal of Economic Structures*, *3*(9), 1-21.

Savelle, J. M., A. S. Dyke, and A. P. McCartney (2000), Holocene bowhead whale (Balaena mysticetus) mortality patterns in the Canadian Arctic Archipelago, *Arctic*, *53*(4), 414-421.

Schroeder, D., D. L. Feltham, D. Flocco, and M. Tsamados (2014), September Arctic sea-ice minimum predicted by spring melt-pond fraction, *Nature Climate Change*, *4*(5), 353-357.

Schweiger, A., R. W. Lindsay, S. Vavrus, and J. A. Francis (2008), Relationships between Arctic sea ice and clouds during autumn, *Journal of Climate*, *21*(18), 4799-4810.

Schweiger, A., R. Lindsay, J. L. Zhang, M. Steele, H. Stern, and R. Kwok (2011), Uncertainty in modeled Arctic sea ice volume, *Journal of Geophysical Research-Oceans*, *116*(C8), C00D06.

Screen, J. A., and I. Simmonds (2010a), The central role of diminishing sea ice in recent Arctic temperature amplification, *Nature*, *464*(7293), 1334-1337.

Screen, J. A., and I. Simmonds (2010b), Increasing fall-winter energy loss from the Arctic Ocean and its role in Arctic temperature amplification, *Geophysical Research Letters*, *37*, L16707.

Sellers, W. D. (1969), A Global Climatic Model Based on the Energy Balance of the Earth-Atmosphere System, *Journal of Applied Meteorology*, *8*, 392-400.

Serreze, M. C., and R. G. Barry (2005), *The Arctic Climate System*, 385 pp., Cambridge University Press, Cambridge, UK.

Serreze, M. C., and J. A. Francis (2006), The Arctic amplification debate, *Climatic Change*, *76*(3-4), 241-264.

Serreze, M. C., and R. G. Barry (2011), Processes and impacts of Arctic amplification: A research synthesis, *Global and Planetary Change*, *77*(1-2), 85-96.

Serreze, M. C., J. E. Box, R. G. Barry, and J. E. Walsh (1993), Characteristics of Arctic synoptic activity, 1952-1989, *Meteorology and Atmospheric Physics*, *51*(3-4), 147-164.

Sewall, J. O., and L. C. Sloan (2004), Disappearing Arctic sea ice reduces available water in the American west, *Geophysical Research Letters*, *31*(6), L06209.

Shepherd, A., et al. (2012), A Reconciled Estimate of Ice-Sheet Mass Balance, *Science*, *338*(6111), 1183-1189.

Sigmond, M., J. C. Fyfe, G. M. Flato, V. V. Kharin, and W. J. Merryfield (2013), Seasonal forecast skill of Arctic sea ice area in a dynamical forecast system, *Geophysical Research Letters*, *40*(3), 529-534.

Singarayer, J. S., J. L. Bamber, and P. J. Valdes (2006), Twenty-first-century climate impacts from a declining Arctic sea ice cover, *Journal of Climate*, *19*(7), 1109-1125.

Smedsrud, L. H., A. Sirevaag, K. Kloster, A. Sorteberg, and S. Sandven (2011), Recent wind driven high sea ice area export in the Fram Strait contributes to Arctic sea ice decline, *Cryosphere*, *5*(4), 821-829.

Smith, D. M. (1998), Recent increase in the length of the melt season of perennial Arctic sea ice, *Geophysical Research Letters*, *25*(5), 655-658.

Smithson, P., K. Addison, and K. Atkinson (2008), *Fundamentals of the Physical Environment: Fourth Edition*, 792 pp., Routledge, Abingdon, UK.

Stewart, E. J., S. E. L. Howell, D. Draper, J. Yackel, and A. Tivy (2007), Sea ice in Canada's Arctic: Implications for cruise tourism, *Arctic*, *60*(4), 370-380.

Stroeve, J. C., M. M. Holland, W. Meier, T. Scambos, and M. C. Serreze (2007), Arctic sea ice decline: Faster than forecast, *Geophysical Research Letters*, *34*(9), L09501.

Stroeve, J. C., T. Markus, L. Boisvert, J. Miller, and A. Barrett (2014), Changes in Arctic melt season and implications for sea ice loss, *Geophysical Research Letters*, *41*(4), 1216-1225.

Stroeve, J. C., M. C. Serreze, M. M. Holland, J. E. Kay, J. Malanik, and A. P. Barrett (2012a), The Arctic's rapidly shrinking sea ice cover: A research synthesis, *Climatic Change*, *110*(3-4), 1005-1027.

Stroeve, J. C., M. C. Serreze, F. Fetterer, T. Arbetter, W. Meier, J. Maslanik, and K. Knowles (2005), Tracking the Arctic's shrinking ice cover: Another extreme September minimum in 2004, *Geophysical Research Letters*, *32*(4), L04501.

Stroeve, J. C., V. Kattsov, A. Barrett, M. Serreze, T. Pavlova, M. Holland, and W. N. Meier (2012b), Trends in Arctic sea ice extent from CMIP5, CMIP3 and observations, *Geophysical Research Letters*, *39*, L16502.

Svendsen, E., K. Kloster, B. Farrelly, O. M. Johannessen, J. A. Johannessen, W. J. Campbell, P. Gloersen, D. Cavalieri, and C. Matzler (1983), Norwegian remote-sensing experiment - Evaluation of the Nimbus-7 scanning multichannel microwave radiometer for sea ice research, *Journal of Geophysical Research-Oceans and Atmospheres*, *88*(NC5), 2781-2791.

Swift, C. T., and D. J. Cavalieri (1985), Passive microwave remote sensing for sea ice research, *Eos Transactions of the American Geophysical Union*, *66*(49), 1210-1212.

Swim, J., S. Clayton, T. Doherty, R. Gifford, G. Howard, J. Reser, P. Stern, and E. Weber (2010), *Psychology and global climate change: addressing a multifaceted phenomenon and set of challenges. A report of the American Psychological Association task force on the interface between psychology and global climate change 2010*, 108 pp., available at http://www.apa.org/science/about/publications/climate-change.aspx.

Tao, X., J. E. Walsh, and W. L. Chapman (1996), An assessment of global climate model simulations of arctic air temperatures, *Journal of Climate*, *9*(5), 1060-1076.

Taylor, K. E., R. J. Stouffer, and G. A. Meehl (2012), An overview of CMIP5 and the experiment design, *Bulletin of the American Meteorological Society*, 485-498.

Taylor, P. C., M. Cai, A. Hu, G. A. Meehl, W. Washington, and G. J. Zhang (2013), A decomposition of feedback contributions to polar warming amplification (vol 26, pg 7023, 2013), *Journal of Climate*, *26*(21), 8706-8706.

Thorndike, A. S., and R. Colony (1982), Sea ice motion in response to geostrophic winds, *Journal of Geophysical Research-Oceans and Atmospheres*, *87*(NC8), 5845-5852.

Tilling, R. L., A. Ridout, and A. Shepherd (2016), Near Real Time Arctic sea ice thickness and volume from CryoSat-2, *The Cryosphere*, *10*, 2003-2016.

Tilling, R. L., A. Ridout, A. Shepherd, and D. J. Wingham (2015), Increased Arctic sea ice volume after anomalously low melting in 2013, *Nature Geoscience*, *8*, 643-646.

Tsamados, M., D. L. Feltham, and A. V. Wilchinsky (2013), Impact of a new anisotropic rheology on simulations of Arctic sea ice, *Journal of Geophysical Research-Oceans*, *118*(1), 91-107.

Tsamados, M., D. L. Feltham, A. Petty, D. Schroeder, and D. Flocco (2015), Processes controlling surface, bottom and lateral melt of Arctic sea ice in a state of the art sea ice model, *Philosophical Transactions of the Royal Society A-Mathematical Physical and Engineering Sciences*, *373*(2052), 1-30.

Tsamados, M., D. L. Feltham, D. Schroeder, D. Flocco, S. L. Farrell, N. Kurtz, S. W. Laxon, and S. Bacon (2014), Impact of Variable Atmospheric and Oceanic Form Drag on Simulations of Arctic Sea Ice*, *Journal of Physical Oceanography*, *44*(5), 1329-1353.

Tschudi, M., C. Fowler, J. Maslanik, J. S. Stewart, and W. Meier (2016), Polar Pathfinder Daily 25 km EASE-Grid Sea Ice Motion Vectors, Version 3, edited, NASA DAAC at the National Snow and Ice Data Center - Digital Media, Boulder, Colorado, USA.

Ulaby, F. T., R. K. Moore, and A. K. Fung (1986), *Microwave Remote Sensing: Active and Passive, Volume II: Radar Remote Sensing and Surface Scattering and Emission Theory* 608 pp., Norwood, MA, USA.

Vancoppenolle, M., T. Fichefet, H. Goosse, S. Bouillon, G. Madec, and M. A. Morales Maqueda (2009), Simulating the mass balance and salinity of Arctic and Antarctic sea ice. 1. Model description and validation, *Ocean Modelling*, *27*, 33-53.

Vellinga, M., and R. A. Wood (2002), Global climatic impacts of a collapse of the Atlantic thermohaline circulation, *Climatic Change*, *54*(3), 251-267.

Vose, R. S., et al. (2012), NOAA's merged land-ocean surface temperature analysis, *Bulletin of the American Meteorological Society*, *93*(11), 1677-1685.

Wadhams, P. (1990), Evidence for thinning of the Arctic ice cover north of Greenland, *Nature*, *345*(6278), 795-797.

Wadhams, P. (2000), *Ice In The Ocean*, 364 pp., Gordon and Breach Science Publishers, Amsteldijk, The Netherlands.

Wadhams, P., W. B. I. Tucker, W. B. Krabill, J. C. Swift, J. C. Comiso, and N. R. Davis (1992), Relationship between sea ice freeboard and draft in the Arctic Basin, and implications for ice thickness monitoring, *Journal of Geophysical Research-Oceans*, *97*(C12), 20325–20334.

Wadhams, P., N. R. Davis, J. C. Comiso, R. Kutz, J. Crawford, G. Jackson, W. Krabill, C. B. Sear, R. Swift, and W. B. Tucker (1991), Concurrent remote-sensing of Arctic sea ice from submarine and aircraft, *International Journal of Remote Sensing*, *12*(9), 1829-1840.

Walsh, J. E., and W. L. Chapman (2001), 20th-century sea-ice variations from observational data, in *Annals of Glaciology, Vol 33*, edited by M. O. Jeffries and H. Eicken, pp. 444-448.

Wang, M., J. E. Overland, V. Kattsov, J. E. Walsh, X. Zhang, and T. Pavlova (2007), Intrinsic versus forced variation in coupled climate model simulations over the Arctic during the twentieth century, *Journal of Climate*, *20*(6), 1093-1107.

Warren, S. G., I. G. Rigor, N. Untersteiner, V. F. Radionov, N. N. Bryazgin, Y. I. Aleksandrov, and R. Colony (1999), Snow depth on Arctic sea ice, *Journal of Climate*, *12*(6), 1814-1829.

Webster, M. A., I. G. Rigor, S. V. Nghiem, N. T. Kurtz, S. L. Farrell, D. K. Perovich, and M. Sturm (2014), Interdecadal changes in snow depth on Arctic sea ice, *Journal of Geophysical Research-Oceans*, *119*(8), 5395-5406.

Wessel, P., and W. H. F. Smith (1991), Free software helps map and display data, *Eos Transactions of the American Geophysical Union*, *72*(41), 445-446.

Wessel, P., W. H. F. Smith, R. Scharroo, J. Luis, and F. Wobbe (2013), Generic mapping tools: Improved version released, *Eos Transactions of the American Geophysical Union*, *94*(45), 409-410.

White, D. M., S. C. Gerlach, P. Loring, A. C. Tidwell, and M. C. Chambers (2007), Food and water security in a changing arctic climate, *Environmental Research Letters*, *2*(4), 045018.

Willatt, R. C., K. A. Giles, S. W. Laxon, L. Stone-Drake, and A. P. Worby (2010), Field investigations of Ku-band radar penetration into snow cover on Antarctic sea ice, *IEEE Transactions on Geoscience and Remote Sensing*, *48*(1), 365-372.

Willox, A. C., et al. (2015), Examining relationships between climate change and mental health in the Circumpolar North, *Regional Environmental Change*, *15*(1), 169-182.

Wingham, D. J., et al. (2006), CryoSat: A mission to determine the fluctuations in Earth's land and marine ice fields, in *Natural Hazards and Oceanographic Processes from Satellite Data*, edited by R. P. Singh and M. A. Shea, pp. 841-871.

Winton, M. (1997), The effect of cold climate upon North Atlantic Deep Water formation in a simple ocean-atmosphere model, *Journal of Climate*, *10*(1), 37-51.

Winton, M. (2006), Amplified Arctic climate change: What does surface albedo feedback have to do with it?, *Geophysical Research Letters*, *33*(3), L03701.

Worby, A. P., C. A. Geiger, M. J. Paget, M. L. Van Woert, S. F. Ackley, and T. L. DeLiberty (2008), Thickness distribution of Antarctic sea ice, *Journal of Geophysical Research-Oceans*, *113*(C5), article C05s92.

Worster, M. G., and D. W. R. Jones (2015), Sea-ice thermodynamics and brine drainage, *Philosophical Transactions of the Royal Society A-Mathematical Physical and Engineering Sciences*, *373*, 20140166.

Wunsch, C., and D. Stammer (1998), Satellite altimetry, the marine geoid, and the oceanic general circulation, *Annual Review of Earth and Planetary Sciences*, *26*, 219-253.

Yan, H., et al. (2012), Global estimation of evapotranspiration using a leaf area index-based surface energy and water balance model, *Remote Sensing of Environment*, *124*, 581-595.

Ye, Y. F., M. Shokr, G. Heygster, and G. Spreen (2016), Improving Multiyear Sea Ice Concentration Estimates with Sea Ice Drift, *Remote Sensing*, *8*(5), 397.

Zhang, J. L. (2007), Increasing Antarctic sea ice under warming atmospheric and oceanic conditions, *Journal of Climate*, *20*(11), 2515-2529.

Zhang, J. L., and D. A. Rothrock (2003), Modeling global sea ice with a thickness and enthalpy distribution model in generalized curvilinear coordinates, *Monthly Weather Review*, *131*(5), 845-861.